Université du Québec
à Rimouski

Influence des conditions météorologiques et des changements climatiques sur le développement des instabilités rocheuses des parois de flysch de la Haute-Gaspésie (Qc, Canada)

Thèse présentée

dans le cadre du programme de doctorat en sciences de l'environnement

en vue de l'obtention du grade de Philosophiæ doctor (Ph.D.)

PAR

© TOM BIRIEN

Janvier 2023

Composition du jury :

Pascal Bernatchez, président du jury, Université du Québec à Rimouski

Francis Gauthier, directeur de recherche, Université du Québec à Rimouski

Daniel Fortier, codirecteur de recherche, Université de Montréal

Michael Krautblatter, examinateur externe, Université technique de Munich

Dépôt initial le 02-09-2022 Dépôt final le 09-01-2023

DÉDICACE

À Frédérique Dumont,

Pour ton appui indéfectible dans toutes les sphères de ma vie. Ma gratitude est immense.

REMERCIEMENTS

Je débute logiquement cette section en remerciant l'initiateur de ce projet, Francis Gauthier. J'ai immigré au Québec en 2017 pour travailler deux ans dans ton laboratoire. Force est de constater que je m'y suis bien plu puisqu'après y avoir finalement fait un doctorat, c'est encore ici que je veux continuer à me creuser les méninges ! Au-delà de ta casquette de directeur, je voulais surtout te remercier pour ton écoute, ta patience, ta générosité et ta bienveillance. Je suis fier d'avoir vécu cette aventure avec toi.

Je tiens à remercier Daniel Fortier, Catherine Cloutier et Guillaume Marie de m'avoir aiguillé dès le début du projet. Vos commentaires m'ont permis de cibler des objectifs plus ambitieux et de ce fait, d'améliorer substantiellement la qualité de ma thèse de doctorat.

Je remercie également le ministère des Transports du Québec (MTQ) d'avoir mis les moyens financiers nécessaires à la réalisation de ce projet de grande ampleur. Les résultats obtenus découlent directement de l'instrumentation conséquente que vous nous avez permis de déployer dans le nord de la Gaspésie. Dans ce contexte, je tiens à souligner la confiance des membres du comité de suivi du service de la géotechnique et de la géologie du MTQ. L'autonomie que vous m'avez accordée tout au long de ce projet m'a permis d'exploiter pleinement ma créativité et de décupler le plaisir pris à mener mes recherches. Je remercie également le Conseil de recherches en sciences naturelles et en génie (CRSNG) du Canada d'avoir contribué financièrement à ce projet.

D'autres structures ont joué un rôle essentiel dans le bon déroulement de mon projet. Je remercie le laboratoire ouvert de géothermie (LOG) de l'Institut national de la recherche scientifique (INRS) pour leur accueil et pour leur accompagnement. Je remercie le Laboratoire de dynamique et de gestion intégrée des zones côtières (LDGIZC) pour le prêt d'équipements. À force de mener des terrains en solitaire, j'ai fini par me lier d'amitié pour

votre LiDAR. Nous avons le point commun de connaître chaque roche du nord de la Gaspésie. Je remercie également le centre pour l'étude et la simulation du climat à l'échelle régionale (ESCER) de l'Université du Québec à Montréal (UQAM) pour les précieuses données que vous m'avez fournies.

Le doctorat a beau être une aventure particulièrement solitaire, il y a certaines marches que je n'aurais pas pu gravir en solitaire. Malgré le poids de ma nonchalance très peu dissimulée, c'est avec une aisance déconcertante, et un système de poulies dont lui seul a le secret, que François Truchon m'a directement téléporté quelques marches plus haut. J'ai ainsi pu, la même année, réaliser un forage horizontal de deux pouces de diamètre et de plus de 550 centimètres de profondeur avec 100 mètres de vide sous les pieds sur une paroi rocheuse, avant d'échouer à installer des tablettes dans du gyproc. Cela dit, il en fallait plus pour me perturber. À la suite de ton départ, j'ai rapidement constaté qu'il ne me suffisait plus de tourner la tête quand j'avais un problème pour en trouver la solution. J'avais beau regarder dans toutes les directions, et il y en a beaucoup sur une paroi rocheuse, j'étais maintenant la personne la plus qualifiée. Cette fois, j'étais perturbé. Ça m'a d'abord déplu, me sortant de ma zone de confort, mais rapidement, comme toi, je suis devenu méthodique, exigeant et nécessairement un peu chiant. Pour gravir les échelons du doctorat, j'ai aussi pu compter sur des bons coups de main de la part de Francis Meloche. Plus que des coups de main, je dirais que tu m'as pris par la main pendant ma première année à Rimouski. Tu m'as accueilli chaleureusement, tu m'as bien souvent prêté ton sofa et c'est aussi avec toi que j'ai acheté mon premier bâton de hockey ou que j'ai découpé mes premières peaux de phoques. On a également partagé suffisamment de terrains pour monter de solides statistiques (toi dans R, moi dans Excel) sur le nombre de degrés-jours de dégel nécessaire à l'inondation du sous-sol de la maison du fond du rang de Rivière-à-Claude. Je me souviens aussi de ce jour de Noël, froid et venteux, passé tous les deux sur les parois rocheuses. Les terrains hivernaux exigeants, il y en a eu beaucoup et Nathalie Thériault a aussi pu y goûter. Au-delà de ton immense bienveillance que je souhaitais souligner, je voulais aussi te remercier pour tous les petits coups de pouce que tu as pu me donner. Mis bout à bout, ce sont encore quelques marches supplémentaires de gravies. Au LGGRM, je tenais également à remercier Julie

Major, Chloé Chouinard et Matteo Arnaldi pour votre aide sur le terrain mais surtout pour les beaux moments de vie que nous avons pu partager dans les dernières années.

Malgré une santé mentale parfois mise à rude épreuve, la présence au quotidien d'un formidable entourage m'a permis de garder la tête hors de l'eau et de globalement vivre de belles années. Stéphanie Arnold, pour toutes tes initiatives et pour m'avoir offert mes plus grands moments d'évasion. Éric Fjord Bouillé, pour les riches émotions que nous avons pu vivre ensemble. Emmanuelle Doran, pour la grandeur de notre amitié. Loïc Théberge Dallaire, pour ta présence. Caroline Charpentier, pour ta bienveillance. Sans oublier Flavie Demers, Leïla Bennour, Gauthier Cervello, Nolwenn Dubois, François Dallaire, Charles Béland, Audrey Pilon, Maëva Dolle, Maurisseau Michelet, Mackendy Nazaire, Delphine Cottier, Clara Boily, Lancelot Massé, Naomy Bédard, Martin Laroche, Étienne Quillet, Annie-France Richard, Benjamin Saint-Onge, Jean-Philippe Angers et bien d'autres.

De l'autre côté de l'Atlantique, je tenais à remercier Simon Oliviero et Antoine Carrouée, mes deux acolytes de toujours, Coralie Chaban pour tous ces moments de qualité mais aussi Léa Costales, Émilie Hogrefe-Bataillon, Bleuenn Bodin, Mickael Abraham, Lara Deguise, Aurélie Nicolas, Fabien Bertho, Guillaume Coiffard et bien d'autres. À la blague mais quand même sérieusement, je remercie Roger Federer, Thibaut Pinot, Julian Alaphilippe, Romain Bardet et l'Équipe de France de football pour les émotions vécues par procuration.

Pendant la majeure partie de mon enfance, l'école représentait surtout une source d'anxiété pour moi. Je remercie mes coachs, Loïc Rapinel et Gaëlle Houitte, d'avoir, dès mon adolescence, inscrit la volonté et la persévérance à mon ADN. *Là où il y a une volonté, il y a un chemin* (William Hazlitt). L'ajout de ces quelques cordes supplémentaires à mon arc m'aura porté bien au-delà de ce que je n'aurais jamais pu imaginer.

Dans la dernière année, d'autres défis majeurs sont venus s'ajouter à celui qui constituait à achever ce doctorat. Malgré tout, avec un peu de recul, c'est de ton sourire dont je me souviendrai Sandrine. Merci à toi d'avoir rendu cette année surmontable.

Je termine cette section en remerciant ma famille (Paulette, René, Rosa : j'ai finalement terminé l'école !) et tout particulièrement mes parents. Dans le cadre de mes remerciements de thèse, je dois me contenter de vous remercier pour votre soutien pendant la durée de cette épreuve, même si ce soutien me donne de la force depuis toujours et je ne crois pas avoir besoin de lire l'avenir pour être capable d'anticiper qu'il me transportera encore dans le futur. Cette relation est intemporelle et ça tombe bien car comme le chante si bien Orelsan :

« Maman est là, mon père est fier
Et l'Univers n'est pas si mal ».

AVANT-PROPOS

L'épisode caniculaire qui a touché l'Europe au mois d'août 2003 a marqué les esprits. Mon esprit d'enfant peut-être encore davantage. C'est avec une grande assiduité que j'ai commencé à prendre des relevés de température de l'air et de pluviométrie quotidiennement ainsi qu'à parcourir le monde virtuellement pour en apprendre plus sur ses climats. Je ne connaissais à peu près rien de la diversité des paysages et de la richesse culturelle des endroits que je sillonnais mais le régime de température de la Sibérie et la pluviométrie de l'Amazonie m'étaient bien familiers. En grandissant, j'ai graduellement compris le rôle primordial de la climatologie et de la météorologie dans le façonnement de l'ensemble des paysages terrestres et dans la répartition de la faune et de la flore qui y résident. La Lune a de quoi être jalouse de notre atmosphère et de ses nuages ! Les rencontres que j'ai pu faire dans les premières années de mon cursus universitaire ont fait en sorte que je me suis tourné vers la géographie plutôt que vers la biologie. Je me suis d'abord intéressé à l'estran, au déplacement des blocs glaciels pendant mon baccalauréat et à la dynamique des plages de sable pendant ma maîtrise. J'ai ensuite pris un peu de hauteur en étudiant dans le cadre de ce doctorat, l'influence des conditions météorologiques sur l'érosion des parois rocheuses. En prenant un peu de recul sur ces différents projets, je dirai que je n'ai pas de favorite parmi les disciplines de la géomorphologie mais que mon intérêt se porte bel et bien sur l'interaction entre la météorologie et la géomorphologie.

Ce doctorat s'inscrit dans un projet plus large, à destination du Ministère des Transports du Québec (MTQ) et qui s'intitule « Influence des variables météorologiques et des changements climatiques sur l'occurrence, la fréquence et la magnitude des mouvements de versant (avalanche de neige, chute de blocs de glace et chute de pierre) affectant certains tronçons des routes 132 et 198 dans le nord de la Gaspésie ». Malgré le fait que je ne sois pas l'initiateur de ce projet qui avait préalablement été mûrement réfléchi par Francis Gauthier,

j’ai pu progressivement me l’approprier. La grande liberté qu’a été la mienne pendant ces cinq années m’a permis de définir mes objectifs et d’exprimer ma créativité. En plus de contribuer à l’avancée des connaissances scientifiques, les résultats de mes travaux pourront servir au MTQ ou à d’autres organismes afin d’améliorer la gestion du risque naturel que peut constituer les chutes de pierres.

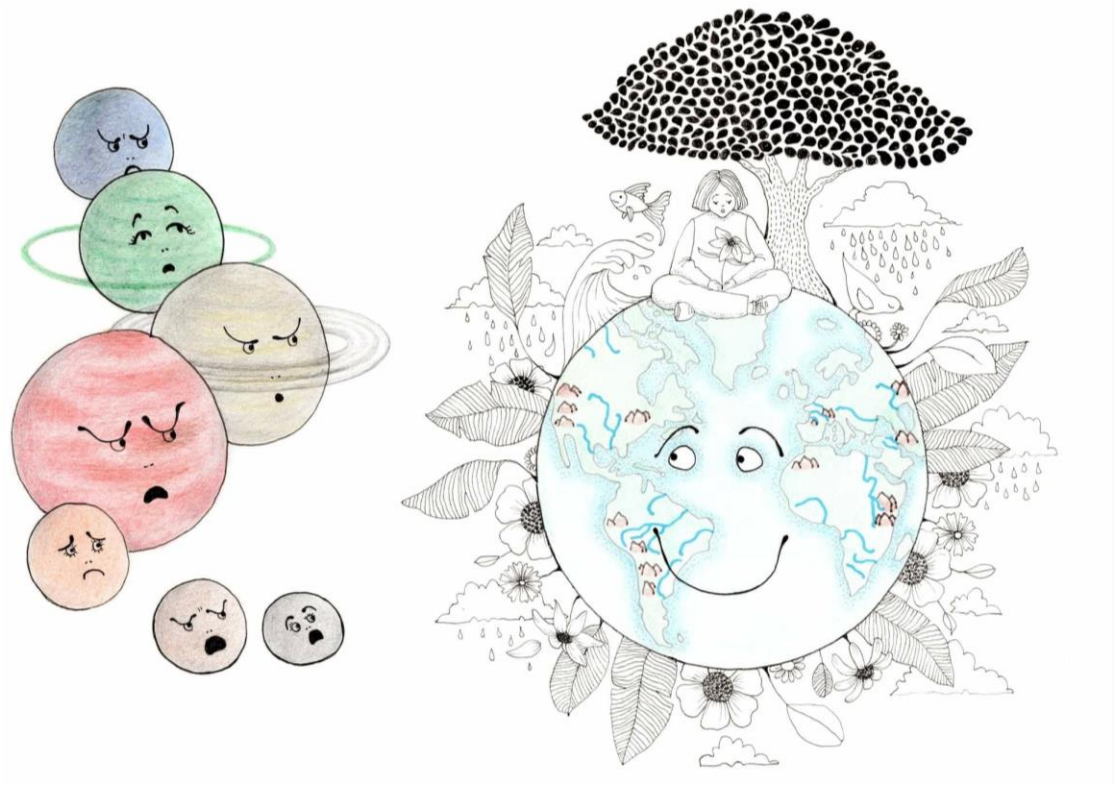

Ma vision d’enfance de la Terre, de son climat et des paysages qui en résultent.
Illustration de Camille Birien.

RÉSUMÉ

Depuis 1987, plus de 17 500 chutes de pierres atteignant les routes de la Haute-Gaspésie ont été répertoriées par le ministère des Transports du Québec (MTQ). Cet aléa naturel représente un danger quasi permanent pour les usagers. Les mesures d'atténuation traditionnelles peuvent s'avérer inefficaces sur des parois rocheuses hautement fracturées comme celles de la Gaspésie. La mise en place d'une gestion préventive du risque, basée sur les facteurs déclenchant les instabilités rocheuses, pourrait être la méthode la plus efficace pour réduire la vulnérabilité des usagers. Des études préliminaires ont montré que ces instabilités sont majoritairement déclenchées par des facteurs externes étroitement liés aux conditions météorologiques. Cette thèse vise 1) à mieux comprendre les processus pré-rupture qui contribuent au développement des instabilités rocheuses, 2) à améliorer notre capacité à prédire les chutes de pierres et 3) à anticiper l'influence du réchauffement climatique contemporain sur la météorisation et l'érosion des parois rocheuses. Un réseau de capteurs hydrométéorologiques a été déployé à la surface de cinq parois rocheuses d'orientations nord et sud et de structures géologiques variées allant du conglomérat massif aux parois sédimentaires stratifiées et hautement fracturées. Des thermistances introduites dans des forages horizontaux de 3 à 5,5 mètres de profondeur ont permis de mesurer le régime thermique de ces parois. Les déformations mécaniques affectant une séquence de flysch ont été enregistrées par des extensomètres pendant une période de 28 mois. La fréquence et la magnitude des chutes de pierres ont été quantifiées sur trois sites à l'aide d'un scanner laser terrestre (TLS) pendant 17 périodes météorologiques ciblées au préalable. Finalement, le régime thermique et le taux de météorisation par le gel d'une des parois rocheuses instrumentée a été modélisé entre 1950 et 2100. Les déformations irréversibles enregistrées en surface par les extensomètres sont principalement induites par les variations brèves et soutenues de la teneur en eau (pluies et fonte des neiges), par les fluctuations de température autour du point de congélation (cycles gel-dégel) et dans une moindre mesure, par les fortes amplitudes thermiques. Les tendances à long terme mettent en évidence les mécanismes qui conduisent à l'érosion différentielle des séquences de flysch. Le recul et le tassement progressifs des strates de siltstone provoquent la déstabilisation par glissement ou basculement de blocs des strates de grès sus-jacentes. Les relevés au TLS ont permis d'identifier 1287 chutes de pierres d'une magnitude supérieure à 0,005 m^3 sur une surface scannée de 12 056 m^2 pendant une période de 18 mois. En été, la fréquence des chutes de pierres est 22 fois plus élevée lors d'une pluie de forte intensité que pendant une période sèche. En hiver, la fréquence des chutes de pierres est 12 fois plus élevée lors d'un dégel superficiel (< 30 cm) que lors d'une période froide où la température reste inférieure à 0°C. Ces redoux hivernaux se traduisent par le développement d'instabilités rocheuses de faible magnitude alors que le dégel printanier en profondeur entraîne une fréquence élevée

d'événements de grande magnitude. Selon les scénarios RCP4.5 et RCP8.5, un réchauffement de 3,3°C à 6,2°C a été modélisé en Haute-Gaspésie au cours du 21ème siècle. Ce réchauffement rapide devrait se répercuter par une diminution d'un à deux mètres de la profondeur maximale atteinte par le front de gel saisonnier et par un raccourcissement de sa durée d'un à trois mois. La fréquence des redoux hivernaux pourrait être multipliée par 12 en janvier. L'efficacité de la fracturation par le gel devrait rester importante en surface, s'intensifier autour de 70 cm de profondeur et s'estomper au-delà (RCP4.5), ou bien diminuer dès 10 cm de profondeur (RCP8.5). Dans cette région soumise à des cycles gel-dégel saisonniers, la fréquence des chutes de pierres de faible magnitude pourrait considérablement augmenter en hiver mais être largement réduite à l'automne et au printemps. Les processus associés au gel-dégel ne contribueront plus au développement d'instabilités de plus grande ampleur. Cette étude propose une classification des conditions météorologiques en fonction de leur capacité à déclencher des instabilités rocheuses de différentes magnitudes. Elle apporte également, dans le contexte du réchauffement climatique, une meilleure connaissance de l'évolution des périodes propices aux chutes de pierres d'ici la fin du 21ème siècle. Ces connaissances pourront être utilisées afin de mettre en place une gestion préventive du risque naturel qui permettrait de diminuer la vulnérabilité des usagers des routes de la Haute-Gaspésie.

Mots-clés : déformation mécanique, chutes de pierres, paroi rocheuse, flysch, régime thermique, conditions météorologiques, réchauffement climatique, extensomètre, TLS, LiDAR.

ABSTRACT

Since 1987, more than 17 500 rockfalls hitting the roads have been inventoried by the Ministère des Transports du Québec (MTQ) in northern Gaspésie. This natural hazard represents a nearly permanent danger for users. Traditional mitigation measures can be ineffective on poorly consolidated, deformed and highly fractured rockwalls such as those found in the area. Implement a preventive risk management based on the factors that trigger rock instabilities could be the most effective method to limit the vulnerability of road users. Preliminary studies have shown that these instabilities are often triggered by external factors that are closely related to meteorological conditions. This thesis aims 1) to better understand the pre-failure processes that contribute to rockfall development, 2) to improve our ability to predict and anticipate rockfalls and 3) to explore the influence of climate warming on rockwall erosion. A network of hydrometeorological sensors has been deployed at the surface of five north and south facing rockwalls with changing structural geology from massive conglomerate to highly stratified sedimentary rocks. Their thermal regimes have also been measured using thermistor sensors inserted in horizontal boreholes 3 to 5.5 meters deep. Mechanical deformations of a flysch sequence composed of sandstone and siltstone have been recorded by crack-meters during a 28-month period. Rockfall frequency and magnitude have been quantified on three sites using a terrestrial laser scanner (TLS) during specific pre-targeted meteorological conditions. Finally, the thermal regime and the rate of frost damage of one of the studies rockwall has been modeled between 1950 and 2100. Irreversible deformations recorded at the rock surface by crack meter are mostly induced by large and sustained changes of water content (rainfall and snowmelt), by temperature fluctuations around the freezing point (freeze-thaw cycles) and to a lesser extent, by large thermal variations. The long-term trends recorded in the sandstone and siltstone strata highlight mechanisms that lead to differential erosion of flysch sequences. Gradual retreating and settling of the weak rock strata (clayey siltstone) cause destabilization of the resistant rock strata (sandstone) above and the eventual slide or topple of sandstone blocks. Over a period of 18 months, 17 surveys using TLS have allowed to identify 1287 rockfalls with a magnitude above 0.005 m^3 on a scanned surface of 12 056 m^2. In summer, rockfall frequency was 22 times higher during a heavy rainfall event than during a period mainly dry. In winter, rockfall frequency was 12 times higher during a superficial thaw (< 30 cm) than during a cold period in which temperature remained below 0°C. These winter thaws result in the development of small magnitude rock instabilities while deep spring thaw result in a high frequency of large magnitude events. According to the RCP4.5 and RCP8.5 scenarios, a warming of 3.3°C to 6.2°C is respectively expected in northern Gaspésie during the 21st century. This rapid warming should result in a reduction of one to two meters in the maximum depth reached by the seasonal frost front and a shortening of its duration by one to three months. The frequency

of sporadic freeze-thaw cycles could be multiplied by 12 in January. The effectiveness of frost weathering should intensify around 70 cm depth and fade beyond (RCP4.5) or decrease from 10 cm depth (RCP8.5). In this region subject to seasonal freeze-thaw cycles, the frequency of small magnitude rockfalls could increase considerably in winter but be greatly reduced in autumn and spring. Freeze-thaw associated processes will no longer contribute to the development of larger magnitude instabilities. This study provides a classification of meteorological conditions based on their ability to trigger rockfalls of different magnitudes. It also allows, in the global warming context, to anticipate the evolution of the favorable periods of rockfall by the end of the 21st century. This knowledge could be used to implement an adequate preventive risk management strategy and thus reduce the vulnerability of road users in Haute-Gaspésie.

Keywords: rock deformation, rockfall, rockwall, flysch, thermal regime, weather conditions, climate warming, crack meter, TLS, LiDAR.

TABLE DES MATIÈRES

LISTE DES TABLEAUX

LISTE DES FIGURES

LISTE DES ABRÉVIATIONS, DES SIGLES ET DES ACRONYMES

ANP	Anse-Pleureuse (lieu)
CAM	Cap-Madeleine (lieu)
CAR	Cap-au-Renard (lieu)
CCCma	Canadian Centre for Climate Modelling and Analysis
CEN	Centre d'Étude Nordique
CORDEX	Coordinated Regional Climate Downscaling Experiment
CRCM5	fifth-generation Canadian Regional Climate Model
ESCER	Étude et la Simulation du Climat à l'Échelle Régionale (centre de recherche)
ETE	Eau Terre Environnement (centre de recherche)
FT	Freeze-Thaw
GCM	Global Climate Model
GIEC	Groupe d'experts Intergouvernemental sur l'Évolution du Climat
GMO	Gros-Morne Ouest (lieu)
HDS	High Definition Surveying
HIRHAM	This acronym comes from the combination of HIRLAM (High Resolution Limited Area Model) and ECHAM (European Centre in HAMbourg)
ICHEC	Irish Centre for High-End and Computing

INRS	Institut National de la Recherche Scientifique
IPCC	Intergovernmental Panel on Climate Change
LGGRM	Laboratoire de Géomorphologie et de Gestion des Risques en Montagne
LiDAR	Light Detection And Ranging
LOG	Laboratoire Ouvert de Géothermie
M3C2	Multiscale Model to Model Cloud Comparison
MAE	Manche d'Épée (lieu)
MAR	Marsoui (lieu)
MPI	Max Planck Institut
MSP	Mont-Saint-Pierre (lieu)
MTQ	Ministère des Transports du Québec
NSERC	Natural Sciences and Engineering Research Council
PCA	Principal Component Analysis
RCA4	fourth Rossby Centre regional Atmospheric model
RCM	Regional Climate Model
RCP	Representative Concentration Pathways
RF	Rainfall
RST	Rock Surface Temperature
SR	Solar Radiation
TLS	Terrestrial Laser Scanning

UDEM Université de Montréal

UNDRR United Nations Office for Disaster Risk Reduction

UQAM Université du Québec à Montréal

UQAR Université du Québec à Rimouski

WC Water content

LISTE DES SYMBOLES

%	Pourcentage
Δ	Différence
Ø	Sans unité
±	Plus ou moins
≥	Supérieur ou égal
>	Supérieur
<	Inférieur
=	Égal
≈	Environ égal
mm	Millimètre
cm	Centimètre
dm	Décimètre
m	Mètre
km	Kilomètre
m^2	Mètre carré
m^3	Mètre cube
in	Inches

s	Seconde
min	Minute
d	Day (jour)
y	Year (année)
kg	Kilogramme
°	Degré
W	Watt
MHz	Mégahertz
J	Joule
K	Kelvin
MPa	Mégapascal
mbar	Millibar
R^2	Coefficient de détermination linéaire de Pearson
f(x)	Fonction

INTRODUCTION GÉNÉRALE

1. LA PROBLÉMATIQUE DES CHUTES DE PIERRES EN HAUTE-GASPESIE

Dans le nord de la Gaspésie, deux axes routiers sont particulièrement exposés aux chutes de pierres. Il s'agit de la portion de la route nationale 132 qui relie le village de Cap-au-Renard à celui de Manche d'Épée ainsi que de l'extrémité nord de la route nationale 198, dans la vallée de l'Anse-Pleureuse (Figure 1). Ces deux routes longent respectivement le littoral du golfe du Saint-Laurent et le lac de l'Anse-Pleureuse tout en étant surplombées par des escarpements rocheux du bas plateau gaspésien. L'emplacement de la route 132 fait en sorte qu'elle est sujette aux aléas de submersion marine et d'érosion du littoral (Drejza et al., 2014), aux avalanches de neige (Fortin et al., 2011; Gauthier et al., 2017; Hétu, 2007a), aux chutes de blocs de glace (Gauthier et al., 2015), aux coulées de débris (Fortin et al., 2015) et aux chutes de pierres (Laliberté et al., 2022). L'emplacement de la route 198 est aussi problématique, puisque des avalanches de neige, des chutes de blocs de glace et des chutes de pierres l'atteignent également fréquemment au niveau du lac de l'Anse-Pleureuse (Gauthier et al., 2017, 2015; MTQ, 2021). Selon les données de 2017, le débit journalier moyen à la jonction de ces deux routes variait entre 780 automobilistes en hiver et 1540 automobilistes en été, dont 15% de véhicules lourds incluant le transport de turbines d'éoliennes (Données Québec, 2022). La route nationale 132 est également le seul axe de transport qui permet de relier certains villages au reste de la région et est donc indispensable pour permettre aux populations locales d'avoir accès aux services essentiels.

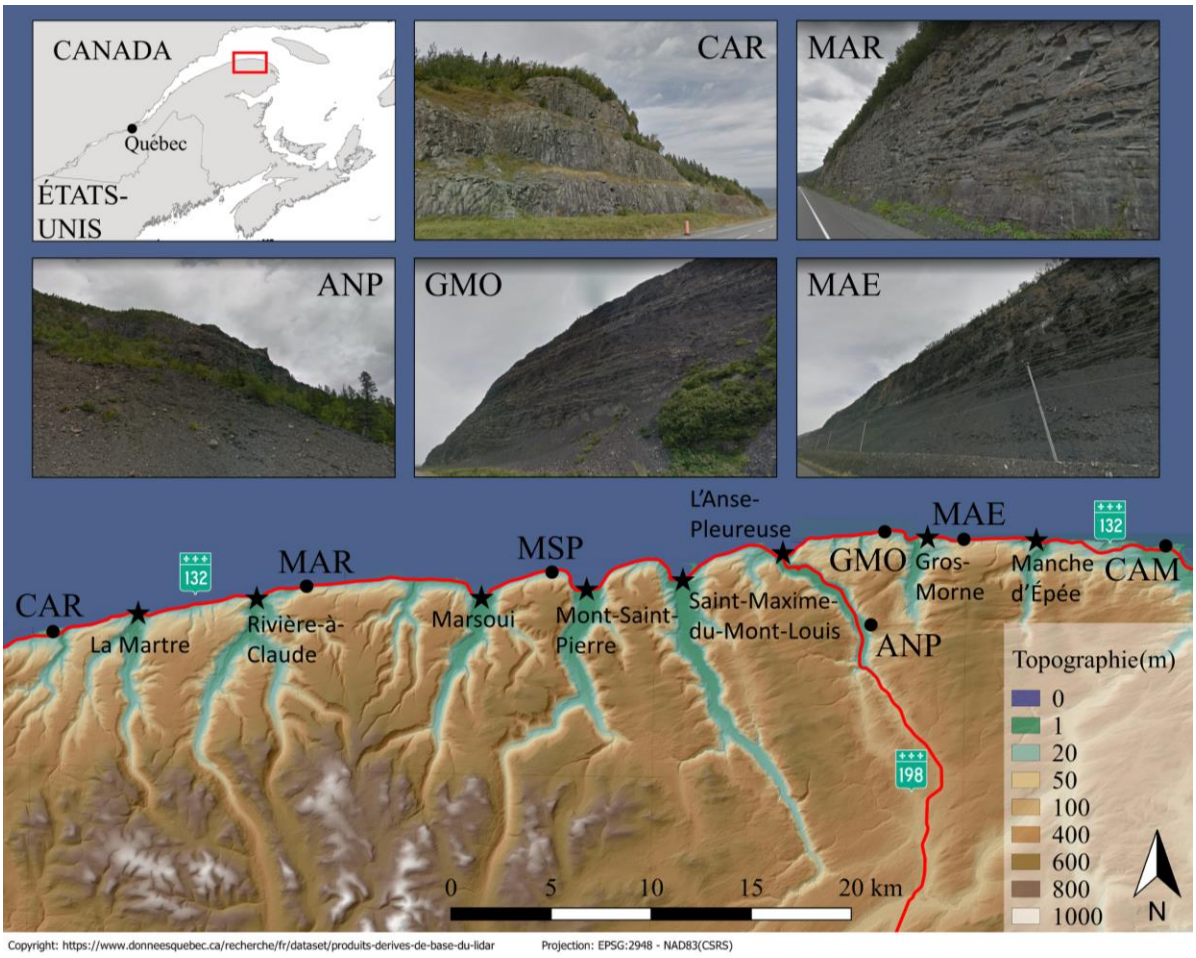

Figure 1. Carte de localisation de la région d'étude avec les cinq parois rocheuses instrumentées. D'est en ouest : MAE, GMO, ANP, MAR, CAR. Cette instrumentation est complétée par la station météorologique MSP située à la halte routière de Mont-Saint-Pierre.

Afin de limiter le risque pour les usagers, le ministère des Transports du Québec (MTQ) a mis en place en 1987 une patrouille qui circule 24h/24 sur les portions problématiques des routes 132 et 198. La vocation de cette patrouille est d'effectuer de la surveillance et de déblayer la route lorsqu'elle est obstruée à la suite d'un mouvement de versant (roche, neige, glace). Entre 1987 et 2020, le MTQ a répertorié plus de 13 000 chutes de pierres sur les 25 km de la route nationale 132 qui sont surplombés par une paroi rocheuse et plus de 3 000 sur la portion de 2 km de la route nationale 198 (Ministère du Transport du Québec, 2021). Ces chiffres positionnent les routes 132 et 198, parmi les axes routiers les plus exposés à cet aléa

au Québec et rappellent les chiffres avancés sur divers axes routiers et ferroviaires en Colombie-Britannique (Bunce et al., 1997; Hungr et al., 1999).

La base de données événementielles du MTQ révèle toutefois une grande variabilité saisonnière dans la fréquence des chutes de pierres (Figure 2). La majorité des interventions de la patrouille se produit au printemps, lors du dégel des parois rocheuses alors que la période hivernale est caractérisée par une grande stabilité. Après le dégel printanier, des fréquences soutenues des chutes de pierres se produisent durant ou suivant des événements de pluie de forte intensité (Gauthier et al., 2022a, 2022b). Ces résultats préliminaires, comparables aux travaux de Macciotta (2013, 2015) dans la chaîne Côtière canadienne, mettent en évidence le rôle prépondérant des conditions météorologiques sur la fréquence des chutes de pierres.

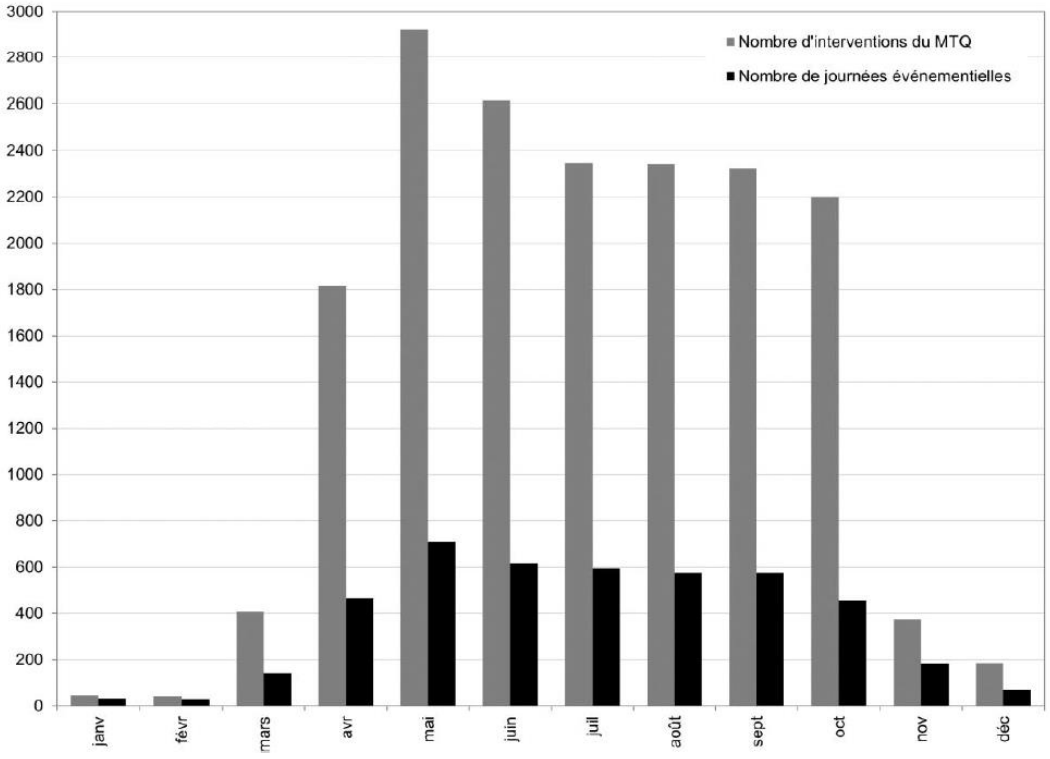

Figure 2. Fréquence mensuelle d'interventions du MTQ et de journées événementielles entre 1987 et 2019 (Gauthier et al., 2022b).

En raison des défis techniques, financiers et environnementaux que représenterait la relocalisation de ces routes, cette option n'est pas priorisée par le MTQ. Par contre, une compréhension approfondie de la relation entre les conditions météorologiques et le développement des chutes de pierres pourrait servir de base au développement d'une gestion préventive du risque naturel (Gauthier et al., 2018; Laliberté et al., 2022). La mise en place d'une gestion préventive par les gestionnaires du MTQ, permettrait de diminuer la vulnérabilité des usagers des routes et ainsi, d'augmenter leur résilience face à l'aléa chute de pierres (Gauthier et al., 2022b; Laliberté et al., 2022).

2. CADRE THÉORIQUE

2.1 Mouvements de versant et chutes de pierres

Un mouvement de versant est un phénomène physique de déplacement de matériel survenant instantanément après la rupture des forces résistances qui maintenaient la portion nouvellement déstabilisée stable (Hungr et al., 2014; Jarman, 2006; Varnes, 1978). Les mouvements de masse sont généralement caractérisés par plusieurs épisodes de déplacement, séparés par des périodes plus ou moins longues de stabilité relative. Dans les massifs rocheux, la rupture correspond au mouvement le plus significatif qui survient après une diminution des forces résistantes ou après une augmentation des contraintes de cisaillement le long d'une discontinuité (Hungr et al., 2014; Jarman, 2006; Wieczorek, 1996). Ces instabilités rocheuses peuvent prendre de nombreuses formes (Viles, 2013). Les déformations, les basculements, les chutes de pierres, les écroulements, les avalanches rocheuses, les glissements et les étalements rocheux sont les principaux types de mouvement qui se produisent sur les versants rocheux (Giani, 1992; Highland et Bobrowsky, 2008; Hungr et al., 2014; Varnes, 1978). La magnitude de ces instabilités est très variable (centimétrique à plusieurs millions de mètres cubes) et le mouvement peut se produire à de grandes vitesses (chutes de pierres, avalanches

rocheuses) ou plus lentement et progressivement (déformation, étalement ou glissement rocheux) (Viles, 2013).

Cette étude porte spécifiquement sur les chutes de pierres, qui peuvent être définies comme étant des mouvements de versant mobilisant des blocs superficiels qui se détachent d'un escarpement rocheux (Budetta, 2004; Michoud et al., 2012; Piteau et Peckover, 1978; Selby, 1982). Les propriétés du massif rocheux telles que la lithologie, le degré d'altération, les caractéristiques du réseau de discontinuités et la pente prédisposent le mode de rupture (chute de surplomb, glissement planaire ou en coin, basculement) et la magnitude des instabilités rocheuses (Selby, 1982; Turner et Schustler, 1996).

2.2 Risque naturel et mesures de mitigation

Le bureau des Nations Unies pour la réduction des risques de catastrophes (UNDRR) (2022) défini le risque naturel comme étant un « processus naturel qui peut causer des pertes de vies humaines, des blessures ou d'autres effets sur la santé, des dommages aux biens, la perte de moyens de subsistance et de services, des perturbations socio-économiques, ou des dommages à l'environnement ». En raison des caractéristiques peu prévisibles des instabilités rocheuses, la capacité de prendre des mesures d'évitement est pratiquement nulle lorsqu'un événement se produit (Volkwein et al., 2011). L'occurrence des chutes de pierres étant quotidienne dans les régions montagneuses (Dorren, 2003), de nombreux exemples d'infrastructures endommagées ou de personnes tuées par des chutes de pierres sont décrits dans la littérature (e.g. Badger et Lowell, 1992; Badoux et al., 2016; Bunce et al., 1997; Chau et al., 2003; Hilker et al., 2009; Mourey et al., 2022; Porter et Orombelli, 1980).

La résilience est définie comme étant « la capacité d'un système, d'une communauté ou d'une société exposée à des aléas à résister, absorber, s'adapter, se transformer et se remettre des effets d'un aléa rapidement et efficacement, y compris par la préservation et la restauration de ses structures de base essentielles et de ses fonctions par l'intermédiaire de la

gestion de risques » (UNDRR, 2022). Afin de bien évaluer le risque que constitue les chutes de pierres, Scavia et al. (2020) proposent une procédure détaillée qui passe notamment par l'identification des zones sources et des trajectoires possibles des blocs qui chutent. Selon l'intensité de l'aléa et la vulnérabilité des enjeux, le risque peut être considéré comme « acceptable » ou « tolérable ». Le cas échéant, des mesures de mitigation doivent être mises en place pour améliorer la résilience des sociétés humaines face aux chutes de pierres. À travers le monde, différentes méthodes sont utilisées. Les mesures de mitigation les plus courantes sont variées et ont vocation à réduire soit la probabilité d'occurrence des instabilités rocheuses directement, soit la probabilité de conséquences négatives de ces chutes de pierres. En pied de versant, la construction de risbermes, le reprofilage de pente et l'installation de clôtures de captage sont les mesures les plus couramment utilisées. Sur les versants, l'écaillage mécanique, la pose d'ancrages, de structures drapées en treillis d'acier ou de résines de polyuréthane sont les méthodes les plus communes (Peckover et Kerr, 1977; Wyllie et Mah, 2004). L'efficacité de ces mesures peut être évaluée selon le « risque résiduel » qui correspond au risque qui subsiste après leur mise en place (UNDRR, 2022).

Weidner et Walton (2021) montrent que dans le contexte de parois rocheuses mal consolidées, déformées et hautement fracturées, les mesures de mitigation telles que le nettoyage mécanique, la stabilisation par des ancrages, la pose de clôtures ou l'injection de résines de polyuréthane, peuvent s'avérer inefficaces et que le risque résiduel demeure important. Ils observent même des fréquences de chutes de pierres plus élevées après l'implantation de ces mesures de mitigation. Ils notent par exemple, que les nouvelles surfaces exposées à la suite d'opérations de nettoyage peuvent être tout autant altérées et instables que les surfaces anciennement exposées. De plus, les mesures traditionnelles seraient peu efficaces dans le cas des instabilités de faible et de moyenne magnitudes ($<1 m^3$) (Weidner et Walton, 2021; Wyllie et Mah, 2004). Pour les parois rocheuses hautement altérées, la mise en place d'une gestion préventive du risque, basée sur les facteurs qui déclenchent les instabilités rocheuses, pourrait être la façon la plus efficace de limiter le risque associé aux chutes de pierres et donc d'augmenter la résilience des populations vulnérables. Ce type de gestion novateur pourrait également constituée une bonne alternative

aux mesures traditionnelles lorsque les ressources financières ne sont pas disponibles pour la mise en place et l'entretien de ces infrastructures (Peckover, 1975; Peckover et Kerr, 1977).

2.3 Quantifier les chutes de pierres

La mise en place d'une gestion préventive nécessite au préalable, une très bonne compréhension de l'aléa (Dorren, 2003; Erismann et Abele, 2001; Mourey et al., 2022; Scavia et al., 2020). L'étude de la dynamique des parois rocheuses s'est longtemps avérée problématique en raison de leur faible accessibilité et de leur dangerosité (Abellán et al., 2014). Les chutes de pierres ont pu être quantifiées directement dans les talus sous les parois par dendrochronologie (Brázdil et al., 2012), ou récoltées dans des filets métalliques (Krautblatter et Moser, 2009) et dans des quadrats (Douglas, 1980) disposés sur le sol ou enfin en utilisant le manteau neigeux comme collecteur naturel (Matsuoka et Sakai, 1999). Des filets métalliques suspendus (Sass, 2005b) et de la peinture (Matsuoka, 1990) à la surface de certaines portions de parois rocheuses ont permis de quantifier les chutes de pierres directement sur les parois. Ravanel et Deline (2011) ont également comparé des photographies anciennes et récentes pour répertorier les chutes de pierres de la face nord des Aiguilles de Chamonix. Ces méthodes ne permettent pas toujours d'évaluer adéquatement le risque posé par les chutes de pierres, notamment dans le cas des versants rocheux à la topographie complexe pour lesquelles la zone source n'est pas visible depuis le sol (Lato et al., 2015). Le développement récent de technologies de télédétection a permis de cartographier la surface des parois rocheuses et de quantifier la dynamique des chutes de pierres (Abellán et al., 2014; D'Amato et al., 2016; Guerin et al., 2014; Lato et al., 2015; van Veen et al., 2017). Ces technologies permettent d'effectuer des levés topographiques sur de vastes surfaces avec une bonne précision et une très haute résolution (Abellán et al., 2014; Santana et al., 2012; Williams et al., 2018). Les scanners laser LiDAR (« Light Detection And Ranging ») et la photogrammétrie sont les deux technologies de télédétection les plus communément utilisées pour cartographier la surface des parois rocheuses (e.g. Williams et

al. 2018, Kromer et al. 2019, Anders et al. 2020, Weidner et Walton 2021). L'acquisition de données peut se faire depuis le sol (e.g. van Veen et al. 2017) mais la récente émergence des drones facilite également les relevés aériens (e.g. Lato et al. 2015). En combinant les nuages de points issus de ces relevés, on peut d'une part, identifier les instabilités rocheuses qui sont survenues entre ces relevés (e.g. van Veen et al. 2017) et d'autre part, mettre en évidence le développement de futures instabilités rocheuses (e.g. Oppikofer et al. 2008, 2009, Royán et al. 2014, Kromer et al. 2018). Ces technologies ont déjà fait leurs preuves pour quantifier les chutes de pierres de différentes magnitudes qui surviennent à la surface de différentes parois rocheuses (e.g. Hungr et al. 1999, Rosser et al. 2005, Santana et al. 2012, Guerin et al. 2014, 2020, van Veen et al. 2017, Williams et al. 2018). La fréquence et la résolution spatiale des relevés LiDAR ou photogrammétriques doivent être suffisamment importantes pour identifier individuellement les chutes de pierres et ne pas sous représenter les instabilités de faibles magnitudes (Barlow et al., 2012; Guerin et al., 2014; Malamud et al., 2004).

2.4 Quantifier les facteurs déclencheurs des chutes de pierres

Les technologies de télédétection ne permettent pas à elles seules d'expliquer les chutes de pierres. Elles doivent être mises en relation avec les facteurs qui déclenchent ces instabilités. Ces dernières résultent d'un relai de processus qui interagissent sur de longues périodes (Schovanec, 2020; Viles, 2013), elles ne sont jamais l'unique résultat du changement apparent le plus récent (Draebing et Krautblatter, 2019; Gunzburger et al., 2005). De nombreux facteurs peuvent contribuer à leur développement et c'est notamment le cas des précipitations et des cycles gel-dégel qui sont fréquemment cités dans la littérature (e.g. Rapp 1960, Peckover et Kerr 1977, Coutard et Francou 1989, Wieczorek et Jäger 1996, Hungr et al. 1999, Matsuoka et Sakai 1999, Macciotta et al. 2015, Collins et Stock 2016, D'Amato et al. 2016). L'apport d'eau provenant des précipitations est susceptible d'entraîner une augmentation de la pression hydrostatique dans les massifs rocheux qui peut se traduire par une diminution de la résistance au cisaillement (Selby, 1993; Wieczorek et Jäger, 1996;

Wyllie et Mah, 2004) et conduire à des chutes de pierres (D'Amato et al., 2016; Delonca et al., 2014; Matsuoka, 2019; Wieczorek et Jäger, 1996). Les mécanismes inhérents à la cryoclastie, soit l'expansion volumétrique causée par le gel de l'eau dans les pores et dans les discontinuités de la roche ainsi que la ségrégation de la glace, contribuent grandement à l'altération des versants rocheux (Draebing et al., 2017; Matsuoka et Murton, 2008; McGreevy et Whalley, 1985; Walder et Hallet, 1986) et au développement d'instabilités rocheuses (Coutard et Francou, 1989; Matsuoka, 2008; Matsuoka et Sakai, 1999).

L'influence des conditions météorologiques sur le développement des chutes de pierres fait aujourd'hui consensus mais il reste néanmoins souvent difficile de quantifier leur rôle respectif (Schovanec, 2020). Les technologies modernes permettent de quantifier précisément les instabilités rocheuses, mais elles ne sont pas toujours mises en relation avec des données météorologiques adaptées (Birien et Gauthier, 2022). Par exemple, les cycles gel-dégel sont souvent déduits de la température de l'air sans tenir compte de l'influence du rayonnement solaire, même pour des parois rocheuses exposées au sud (e.g. Weidner et Walton 2021). Pourtant, la température de surface de la roche ne peut pas être déduite convenablement de la température de l'air (e.g. Hall 1997, Gruber et al. 2003, Draebing et Mayer 2021) car d'autres facteurs exercent une influence majeure sur cette température. La topographie contrôle l'exposition au rayonnement solaire d'une paroi rocheuse alors que la rugosité et la couleur des roches en surface contrôlent l'absorptivité de l'énergie de ce rayonnement (Gruber et al., 2004b; Hall et al., 2005; Hasler et al., 2011; Schnepfleitner et al., 2018). L'absence d'information sur le régime thermique des parois rocheuses peut également être problématique pour suivre l'évolution du front de gel saisonnier et pour mettre en relation le dégel printanier avec les chutes de pierres qui surviennent (e.g. Macciotta et al. 2015). La propagation du signal thermique absorbé par la surface à différentes profondeurs dépend de la conductivité, de la capacité et de la diffusivité thermique de la paroi rocheuse, elles-mêmes dépendantes de la lithologie, du degré d'altération de la roche (porosité, fractures) et de sa saturation en eau (Schnepfleitner et al., 2018). Des mesures de température entre la surface et la profondeur maximale atteinte par le front de gel saisonnier permettent

de mesurer la distribution du gel et du dégel dans la paroi rocheuse et de quantifier l'efficacité de la cryoclastie à différentes profondeurs.

La relation entre les conditions météorologiques et le développement des instabilités rocheuses est souvent étudiée à l'échelle mensuelle voire saisonnière (e.g. Macciotta et al. 2017, Kromer et al. 2018, Pratt et al. 2019). Cette temporalité ne correspond pas à la durée des principaux phénomènes météorologiques et n'est donc pas adaptée pour discriminer l'influence d'un facteur météorologique par rapport à un autre.

Enfin, les études qui s'intéressent à l'influence des variables météorologiques sur la dynamique des parois rocheuses se concentrent presque uniquement sur la fréquence des chutes de pierres (e.g. Delonca et al. 2014, D'Amato et al. 2016, Pratt et al. 2019) et n'abordent que très peu la problématique de la magnitude alors même que les dommages causés par les instabilités rocheuses sont proportionnels à leurs magnitudes. Pour quantifier l'influence de ces conditions météorologiques sur le développement des instabilités qui affectent les parois rocheuses, elles doivent être mesurées localement et adéquatement.

2.5 Influence du réchauffement climatique contemporain

Le réchauffement climatique planétaire est particulièrement intense dans les hautes latitudes ainsi qu'en altitude (Hartmann et al., 2013). Cette augmentation de la température de l'air modifie la distribution du gel et du dégel dans les massifs rocheux et de ce fait, l'efficacité du processus de cryoclastie (Rode et al., 2016). De nombreuses études à travers le monde, et notamment dans les Alpes, montrent que ces changements ont des répercussions déjà visibles sur la fréquence des chutes de pierres de différentes magnitudes (e.g. Gruber et al. 2004, Gruber et Haeberli 2007, Harris et al. 2009, Huggel 2009, Ravanel et Deline 2011, Huggel et al. 2012, Gobiet et al. 2014, Paranunzio et al. 2016, Hartmeyer et al. 2020).

À l'échelle du Canada, Cloutier et al. (2016) évoquent un réchauffement de 1,6°C entre 1948 et 2014. Dans le nord de la Gaspésie, un réchauffement de 0,95°C a été enregistré entre

1950 et 2020 (Environnement Canada, 2021). Ce réchauffement climatique n'en est qu'à ses prémices (Collins et al., 2013; Hartmann et al., 2013) et des répercussions majeures peuvent être anticipées sur la dynamique des chutes de pierres d'ici la fin du 21ème siècle. Noetzli et al. (2007) montrent que même si du pergélisol relique pourrait subsister pendant des siècles en profondeur malgré les changements climatiques, il se dégraderait très rapidement proche de la surface des massifs rocheux. Rode et al. (2016) ont comparé dans les Alpes autrichiennes, les périodes favorables à l'occurrence des processus de fracturation par le gel en 2010 et en 2100. Ils montrent que d'ici la fin du 21ème siècle, les périodes favorables à l'efficacité de ces processus devraient se raréfier à basse altitude mais qu'en raison des redoux plus fréquents et de la plus grande disponibilité en eau liquide, ces périodes devraient s'allonger dans le pergélisol. À ce jour, aucune étude ne quantifie l'évolution de l'efficacité de l'altération par le gel dans les massifs rocheux dans le contexte des changements climatiques contemporains et les études qui discutent de l'évolution de la fréquence et de la magnitude des instabilités rocheuses au cours du 21ème siècle restent spéculatives (e.g. Gruber et al., 2004b; Huggel, 2009; Ravanel et Deline, 2011).

3. OBJECTIFS DE RECHERCHE

L'objectif principal de cette thèse est d'améliorer notre compréhension de l'influence des conditions météorologiques sur le développement des instabilités rocheuses et d'anticiper le rôle du réchauffement climatique contemporain sur cette dynamique.

D'un point de vue scientifique, les connaissances acquises au cours de ce projet permettront de mieux cerner les mécanismes de développement des instabilités rocheuses qui n'ont jamais été documentés localement. Elles pourront également s'exporter aux parois de roche caractérisées par des lithologies et des structures apparentées, soumises à des conditions météorologiques typiques des environnements de moyennes latitudes (e.g. gel saisonnier, cycles gel-dégel sporadiques). Cette étude est la première à mettre en relation des conditions météorologiques précises et mesurées adéquatement avec une quantification tout

aussi rigoureuse i) des déformations mécaniques pré-rupture qui se produisent à la surface de la paroi rocheuse, ii) de la fréquence et iii) de la magnitude des chutes de pierres. Elle apporte également, dans le contexte du réchauffement climatique, une meilleure connaissance de l'évolution des périodes d'occurrence, de la fréquence et de la magnitude des chutes de pierres attendues d'ici la fin du 21ème siècle.

D'un point de vue opérationnel, l'objectif est de développer une classification des conditions météorologiques en fonction de leur capacité à déclencher des instabilités rocheuses de différentes magnitudes. Dans une optique de gestion du risque naturel, s'intéresser à la relation entre la magnitude des instabilités rocheuses et les facteurs qui les déclenchent est essentielle puisque les dommages causés par ces instabilités sont proportionnels à leur magnitude. Ce projet apportera les connaissances scientifiques nécessaires à la mise en place d'une gestion préventive des chutes de pierres, basée sur les facteurs qui les déclenchent. Un tel outil de gestion, à destination des gestionnaires du MTQ, permettrait de diminuer la vulnérabilité des usagers des routes nationales 132 et 198 et ainsi, d'augmenter leur résilience face aux chutes de pierres. Enfin, cette étude apportera des connaissances essentielles afin d'anticiper l'influence des changements climatiques à venir sur l'évolution des périodes stables et des périodes propices des chutes de pierres.

Pour y parvenir, ce projet de doctorat s'articule autour des objectifs spécifiques suivants :

1. Quantifier et discriminer l'influence respective des conditions météorologiques sur les déformations mécaniques qui affectent la surface des parois de roche sédimentaire stratifiée (flysch) ;

2. Expliquer la dynamique d'érosion différentielle et le développement des instabilités rocheuses dans les flyschs ;

3. Quantifier et discriminer l'influence respective des conditions météorologiques sur la fréquence et sur la magnitude des chutes de pierres des parois de roche sédimentaire ;

4. Développer une classification des conditions météorologiques en fonction de leur niveau de préoccupation dans une optique de gestion préventive du risque ;

5. Mesurer le régime thermique des parois rocheuses à fine échelle temporelle et le modéliser afin de quantifier la distribution du gel et du dégel dans les parois rocheuses ;

6. Évaluer l'influence du réchauffement climatique contemporain sur le régime thermique des parois rocheuses et sur la capacité du processus de cryoclastie à fracturer la roche et à générer des chutes de pierres de différentes magnitudes en Haute-Gaspésie.

4. TERRITOIRE À L'ÉTUDE ET INSTRUMENTATION

Le territoire à l'étude s'étend sur une distance de 64 km le long du rivage du golfe du Saint-Laurent, entre les villages de Cap-au-Renard et de Manche d'Épée ainsi que le long du lac de l'Anse-Pleureuse (≈ 2 km) (Figure 1). Ce territoire est situé sur la côte nord de la péninsule gaspésienne, à l'extrémité continentale de la ceinture plissée des Appalaches, à l'endroit où les monts Chics-Chocs rencontrent le golfe du Saint-Laurent (Hétu et Gray, 2000b). Le relief local est dominé par des vallées glaciaires (Hétu et Gray, 1985) qui séparent des plateaux rocheux culminant entre 400 et 600 m d'altitude. La jonction entre ces plateaux et le golfe du Saint-Laurent se matérialise par d'imposantes parois rocheuses (Figure 1). Taillées dans les flyschs ordoviciens, ces parois sont principalement constituées d'une alternance de strates de grès, de grauwacke, de siltstone et de shale pélagique d'épaisseurs pluri-décimétriques (Enos, 1969b, 1969a). Ces roches, hautement fissiles, favorisent une grande densité du réseau de discontinuités des parois rocheuses (Hétu et Vandelac, 1989). Localement, des portions de conglomérat du Cambro-Ordovicien sont également présentes (Bernstein et al., 1992). D'après la caractérisation des parois rocheuses que nous avons effectuée en 2019 (Gauthier et al., 2020), sur les 64 km de la route nationale 132 qui relient

le village de Cap-au-Renard à celui de Manche d'Épée, 25 km sont surplombés par des parois rocheuses dont 5 km qui sont des parois anthropisées (dynamitées).

Dans le secteur du lac de l'Anse-Pleureuse, la route nationale 198 est surplombée par des parois rocheuses naturelles sur une distance totale de 5,7 km. La majorité de ces parois rocheuses ont une structure sub-horizontale (ou légèrement anaclinale). Une très faible proportion présente des structures cataclinales propices aux glissements rocheux ou des structures complexes associées à la présence de plis ou de failles (Brisebois and Nadeau, 2003; Gauthier et al., 2020).

Afin de répondre aux objectifs spécifiques du projet, cinq parois rocheuses ont été instrumentées à proximité des villages de Cap-au-Renard (CAR), de Marsoui (MAR), de l'Anse-Pleureuse (ANP), de Gros-Morne (GMO) et de Manche d'Épée (MAE) (Figure 1). La localisation ainsi que les principales caractéristiques lithologiques et structurales des sites instrumentés sont présentées dans le Tableau 1. Ces sites ont été sélectionnés en tenant compte des critères suivants :

1. Leurs caractéristiques structurales et lithologiques sont représentatives des parois rocheuses de la Haute-Gaspésie ;

2. Leurs morphologies (verticalité, hauteur) et leurs microtopographies (rugosité) sont compatibles avec l'acquisition de relevés LiDAR depuis la route. L'absence de végétation (zone d'occlusion) et d'écoulement d'eau (réflexion du signal) ont également été considérés.

3. Leurs expositions au rayonnement solaire sont diversifiées ;

4. Les chutes de pierres provenant de ces parois atteignent fréquemment la route ;

5. Les sites sont accessibles à toutes les saisons pour effectuer la maintenance des instruments et les relevés topographiques.

Tableau 1. Caractéristiques des cinq parois rocheuses instrumentées. « cm » est pour « centimétrique », « dm » est pour « décimétrique », « m » est pour « métrique ».

	ANP	CAR	GMO	MAE	MAR
Localisation	49°13'53.1"N 65°36'50.9"W	49°11'41.1"N 66°13'41.2"W	49°15'22.3"N 65°33'45.2"W	49°15'13.1"N 65°32'06.3"W	49°13'23.1"N 66°01'17.8"W
Route exposée	198	132	132	132	132
Type de paroi	Naturelle	Dynamitée	Naturelle	Naturelle	Dynamitée
Lithologie	Siltstone, grauwacke	Conglomérat	Grauwacke, siltstone, shale	Siltstone, grauwacke, shale	Grès, siltstone, shale
Épaisseur des strates	dm	m	cm à dm	cm à m	cm à m
Plan de statification	Plissé	Anaclinal	Anaclinal	Anaclinal	Anaclinal
Hauteur	35 m	20 m	55 m	80 m	30 m
Pente	80°	90°	80°	80°	90°
Orientation	SO	SE	NO	N	N

Des microstations météorologiques ont été installées directement à la surface des parois rocheuses instrumentées (Figure 3). Ces stations mesurent la température de l'air, l'humidité relative, le rayonnement solaire incident et réfléchi, la vitesse et la direction du vent. En complément, le rayonnement incident et réfléchi de longue longueur d'onde, la pression atmosphérique et les précipitations sont mesurées par une station météorologique conventionnelle située à 30 m d'altitude le long du littoral à la halte routière de Mont-Saint-Pierre. Des grappes de thermistances ont également été introduites dans des puits de forages perpendiculaires à la surface des parois rocheuses (Figure 3). Une thermistance mesure la température tous les 30 cm jusque 300 cm de profondeur pour les parois rocheuses de CAR, MAR et GMO et jusque 550 cm de profondeur pour la paroi rocheuse de MAE. Le site de l'ANP étant difficilement accessible, la température est seulement mesurée jusqu'à 55 cm de

profondeur. L'instrumentation du site de GMO est complétée par une sonde qui mesure la teneur en eau à la surface de la roche et par des extensomètres qui mesurent les déformations mécaniques qui se produisent à la surface de la paroi rocheuse (Figure 3). Des photographies de la foreuse développée par la Laboratoire de géomorphologie et de gestion des risques en montagne (LGGRM), d'une tige de thermistance, de microstations météorologiques et d'extensomètres en paroi rocheuses sont présentées sur la Figure 3 et l'ensemble de l'instrumentation du projet est détaillée dans le Tableau 2.

D'après la classification de Köppen, la Haute-Gaspésie est caractérisée par un climat continental, humide à été court et frais (Beck et al., 2018). Sur la période 1991-2020, la température moyenne annuelle s'établit à 3,9°C, la température moyenne du mois le plus chaud à 16,3°C (juillet) et la température moyenne du mois le plus froid à -9,2°C (janvier). Sur cette même période de 30 ans, les précipitations annuelles culminent à 888 mm dont 33% tombent sous forme de neige (Environnement Canada, 2021). L'exposition nord de la grande majorité des parois rocheuses qui bordent la route 132 limite l'influence du rayonnement solaire sur la température de la roche. Ces parois demeurent ombragées toute la journée de la mi-octobre à la mi-mars avant d'être de nouveau exposées au rayonnement solaire en fin d'après-midi. Les quelques parois rocheuses qui bordent la route 198(Gauthier et al., 2020) sont exposées sud et davantage influencées par le rayonnement solaire. Le contexte climatique nord-gaspésien est propice à la météorisation par cryoclastie (Trenhaile et Rudakas, 1981). La présence de roches riches en argile (shale) favorise également le processus d'hydratation et de déshydratation par adsorption et désorption d'eau entre les feuillets d'argile (Trenhaile, 2006) L'action répétée du gel-dégel et de l'hydratation-déshydratation induit une contrainte suffisante dans la roche pour favoriser sa fragmentation (e.g. Dunn and Hudec, 1972; Hall et al., 2002). Cette prédisposition climatique est propice au développement des instabilités rocheuses.

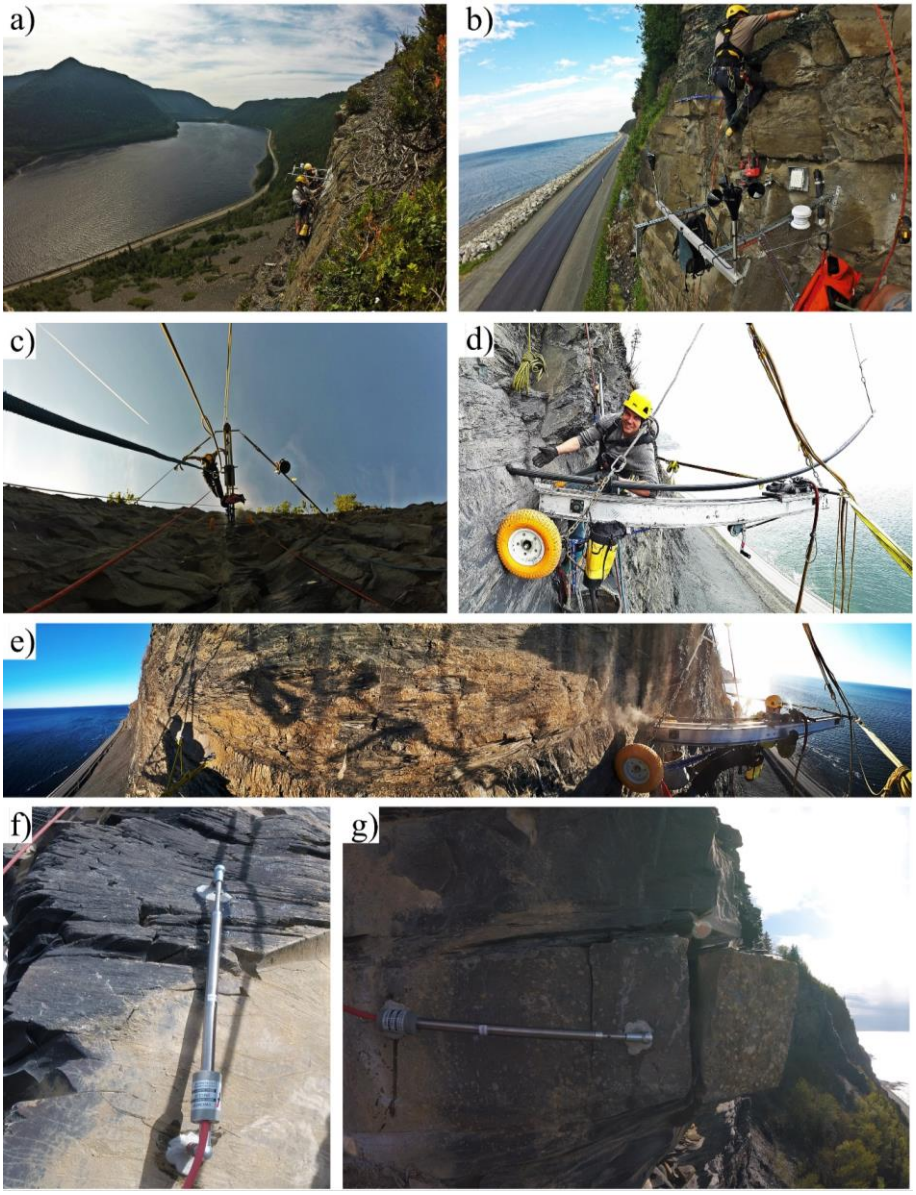

Figure 3. a) Station micrométéorologique de l'ANP avec en arrière-plan le talus d'éboulis, la route nationale 198 et le lac de l'Anse-Pleureuse ; b) station micrométéorologique installée sur la paroi rocheuse dynamitée de MAR avec la route nationale 132 en arrière-plan ; c) vue de la foreuse stabilisée sur la paroi rocheuse dynamitée de CAR ; d) tige de thermistances de 550 cm insérée dans un puit de forage horizontal sur la paroi rocheuse de MAE ; e) vue latérale de la foreuse en opération sur la paroi rocheuse de MAE avec la route nationale 132 en arrière-plan ; f) extensomètre vertical encadrant un segment de siltstone hautement altéré sur la paroi rocheuse de GMO ; et g) extensomètre horizontal positionné dans une strate de grès avec une fracture persistante et ouverte dans le haut de la strate.

Tableau 2. Ensemble des instruments installés sur les parois rocheuses de l'ANP, CAR, GMO, MAE et MAR ainsi que sur le site de GMO qui ont été utilisés dans le cadre de ce projet.

Donnée	Unité	Instrument (Fabriquant)	Précision	Sites
Température de l'air	°C	Senseur de température de l'air TMC6-HD + protecteur de rayonnement solaire M-RSA (HOBO par Onset)	±0.25°C	ANP, CAR, GMO, MAE, MAR
Température de la roche	°C	Tige de thermistances 915 MHz + collecteur de données M-Log5W-DALLAS-US (Geoprecision)	±0.25°C	ANP, CAR, GMO, MAE, MAR
Rayonnement solaire incident Rayonnement solaire réfléchi	W/m²	Pyranomètre S-LIB-M003 (HOBO par Onset)	±10 W/m²	ANP, CAR, GMO, MAE, MAR
Vitesse du vent et des rafales Direction du vent	m/s Ø	Senseur S-WSET-B (Onset)	± 1.1 m/s ± 5 degrés	ANP, CAR, GMO, MAE, MAR
Rayonnement infrarouge incident Rayonnement infrarouge réfléchi	W/m²	Pyrgéomètre SN-500-SS (Apogee Instruments)	±8.5 W/m²	MSP
Pression atmosphérique	mbar	Baromètre S-BPB-CM50 (Onset)	±5.0 mbar	MSP
Précipitations	Pouces	Pluviomètre TE525WS-L + adaptateur pour précipitations solides CS705 (Campbell)	±1% à des taux >1 in./hr	MSP
Teneur en eau à la surface de la roche	m³/m³	Senseur S-SMC-M005 (Onset)	±3%	GMO
Déformations de la roche	mm	Extensomètre (RST)	0.1 mm	GMO

5. PRÉSENTATION DES CHAPITRES

Cette thèse de doctorat s'articule autour de trois chapitres présentés sous la forme d'articles scientifiques. Ces chapitres permettent de répondre aux principaux objectifs de ce projet, préalablement définis dans la partie Objectifs de recherche. Le premier chapitre s'intitule « Influence des variables météorologiques sur les déformations des roches sédimentaires conduisant à l'érosion différentielle des parois rocheuses ». Les déformations majeures mesurées à l'aide des extensomètres ont été identifiés et mises en relation avec les conditions météorologiques occurrentes. Ce chapitre permet de répondre aux objectifs (1) et (2) cités préalablement. Le second chapitre s'intitule « Évaluer la relation entre les conditions

météorologiques et les chutes de pierres par l'utilisation du TLS dans une optique de gestion du risque naturel ». Trois parois rocheuses ont été scannées au LiDAR pendant différentes conditions météorologiques ciblées au préalable. Ce chapitre permet de répondre aux objectifs (3) et (4) du projet. Les deux premiers articles de ce projet de doctorat s'articulent bien puisqu'ils s'intéressent aux facteurs responsables de l'altération (article 1) et de l'érosion (article 2) des parois de roches sédimentaires du nord de la Gaspésie.

Le troisième chapitre s'intitule « Influence du réchauffement climatique contemporain sur l'altération par le gel des parois rocheuses sédimentaires stratifiées (flysch). À partir de mesures du régime thermique des premiers mètres de profondeur des parois rocheuses, les cycles gel-dégel superficiels (horaires à plurijournaliers) et saisonnier sont quantifiés à fine échelle spatio-temporelle. Le régime thermique d'une paroi rocheuse a ensuite été modélisé entre 1950 et 2100 et cette modélisation a servi de support à l'analyse de l'influence du réchauffement climatique sur l'évolution de l'efficacité des processus de cryoclastie. En s'appuyant sur les résultats des chapitres 1 et 2, l'évolution des périodes propices aux chutes de pierres et de leur magnitude sont aussi discutées dans cet article. Ce dernier chapitre répond aux objectifs (5) et (6) de ce projet.

La conclusion générale de la thèse est scindée en trois parties. Dans un premier temps, les principales étapes méthodologiques, les résultats notables et la portée scientifique de cette étude sont résumés. Ensuite, la contribution de ce projet à la mise en place d'une gestion préventive des chutes de pierres est synthétisée. Enfin, les perspectives de recherche mises en évidence à partir de ce projet sont identifiées et des recommandations pour les recherches à venir sont proposées.

CHAPITRE 1

INFLUENCE DES VARIABLES MÉTÉOROLOGIQUES SUR LES DÉFORMATIONS DES ROCHES SÉDIMENTAIRES STRATIFIÉES (FLYSCH) CONDUISANT À L'ÉROSION DIFFÉRENTIELLE DES PAROIS ROCHEUSES

1.1 RÉSUMÉ

Les chutes de pierres représentent un danger quasi-permanent pour les infrastructures et pour les usagers des routes du nord de la Gaspésie. Depuis 1987, plus de 17 500 chutes de pierres ont été répertoriées par le ministère des Transports du Québec (MTQ) sur les 25 km de route qui sont surplombées par des parois rocheuses dans cette région. Bien que les instabilités rocheuses soient avant tout des phénomènes gravitaires, d'autres facteurs contribuent à leur développement. Les chutes de pierres résultent d'un relai de processus qui interagissent sur de longues périodes. Elles ne sont jamais l'unique résultat du changement apparent le plus récent. Cette étude vise à mieux comprendre l'influence des conditions météorologiques sur les déformations mécaniques qui affectent les parois de roches sédimentaires stratifiées et qui contribuent à leur érosion. Pour y parvenir, des extensomètres et un réseau de capteurs hydrométéorologiques ont été déployés directement à la surface d'une paroi de flysch. Les déformations mécaniques affectant une strate de grès et une strate de siltstone ont été mesurées, identifiées et mises en relation avec les conditions météorologiques occurrentes. Il en ressort que les déformations irréversibles qui affectent les premiers décimètres de profondeur des parois rocheuses sont principalement induites par les événements de pluie et par la fonte de la neige, par les fluctuations de température autour du point de congélation et dans une moindre mesure, par les fortes variations thermiques. Dans la strate de siltstone argileux, ce sont surtout les variations de teneur en eau qui sont efficaces pour générer des déformations irréversibles. Dans la strate de grès, ces déformations sont

surtout causées par les cycles gel-dégel et par les variations de teneur en eau. Les tendances sur le long terme enregistrées par les extensomètres et les observations sur le terrain mettent en évidence les mécanismes qui conduisent à l'érosion différentielle des séquences de flysch. Le recul et le tassement progressifs des strates de siltstone provoquent la déstabilisation par glissement ou basculement de blocs des strates de grès sus-jacentes. Les résultats de cette étude mettent en évidence l'importance d'étudier la dynamique des parois rocheuses dans son ensemble afin de comprendre les mécanismes qui conduisent au développement des instabilités rocheuses de grandes dimensions qui sont préoccupantes pour la sécurité des usagers des routes.

Mots-clés : paroi rocheuse, flysch, déformation de la roche, altération, érosion, cycle gel-dégel, hydratation-dessication, cycle thermique, extensomètre.

Contribution des auteurs :

Cet article, intitulé « *Influence of climate-dependent variables on deformation and differential erosion of stratified sedimentary rocks* », a été soumis en février 2022 à la revue *Geomorphology*. Il a été révisé en juin 2022 et soumis dans sa version finale en octobre 2022 avant d'être officiellement publié le 15 novembre 2022 *(doi : https://doi.org/10.1016/j.geomorph.2022.108518)*. En tant que premier auteur, j'ai contribué à l'essentiel de la recherche sur l'état de la question, au développement de la méthode, au traitement des données et à la rédaction de l'article. Le professeur Francis Gauthier, second auteur, a fourni l'idée originale, a aidé au développement de la méthode ainsi qu'à la révision de l'article.

1.2 INFLUENCE OF CLIMATE-DEPENDENT VARIABLES ON DEFORMATION AND DIFFERENTIAL EROSION OF STRATIFIED SEDIMENTARY ROCKS

Tom Birien[a], Francis Gauthier[a]

[a] *Département de biologie, géographie, chimie, Centre for Northern Studies (CEN), Université du Québec à Rimouski, Rimouski, Québec, Canada*

Highlights

- The mechanisms of differential erosion were quantified using crack meters;
- Deformations measured by crack meters are correlated to meteorological conditions;
- Wet-dry cycles are the main cause of irreversible deformations in clay-rich rocks;
- Freeze-thaw cycles also result in irreversible deformations;
- The retreat of weak rock strata leads to the cantilevering of stronger rock strata.

Abstract: Rockfalls are major natural hazards for road users and infrastructures in northern Gaspésie (Eastern Canada) where nearly 25 kilometers of road runs along imposing rockwalls. Since 1987, the Ministère des Transports du Québec (MTQ) has reported more than 17 500 rockfalls that have reached the roadway. While rockfalls are primarily gravitational phenomena, other factors contribute to their development. The long-term interaction of a series of processes leads to rock instabilities. They are never caused solely by the most recent visible change. This study aims to better understand the influence of climate-dependent variables on the mechanical deformations that leads to the erosion of stratified sedimentary rock sequences. To achieve this, a flysch rockwall was instrumented with crack meters and a network of hydrometeorological sensors. The major deformations affecting stratum of siltstone and sandstone were identified and correlated with climate-dependent variables. Results highlighted that irreversible deformations in the first decimetres

of rock wall surface are mainly induced by rainfall and snowmelt, by temperature fluctuations around the freezing point and to a lesser extent, by large thermal variations. The water content fluctuations at the rock surface are more effective at generating irreversible deformations in the clayey siltstone strata than freeze-thaw cycles and high amplitude thermal variations. In the sandstone strata, irreversible deformations were primarily caused by freeze-thaw cycles and water content fluctuations at the rock surface. The long-term trends in the sandstone and siltstone strata recorded by crack meters, along with field observations, highlight mechanisms that lead to the development of superficial rock instabilities in this type of geology. Our results show that the retreat and settlement of the weak rock strata (clayey siltstone) causes the gradual overhang of the resistant rock strata (sandstone). As a result, sandstone blocks will eventually slide or topple on the eroding weak rock strata below. The results of this study underscore the importance of studying rock wall dynamics as a whole to understand the mechanisms that lead to the development of hazardous large-scale rock instabilities.

Keywords: Rock deformation; Mechanical weathering, Thermal cycle, Moisture cycle, Freeze-thaw cycle; Flysch; Crack meter.

1.3 INTRODUCTION

A rockfall is a hillslope movement in which blocks detach and fall from the surface of rocky escarpments (Selby, 1982). Given the unpredictability of rock stability, evasive action is practically impossible when an event occurs (Volkwein et al., 2011). Rockfalls are a daily occurrence in mountainous areas (Dorren, 2003), and the literature contains many examples of the infrastructure damage and human fatalities they cause (e.g., Badger and Lowell, 1992; Badoux et al., 2016; Bunce et al., 1991; Chau et al., 2003; Hilker et al., 2009; Porter and Orombelli, 1980). This hazard must be better understood if we are to reduce the risk to infrastructure and human life (Dorren, 2003; Erismann and Abele, 2001).

While rockfalls are primarily gravitational phenomena, other factors contribute to their development. The long-term interaction of a series of processes leads to rock instabilities. They are never caused solely by the most recent visible change (Draebing and Krautblatter, 2019; Gunzburger et al., 2005). The first step in managing the risk rockfalls pose is to better understand the pre-failure processes that contribute to their development. Variations in the temperature and water content of rock slopes are important contributors to weathering. They are responsible for the thermal cycles in rock (Collins and Stock, 2016; Gischig et al., 2011b; Gunzburger et al., 2005), the shrink-swell process in porous and clayey rock (Cripps and Taylor, 1981; Dunn and Hudec, 1972; Hall, 1986; Hall and Hall, 1996; Vergara and Triantafyllidis, 2016), hydrostatic pressure variations in discontinuities (D'Amato et al., 2016; Terzaghi, 1962) and freeze-thaw cycles in rock masses (Draebing and Krautblatter, 2019; Gruner, 2006; Matsuoka, 2001; Matsuoka et al., 1997). By deforming the rock, these processes can trigger ruptures in rock bridges and increase the opening and persistence of discontinuities (Eberhardt et al., 2004; Eppes and Keanini, 2017; Erismann and Abele, 2001; Gischig et al., 2011a; Terzaghi, 1962). Under their effect, outcrops and superficial rocks are altered and progressively fragment (Ollier, 1984). Thus, these processes are the precursors of rockfall (Draebing, 2021; Eberhardt et al., 2004; Lim et al., 2010).

The influence of meteorological variables on rock deformations that cause fractures in intact rock and expand existing discontinuities has often been assumed but rarely quantified. It is now the subject of a growing number of studies around the world (e.g., Draebing, 2021; Draebing and Krautblatter, 2019; Eppes and Keanini, 2017; Matsuoka, 2008). These studies generally focus on the relationship between a process (e.g. freezing, thermal cycles, moisture fluctuations) and the alteration of a rock segment. Consequently, while the relative contributions of these climate-dependent processes to rock deformation and fracturing remain poorly understood (Hall et al., 2002; Hall et al., 2012; Matsuoka and Murton, 2008; Sass, 2005b), the constraints they place on a rock segment gradually accumulate over time or suddenly combine at a given moment (Anderson, 2005). In general, the role of weathering in the development of instabilities remains to be explored, particularly in stratified sedimentary rock walls, such as flysch (Miščević and Vlastelica, 2014). The differential

weathering of these slopes results in a range of morphologies and failure modes (e.g., topple, slide, falls) depending on their bedding planes and discontinuity patterns (Cano and Tomás, 2013). However, while the differential weathering of sedimentary rock walls is well understood, it does not appear to have been quantified at the stratum level.

Our study aims to better understand the influence of climate-dependent variables on the mechanical deformations that lead to the erosion of stratified sedimentary rock sequences. To achieve this, a flysch sequence on a rock wall in the northern Gaspé Peninsula (Québec, Canada) was instrumented with crack meters and a network of hydrometeorological sensors. Measurements were collected for 27 months and compiled into an extensive database. Using these data, the major deformations affecting the flysch sequence were identified and correlated with the climate-dependent variables. Based on crack meter time series trends and field observations, the relationship between differential weathering and the development of instabilities in the flysch sequence under study is discussed.

1.4 STUDY SITE

In the Haute-Gaspésie region, provincial highway 132 separates a rock wall and talus from the Gulf of St. Lawrence. The highway is subject to many natural hazards: coastal erosion and flooding (Drejza et al., 2019) on one side, snow avalanches (Fortin et al., 2011; Hétu, 2007), ice block falls (Gauthier et al., 2017), debris flows (Fortin et al., 2015), and rockfall on the other. Between 1987 and 2020, the Québec Ministry of Transportation (MTQ) recorded 13 261 rockfall events along the 25 km where rock walls border highway 132 (MTQ, 2021). The region has a humid continental climate with short cool summers, according to the Köppen climate classification system. During the period 1991–2020, it had an annual mean temperature of 3.9°C, and the mean temperatures of the warmest (July) and coldest (January) months were 16.3°C and -9.2°C, respectively. Over those same 30 years, total annual precipitation was 888 mm, 33% of which fell as snow (Environment Canada, 2021). The rock wall has a northwestern (340°) exposure, which limits the influence of solar

radiation on rock temperature. It is in constant shade from mid-October to mid-March when it is once again exposed to the late afternoon sun.

The rock wall under study is 2 km west of the village of Gros-Morne in Haute-Gaspésie, Québec, Canada (49°15'20.5"N 65°33'54.0"W, Figure 4). In the instrumented area, it rises about 45 m at an angle of 80° and has a slope aspect of 340° (north-northwest). The slope is carved from Ordovician flysch composed primarily of alternating pluri-decimetric strata of sandstone, siltstone and pelagic shale (Enos, 1969a; Enos, 1969b). It is slightly anticlinal in structure; the main bedding plane presents a dip of 10° oriented approximately 100° with many fractures running perpendicular to that plane. The slope has no major tectonic deformations (faults or folds) in the study area. According to the Geological Strength Index, it is in Group E (GSI 25 to 35) for heterogeneous rock masses such as flysch (Marinos and Hoek, 2001). It overlooks an approximately 38° talus slope about 40 metres in height. Its upper section is free of vegetation while parts of its lower section are covered in balsam fir. Apart from some pluri-decimetric sandstone blocks that have fallen to its base, it is formed of centimetre-sized flakes with very low sphericity. Many tongues of debris extend as far as the forest at the base of the talus slope.

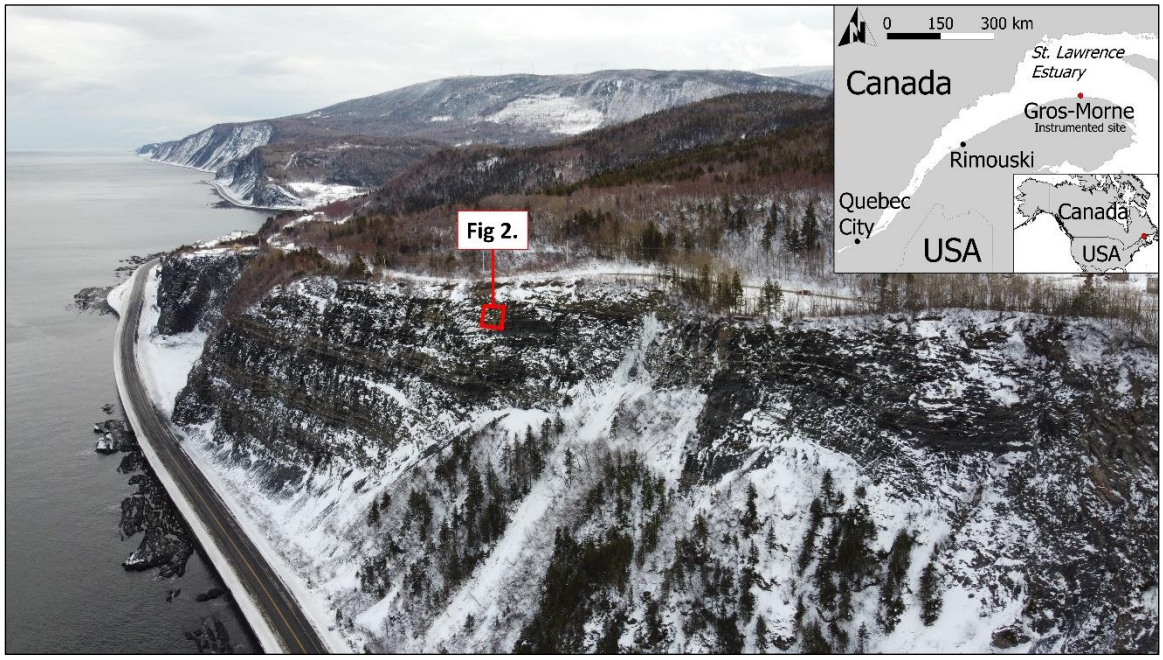

Figure 4. Location and overview of the study site. Red square refers to instrumented section.

1.5 METHODS

The originality of this study lies in its use of data acquired directly on the rock wall to provide an overview of the processes that cause deformations and affect the development of instability in sedimentary rock wall.

1.5.1 Rock deformation

Two RST Instruments Ltd. 1D Vibrating Wire Crack Meters connected to the DT2055B data logger were used to measure rock deformation. Crack meters of this type measure expansion and contraction between two anchor points to a resolution of 1.0 e^{-6} mm. Calibrating the instruments with temperature correction allows movement of 0.1 mm or more to be considered as significant. One instrument was oriented vertically in a stratum of horizontally-layered altered siltstone (Figure 5.1) with an anchor-to-anchor distance of 34.5 cm. The second was oriented horizontally in a sandstone stratum (Figure 5.2) with an anchor-

to-anchor distance of 33 cm. One of its two anchors was set in a block of unstable sandstone, which was detached from the sandstone stratum by a persistent vertical fracture. The fracture opening was wider at the top of the stratum (~4 mm) than at the bottom (~0.5 mm), evidence of minor subsidence of the detached sandstone block. The depth of all anchors is approximately equal to 5 cm. Measurements were recorded every 15 minutes and the USB data downloading was done on-site every three months.

The rock wall under study is characterized by a repeating series of sandstone, shale, and siltstone strata. By instrumenting one sandstone and one siltstone stratum, we expected to detect amplitudinal and directional (expansion/contraction) differences in the deformations. These differences may be explained by the lithology, the structure, or the degree of alteration of the rock segment being monitored. Data from the crack meter time series could help better understand the differential weathering of the rock wall. The extensive weathering in the surface of the shale strata precluded installation of a crack meter.

1.5.2 Weather data

Various instruments were installed directly on the rock wall to evaluate the influence of climate-dependent variables on the deformations operating on the rock segment under study (Figure 5). A thermistor string and data logger from GeoPrecision operating at 915 MHz were installed perpendicular to the rock wall to measure the temperature (°C) every 30 cm up to 3 metres in depth (Figure 5.3). Surface temperatures were used to quantify thermal cycles, while temperatures deeper inside the rock mass were taken as indicators of freezing front and thawing front depths in winter. In addition, an Onset S-LIB-M003 Silicon Pyranometer (Figure 5.4) mounted one metre from the rock wall surface was used to measure incident solar radiation (W/m^2). For representative readings of received and reflected radiation, it was oriented perpendicular to the slope. An Onset S-SMC-M005 sensor, initially designed to measure soil moisture (m^3/m^3), was partially buried in sediments and placed below a platy rock (Figure 5.5). Because this sensor must be fully embedded in the soil, the data measured indicate the rough condition of humidity locally at the rock wall surface but

not exactly its saturation degree. This set of instruments were connected to HOBO Micro Station data logger and the USB data downloading was done on-site every three months.

A Campbell TE525WS-L rain gauge was used to measure precipitation (mm). In winter, it was equipped with the CS705 adapter to measure the water equivalent of solid precipitation. The rain gauge was the only instrument not installed on the rock wall. It was located nearby (21 km west) in a similar environment on the shore of the Gulf of St. Lawrence and at the same elevation.

The set of weather instruments installed directly on the rockwall were connected to HOBO Micro Station data logger whereas a hobo U30 NRC data logger recorded data from the rain gauge. Like the crack meters, weather data readings were taken every 15 minutes and downloaded on-site every three months. Data was collected from 1 July 2018 to 15 October 2020, a total of 27.5 months (838 days).

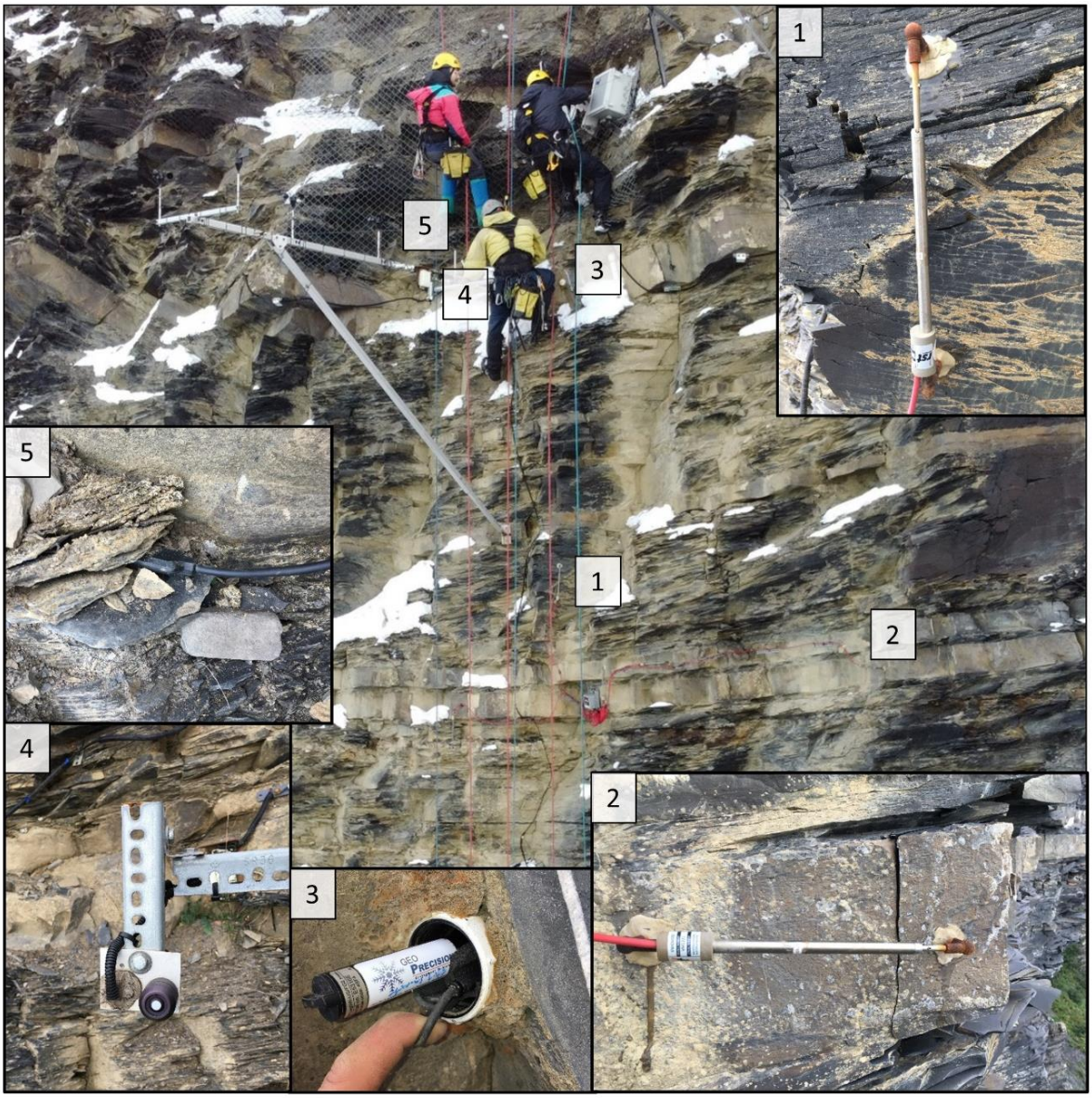

Figure 5. Instrumented rockwall including crack meters in siltstone (1) and in sandstone (2), thermistor string (3), pyranometer (4) and water content sensor (5).

1.5.3 Data analysis

To investigate the effect of meteorological variables on rock wall surface deformations, the most extensive deformations recorded by the crack meters were identified. The goal of

this approach is to analyze events that stand out from the trend or cycle of events driven by daily and seasonal air temperature variations (Draebing, 2021; Weber et al., 2016). Given the instrument's 0.1 mm accuracy, this study defined major movements as those with an amplitude over 0.15 mm that develop at a rate exceeding 0.1 mm/24 h. This threshold allowed a number of significant events to be analyzed while considering high-amplitude deformation outliers from the mean daily variability in the time series. Constraining by rate made it possible to retain only sudden movements lasting at most a few days that stand out from seasonal trends. This article uses the term "major deformation" for these significant (>0.15 mm) and sudden (0.1 mm/24 h) movements.

Major deformations identified in the two crack meter time series were filtered by a reversibility threshold. The reversibility of rock deformations is an important factor to consider. When movements are reversible, their amplitude remains below the elastic limit of the material (Gischig et al., 2011a). In contrast, the development of irreversible movements is an indicator of a progressive increase in the alteration degree of rock (Weber et al., 2017). In irreversible deformations, the elastic limit of a discontinuity in the rock under study is reached. This irreversibility generally takes the form of a rock bridge rupture, an increase in fracture opening and/or persistence, or movement along an existing discontinuity (Draebing and Krautblatter, 2019; Eberhardt et al., 2004; Gischig et al., 2011a). An accumulation of irreversible deformations affecting part of a rock wall can eventually lead to rockfalls (Eppes and Keanini, 2017; Erismann and Abele, 2001). Depending on the degree of rock alteration, the application of the same constraint could lead to either a reversible or an irreversible deformation (Weber et al., 2017).

On a daily scale, reversible deformations can appear irreversible. Conversely, irreversible deformations may seem reversible. Over time, many highly localized deformations could occur in the crack meter-monitored rock. Thus, the crack meter movement readings represent the resultant of all micro-movements in the instrumented rock since the previous reading. These localized micro-movements can result in contractions or expansions. Over the long term, irreversible deformations can appear reversible if other

opposite deformations—irrespective of amplitude—occur. However, all such events—irrespective of direction—can be spatially independent yet contribute to reduce resistance in the rock and hence to its alteration. This study compares the five-day average preceding a major deformation with the five-day average following the event. If the difference between these two averages was equal or greater than 50% of an event's total amplitude, that movement was considered to be irreversible. Otherwise, it was considered reversible (Figure 6). Using a 10-day period to evaluate the reversibility of a deformation is short enough to avoid overlap between independent irreversible deformations, and sufficiently long to observe if a deformation is really irreversible or if it will recover in a few days. Furthermore, the climate-dependent variables considered in this study occur over time scales of less than ten days and do not individually interfere over longer periods. Thus, this study defines an irreversible deformation as a deformation with an irreversible component that is equal to or greater than its reversible component over a 10-day period.

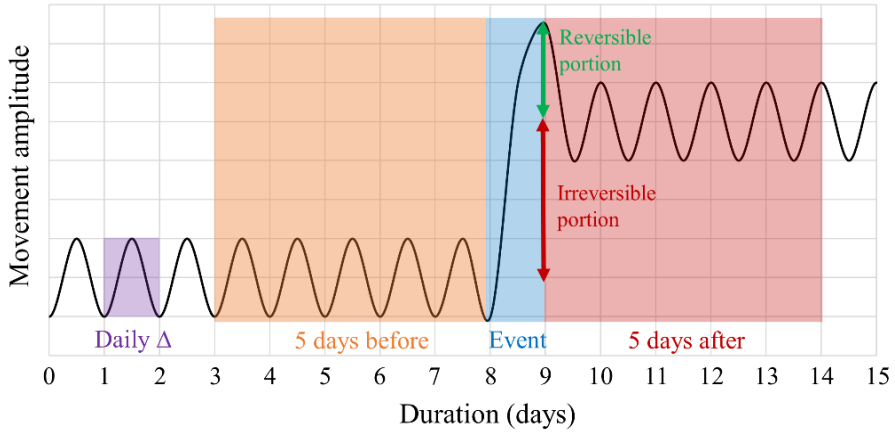

Mostly irreversible (10 days)

$$\frac{[\text{Mean 5 days before the event}] - [\text{Mean 5 days after the event}]}{\text{Event amplitude}} \times 100 \geq 50\%$$

Figure 6. Method used to define irreversible deformations applied on a theoretical movement time series.

Once identified, the measured major deformations were cross-referenced with the locally recorded meteorological variables. By instrumenting segment of altered but not

excessively precarious rock (Figure 5.1 and 2.2), we presumed that certain climate-dependent variables cause more major deformations than others, and that some of those variables more effectively create deformations with a high irreversibility component. Principle component analysis (PCA) was used to statistically analyze the influence of the meteorological variables on the rock deformations. Using the raw climate-dependent variable time series, the following explanatory variables were selected for the PCA: maximum amplitude of surface temperature during event (ΔT), maximum solar radiation recorded during event (SR), presence or absence of surface temperature fluctuations around 0°C during event (FT), maximum water content at slope surface during event (WC) and total rainfall during event (RF).

Of the five variables used for the PCA (ΔT, SR, FT, RF and WC), some can be redundant (autocorrelation). For example, the rock surface temperature (ΔT) can be linked to solar radiation intensity (SR). These two variables were nonetheless used in the PCA for a number of reasons. The variable ΔT can bring out significant but progressive temperature changes, while SR is more useful for highlighting abrupt changes in rock surface temperature due to slope exposure to direct solar radiation. Furthermore, extreme temperature variations can occur between October and March even if the northwest-facing rock wall is constantly in shade. The variables RF and WC can also be seen to be redundant. A rain event will generally result in an increase in water on the rock wall surface. However, precipitation is not recorded directly on the rock wall, and its ability to alter water content at the slope surface is dependent on wind direction and velocity (Sass, 2005b). Furthermore, variables other than rain have a strong influence on water content at the rock wall surface. During winter and spring thaws, melting ice from cracks in the rocks and melting snow from the plateau above the rock wall represent significant water inputs that are detectable by the variable WC (Coutard and Francou, 1989; Sass, 2005a). Despite their apparent (or event-driven) autocorrelations, we deemed it appropriate to retain all of the variables for the analysis.

1.6 RESULTS

Over the study period, the sandstone sequence had a general opening trend while the siltstone sequence had a general closing trend (Figure 7). The Solar radiation reached its maximum values in June and its minimum values in December and the surface temperature fluctuated between 30°C in summer and -22°C in winter. Rainfall events occurred mainly between April and the first half of November and the water content at the rock wall surface is remained low in winter and it responded to snow melt and rainfall in spring and summer (Figure 7).

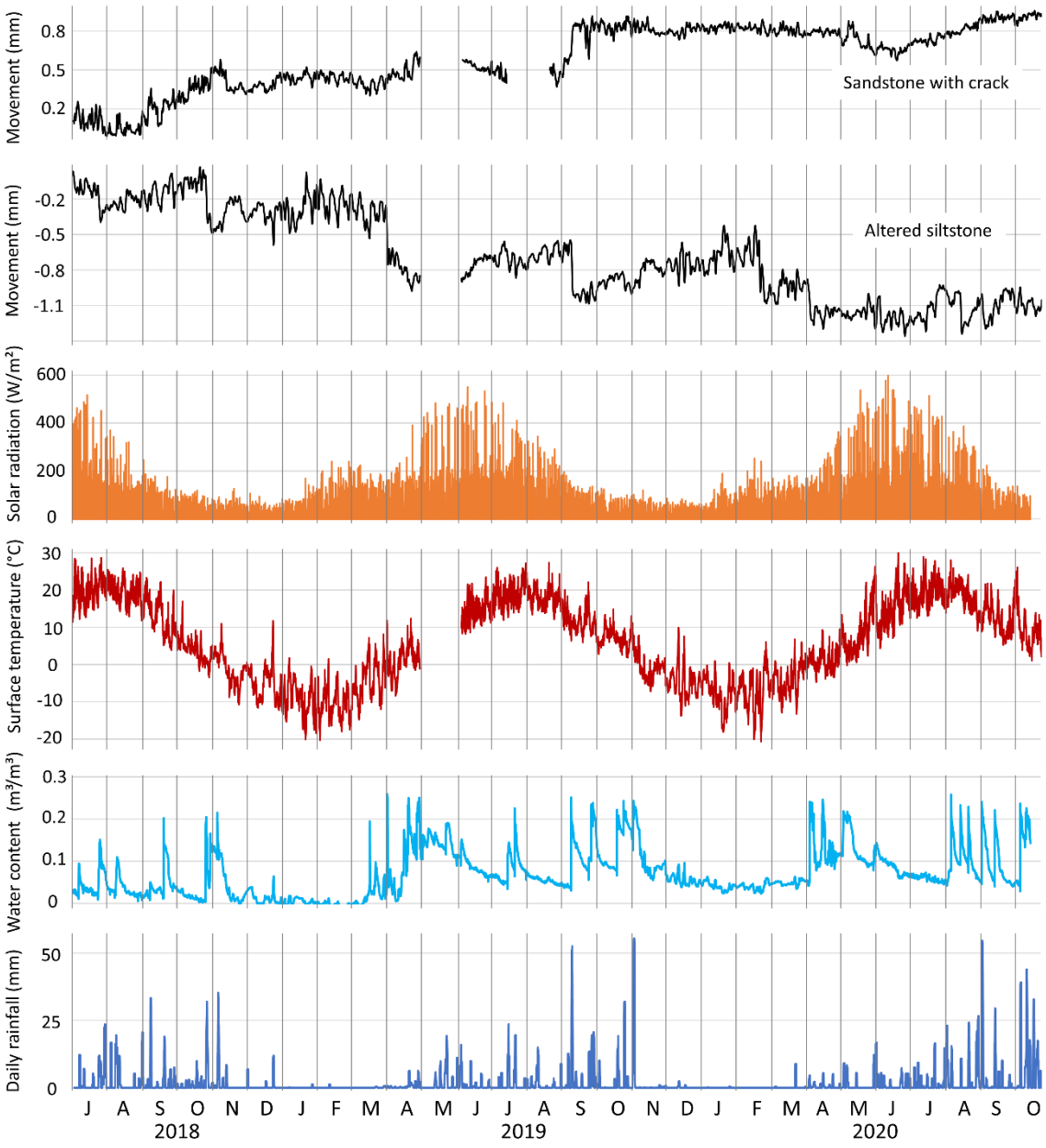

Figure 7. Overview of the data set recorded on the instrumented rock wall and used in this study.

1.6.1 Rock deformation measurements

Over the study period, the crack meter monitoring the siltstone sequence recorded 50 major deformations. Of that number, 16 were identified as irreversible (Figure 8). Most of the irreversible deformations were contractions (11 of 16). Over the same period, the crack meter monitoring the sandstone recorded 17 major deformations, 7 of which were identified as irreversible. Of the 7 irreversible deformations, 6 were expansions.

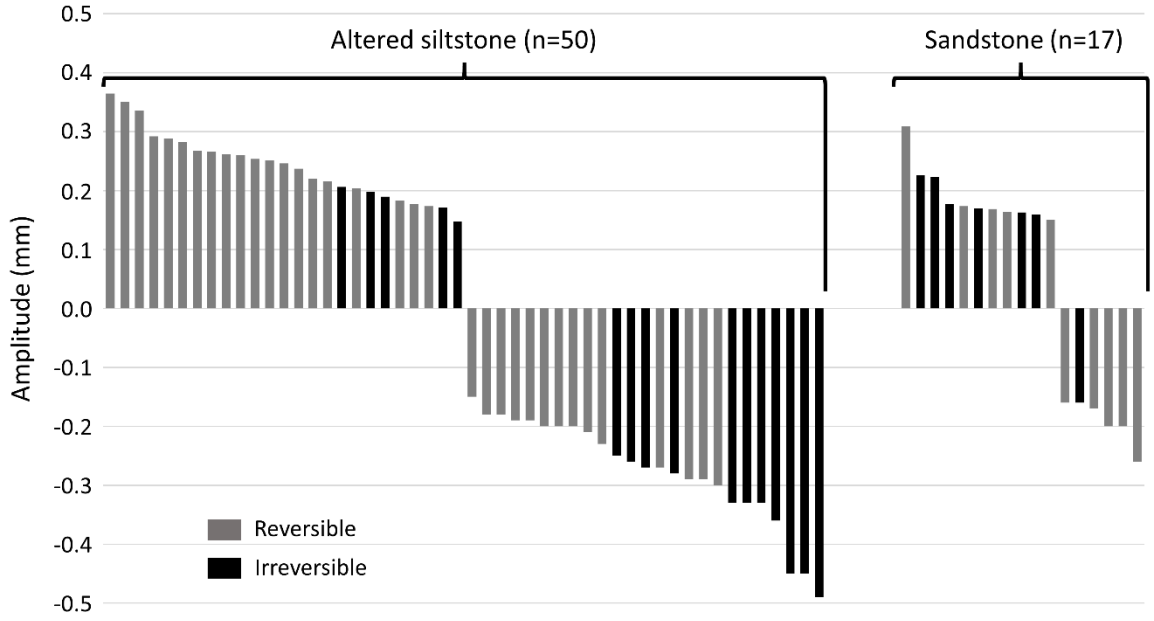

Figure 8. Set of major deformations measured between July 2018 and October 2020.

The time series is punctuated by daily fluctuations, but some irreversible contractions are responsible for this closing trend (-1.2 mm / 838 days). Between those episodes of irreversible deformations, a general opening trend is observed (Figure 9a).The six major irreversible deformations with the highest amplitude are detailed in Figure 9b. On 24 October 2018, a heavy rain event (39 mm) led to a sudden increase in water content at the rock surface (Figure 9b.1). The surface temperature during that event was slightly above 0°C. The crack

meter recorded a 0.4 mm closure in 48 hours, which represents 30% of the total amplitude of the 838-day time series. Over a 10-day period, this deformation is completely irreversible (100%). The settlement recorded in the siltstone sequence took nearly three months to recover.

On 31 March 2019, the temperature of the rock surface rose above the freezing point around 8:00 a.m. and climbed to 11°C by 4:30 p.m. (Figure 9b.2). This spring thaw penetrated to a depth of 39 cm and resulted in a sustained increase in water content at the rock wall surface, which sporadically reached its highest value in the time series (0.26 m^3/m^3). The temperature of the rock fell below 0°C the following morning and water content dropped again. In the siltstone segment, this thaw was accompanied by a contraction of 0.49 mm in less than 36 hours. The amplitude of this contraction represents 36% of the total amplitude of the time series. Over a period of 10 days, the irreversible component of the deformation was 78%. The total measured settlement was never fully recovered.

On 7 September 2019, Category 5 hurricane Dorian reached the Gulf of St. Lawrence as a post-tropical storm. It dropped 54 mm of heavy rain (4 mm/h for 12h 45 min) on the study site (Figure 9b.3). The water content at the rock wall surface recorded its third-highest level of the time series. This event coincided with a contraction in the siltstone segment of about 0.45 mm, which represents 33% of the total amplitude of the time series. This deformation had a 10-day irreversible component of around 84%. This settlement would have repercussions on the general trend for more than three months.

Between 15 February 2020 and 22 February 2020, very wide temperature fluctuations were measured at the rock surface. On the first day, the temperature fell sharply by 19.7°C (-0.8°C to -20.5°C). After recovering on the second day, it dropped again by 19.3°C (-1.8°C to -21.1°C) on the third day. On the four subsequent days, the temperature gradually rose from -21.1°C to +5.7°C. This thaw event reached 9 cm depth from rock surface (Figure 9b.4). The rate of temperature change during this episode did not exceed 3.8°C/15 min and appears to have remained below the thermal cracking threshold (Hall and André, 2001), even if this rate may have rapidly risen withing a few minutes. No rainfall events were recorded and

water content values remained relatively low. During this period, the crack meter recorded a major contraction in the siltstone sequence that occurred in three successive sudden movements. The first two resulted in a deformation characterized by a contraction with an amplitude of 0.55 mm over four days and a 10-day irreversibility of 62%. The amplitude of this contraction represents 41% of the total amplitude of the time series. The total measured subsidence was never fully recovered.

On 31 March 2020, a significant warming event thawed the rock wall to a depth of 50 cm for a period of several days (Figure 9b.5). The spring thaw was accompanied by a marked increase in water content at the rock surface from 0.05 m^3/m^3 to 0.24 m^3/m^3 in one hour. This episode coincided with a 0.33 mm contraction of the siltstone sequence with a 10-day irreversibility of 82%.

On 2020-08-11, a moderate but short rainfall event (11 mm) was accompanied by a sharp increase in water content at the rock surface, which rose from 0.09 m^3/m^3 to 0.23 m^3/m^3 in 30 minutes (Figure 9b.6). This rainfall event coincided with a 0.33 mm contraction of the siltstone sequence with a 10-day irreversibility of 85%.

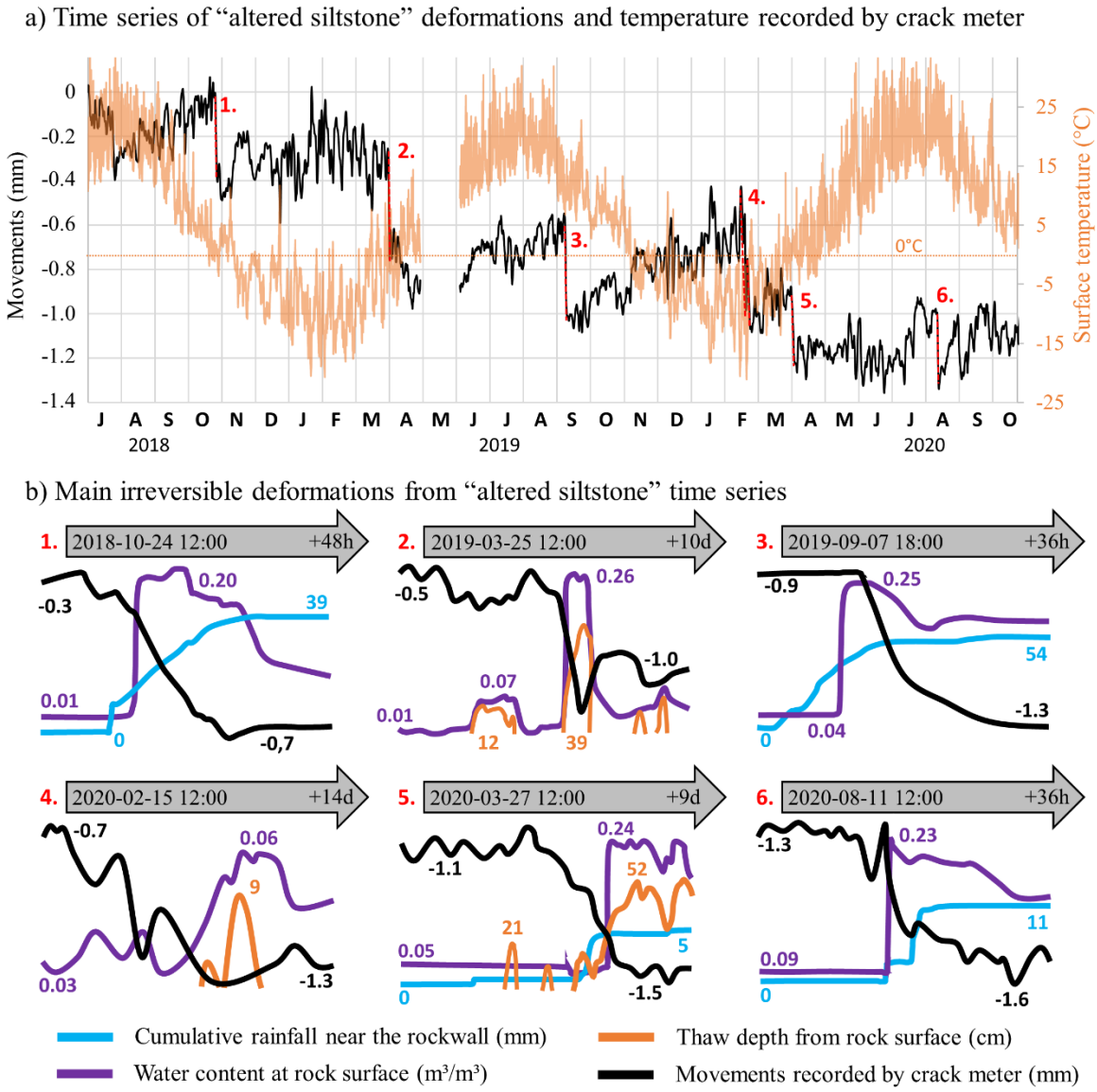

Figure 9. Time series of altered siltstone deformations (a) and main irreversible changes (b) recorded by crack meter between July 2018 and October 2020. The date and the number of hours/days displayed in the arrows are respectively for the beginning of the time series and for their duration from this date.

Over the 838-day study period, the movement time series recorded by the sandstone sequence crack meter had a general opening trend (Figure 10a). While punctuated by daily fluctuations, overall it trends toward expansion (+0.9 mm / 838 days). Despite being in the

opposite direction, the amplitude of this trend is comparable to that of the siltstone sequence. Despite a progressive expansion trend in summer, fewer major deformations were identified during the last year of the time series.

The three main irreversible major deformations in the time series are shown in Figure 10b. On 11 November 2018, a five-hour rainfall event of 8 mm was immediately followed by a fall freeze-thaw cycle. This coincided with a 0.16 mm contraction of the sandstone sequence with a 10-day irreversibility of 93% (Figure 10b.1). On 22 April 2019, an event typical of the spring took place as the rock wall thawed. Readings from the thermistor perpendicular to the rock surface (Figure 5.3) showed that depending on winter severity, the freezing front penetrated between three and five metres into the rock wall. In spring, the thawing process started at the surface and gradually penetrated the rock. During this progressive thaw, sudden melting from within the rock fall was observed. This thawing spike was characterized by the temperature at each thermistor rising above the freezing point in under 15 minutes. The temperature of the rock wall quickly returned to equilibrium and the freezing front reformed deep within the rock (Figure 10b.2). This known phenomenon, while poorly documented in rock walls, is an example of advection associated with a rising water table during the snow melt (Hoek and Bray, 1981; Terzaghi, 1962). While detectable because it occurred at right angles to the thermistor sensors, this flow cannot be generalized to the entire rock wall due to the preferential flow of water (Singhal and Gupta, 2010). This sudden influx of water and its associated thaw coincided with a 0.2 mm expansion of the instrumented sandstone sequence with a 10-day irreversibility of 86%.

The significant rainfall (54 mm) from tropical storm Dorian on 6 and 7 September 2019 affected both the siltstone and sandstone sequences (Figure 10b.3). Over the 838-day time series, this is the most significant event that affected the sandstone sequence. This 0.24 mm expansion with a 10-day irreversibility of 100% is a major contributor to the general expansion trend in the time series.

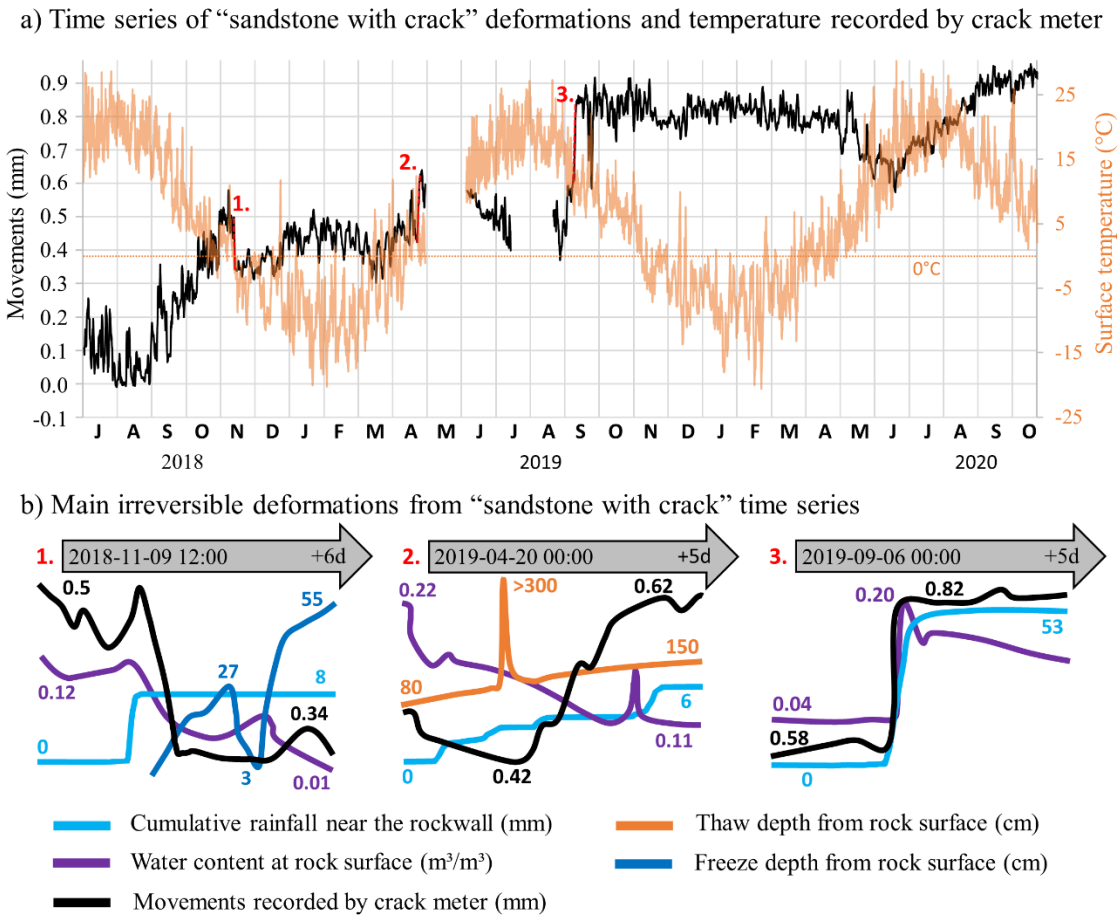

Figure 10. Time series of "sandstone with crack" deformations (a) and main irreversible changes (b) recorded by crack meter between July 2018 and October 2020. The date and the number of days displayed in the arrows are respectively for the beginning of the time series and for their duration from this date.

1.6.2 Statistical analysis

Figure 11a shows the PCA correlation circle with the distribution of explanatory climate-dependent variables for the 50 major crack meter-recorded deformations in the siltstone sequence. Dimension 1 on the X-axis and Dimension 2 on the Y-axis accounted for 38.4% and 25.1% of the total variance, respectively. The variables RF and WC were highly correlated, while SR was inversely correlated with FT.

Figure 11b presents the spatial distribution of the 50 major deformations of the siltstone segment based on the explanatory variables. The black dots represent irreversible movements, and the grey dots represent reversible movements. The dots representing the major deformations are ringed by coloured circles when the value of an explanatory variable is included in the highest 10% of the 838-day time series. Thresholds are WC > 0.175 m^3/m^3 (blue circle), RF > 5.3 mm (blue circle), SR > 365.6 W/m^2 (yellow circle) and $\Delta T > 12.5°C$ (red circle). Freeze-thaw cycles occurrence (orange circle) only coincided with 4.7% of the 838-day time series. Dotted lines around groups of events are used to improve graph readability; they are not statistically derived.

Of the 50 major deformations identified in the siltstone sequence, 20 correlated with a freeze-thaw cycle, 14 with a rainfall event, 13 with high water content at the rock wall surface, 12 with a high surface temperature amplitude and three with strong solar radiation. Some deformations correlated with many of the above conditions. For example, on three occasions, a winter freeze-thaw event was accompanied by rainfall and by a significant surface temperature variation. While the 15 remaining deformations—including two of the 16 irreversible movements—had values under the 10% threshold for explanatory variables, they nonetheless coincided with low amplitude variations in temperature, solar radiation and water content.

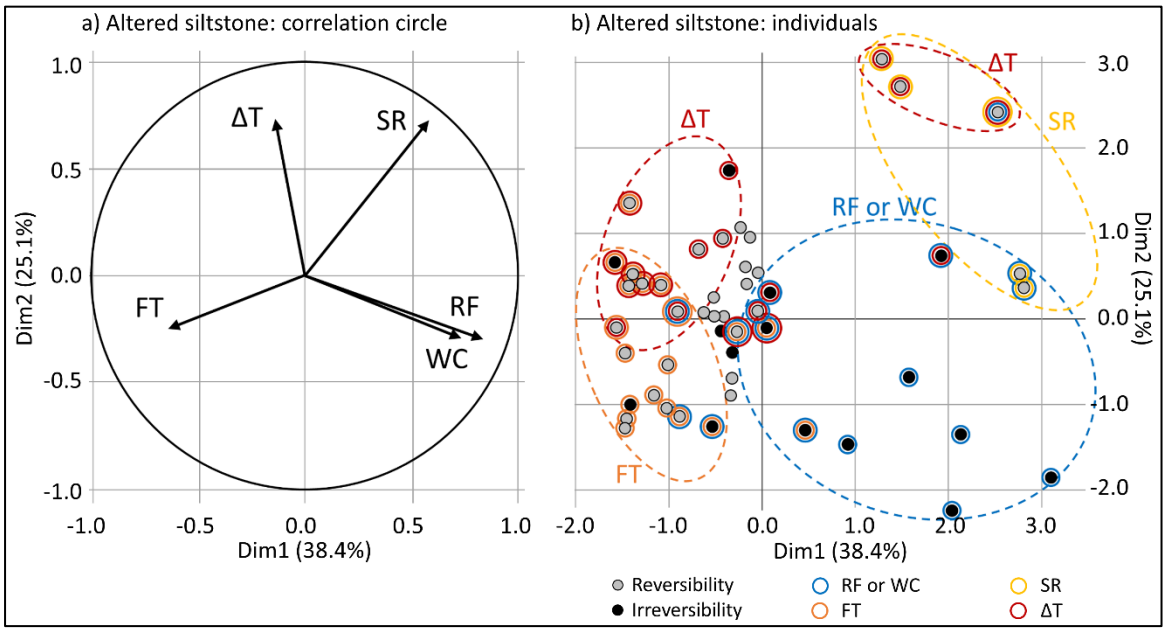

Figure 11. Principal component analysis to highlight which variable contributes more to irreversible movements – Altered siltstone: correlation circle (a) and individuals (b).

Figure 12a shows the PCA correlation circle obtained with the distribution of explanatory meteorological variables for the 17 major deformations that affected the studied segment of sandstone. Dimension 1 on the X-axis and Dimension 2 on the Y-axis accounted for 43.5% and 30.6% of the total variance, respectively. For this crack meter, the PCA used four explanatory variables: RF, WC, FT, and SR. The variable ΔT is not used since none of the 17 major deformations occurred during an extended amplitude variation in rock surface temperature (threshold > 12.5°C). RF and WC had a weaker correlation than for the siltstone segment. WC was also inversely correlated with SR.

Figure 12b presents the spatial distribution of the 17 major deformations identified in the sandstone segment based on the explanatory variables. Six of these major deformations coincided with rainfall events. The two highest intensity rainfall events (>20 mm) produced irreversible movements. Two additional non-rainfall events presented high water content at the rock wall surface. Three major deformations in the instrumented sandstone sequence correspond to freeze-thaw cycles. All three are irreversible. Three major deformations

coincide with high intensity solar radiation, and one is irreversible. The latter also corresponds to a freeze-thaw cycle and a high water content event. Seven major deformations were below the 10% threshold for explanatory variables, but they nonetheless coincided with low amplitude variations in temperature, solar radiation, and water content. These included two of the seven irreversible movements.

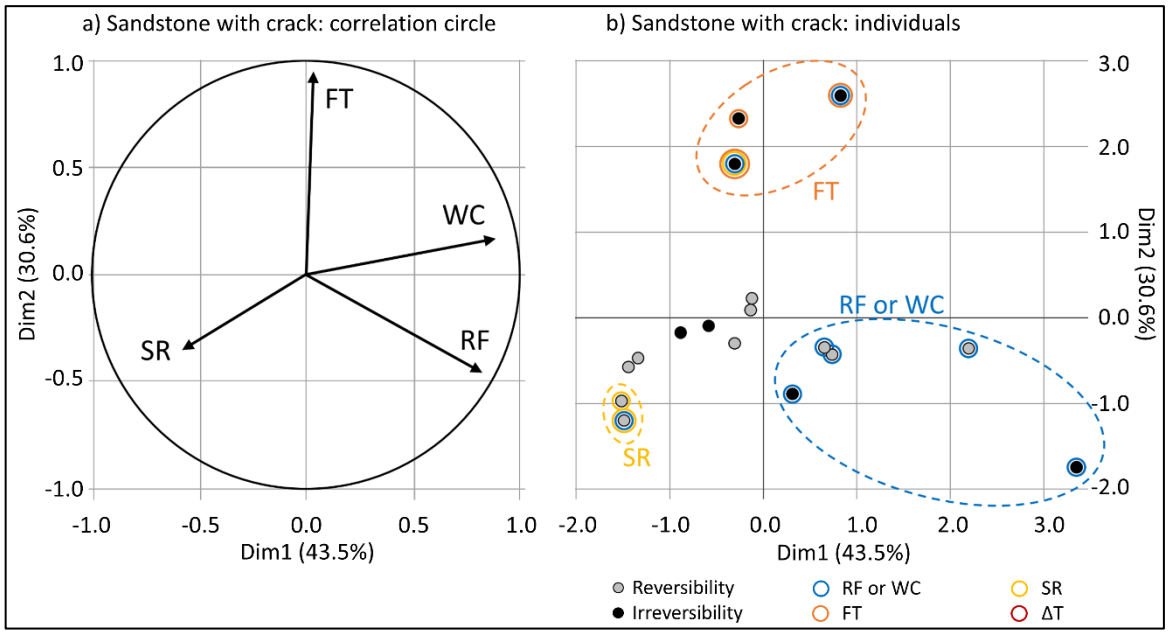

Figure 12. Principal component analysis to highlight which variable contributes more to irreversible movements – Sandstone with crack: correlation circle (a) and individuals (b).

1.7 DISCUSSION

1.7.1 Influence of climate-dependent variables on deformation and alteration of sedimentary rock

FT is the variable with the strongest correlation with major deformations in the instrumented siltstone segment (Figure 11b). Indeed, while freeze-thaw cycles only coincided with 4.7% of the time series, they corresponded to 40% of all identified major

deformations. However, the results show that most deformations corresponding to freeze-thaw cycles were reversible. Furthermore, of the five that are irreversible, four corresponded to another explanatory meteorological variable, of which three corresponded to WC. A similar dynamic can be observed with the instrumented sandstone. FT coincided with three major deformations, all irreversible. At least two of those presented high water content at the rock surface. These results highlight the role of water in the effectiveness of freeze-thaw cycles discussed by many authors (e.g., Hall, 2004; Matsuoka, 2001, 2008). Rock must have at least 90% pore saturation for the 9% expansion associated with the liquid-solid phase change to contribute to its alteration (Bost, 2008; Davidson and Nye, 1985; Hallet et al., 1991; Rode et al., 2016; Walder and Hallet, 1985). Hall et al. (2002) note that the ability of freeze-thaw cycles to alter rock is often overestimated, while the importance of available water is often underestimated. Rode et al. (2016) show that, in two study sites in the Alps, the thresholds for frost cracking by volumetric expansion (temperature and pore saturation) are reached less than during 0.5% of the time during a year. This is supported by the results of this study, since most of the freeze-thaw cycles accompanied by a low availability of water resulted in reversible deformations. Conversely, they caused irreversible deformations when water content was high (Figure 11 and Figure 12). Spring freeze-thaw cycles are often associated with high water content at the surface of the rock wall (Figure 9b), which makes them particularly effective (Matsuoka, 2001). High water availability in spring is mainly attributable to meltwater from ice in cracks and surface snow (Coutard and Francou, 1989; Sass, 2005a). Liquid water infiltration can also accelerate spring thaws by transferring heat energy to the rock (Weber et al., 2017, Figure 10b.2).Irrespective of whether it is from melting snow or ice, or from rainfall events, water infiltration can lead to increased hydrostatic pressure. This can reduce shear strength by changing cohesion and friction along discontinuities (Blikra and Christiansen, 2014; Fischer et al., 2010; Krautblatter et al., 2013). Seeping water may also erode and wash away fine particles, especially in highly fractured rock (Duszyński et al , 2016; Hall et al., 2002; Higgins and Osterkamp, 1990). This study shows that many rainfall events resulted in major deformations that were often irreversible (Figure 11 and Figure 12). Thus, water content variations appear to contribute to the

alteration of sedimentary rock, particularly siltstone, which has a high clay content and which is highly fractured. Overall, the variables that lead to high water content at the rock surface (rainfall, snowmelt) produce the majority of the major deformations, more than half of which are irreversible. This result highlights the central role water plays in the alteration of these rocks. However, crack meter measurements do not allow to assess the relative responsibility of wetting-drying cycles, hydrostatic pressure variations and wash away of fine particles.

Rock surface temperature is also influenced by variations in air temperature and incident solar radiation intensity (Hall, 1997; Hall, 2004). The crack meter measurements show that variations in rock surface temperature consistently result in expansion and contraction movements in sandstone and siltstone. Draebing (2021) observed that the rock he instrumented contracted as its temperature decreased and expanded as its temperature increased. In a highly stratified sequence of sedimentary rock such as the siltstone segment under study, we observed the inverse relationship. When a rock segment is embedded in a rock mass, its response to thermal variations is influenced by the elastic behaviour of adjacent rocks (Figure 13). This rock segment may be subjected to "forced" contraction even as its temperature is rising if the surrounding rocks are better able to expand. In the instrumented siltstone stratum, the many fractures and fissures probably tend to close under the pressure of expanding adjacent rocks. Consequently, increased temperature produces a contraction at the crack meter monitoring the siltstone sequence. Of the 24 major deformations that coincided with the variables ΔT and SR in the two instrumented sequences, most also coincided with other explanatory variables (Figure 11 Figure 12). Only the irreversible deformation that occurs on the 15th of February 2020 (Figure 9b.4) should be attributable to thermal cycles.

The measurements show that deformations of the same amplitude have a large irreversible component when they are associated with freeze-thaw cycles or a significant increase in water content when they are associated with thermal cycles (Figure 11 andFigure 12). When movement is thermally induced, the recorded expansion is uniformly distributed along the entire length that separates the two crack meter anchors. The presence of open

fractures in the instrumented segment can attenuate the amplitude of recorded movements since they will contract and thereby partially compensate for an expansion (Figure 13.1). This phenomenon was also described by Draebing (2021). Moisture, like freezing, can also trigger rock pore expansion, but Sass (2005a) showed that fluctuations in water saturation are less pronounced in the very first centimetres of rock and are practically nonexistent by around 10 cm of depth. However, water content fluctuations in a discontinuity can cause variations in the hydrostatic pressure applied to its edges and cause the discontinuity to open (Blikra and Christiansen, 2014; Fischer et al., 2010; Krautblatter et al., 2013). Thus, a crack meter recorded expansion due to thermal expansion will be distributed along the entire instrumented segment, while a recorded expansion of identical amplitude caused by increased water availability can be concentrated at a discontinuity (Figure 13). A 0.2-mm movement distributed evenly along the 33 cm between a crack meter's anchor points represents a deformation of 0.0006 cm/cm. If the recorded movement is actually concentrated in a ~3 mm wide fracture, it represents a deformation of 0.07 cm/cm. In this specific example, with recorded movements of the same amplitude, the deformation is 117 times greater locally when concentrated in a fracture than when it is distributed. In addition to being more localized and concentrated, a deformation that occurs in a fracture will result in movement along the length of that fracture. Two movements of the same crack meter measured amplitude can therefore have very different meanings. This hypothesis would explain why the variables FT, WC and RF lead to deformations with a higher irreversibility component than the variables ΔT and SR.

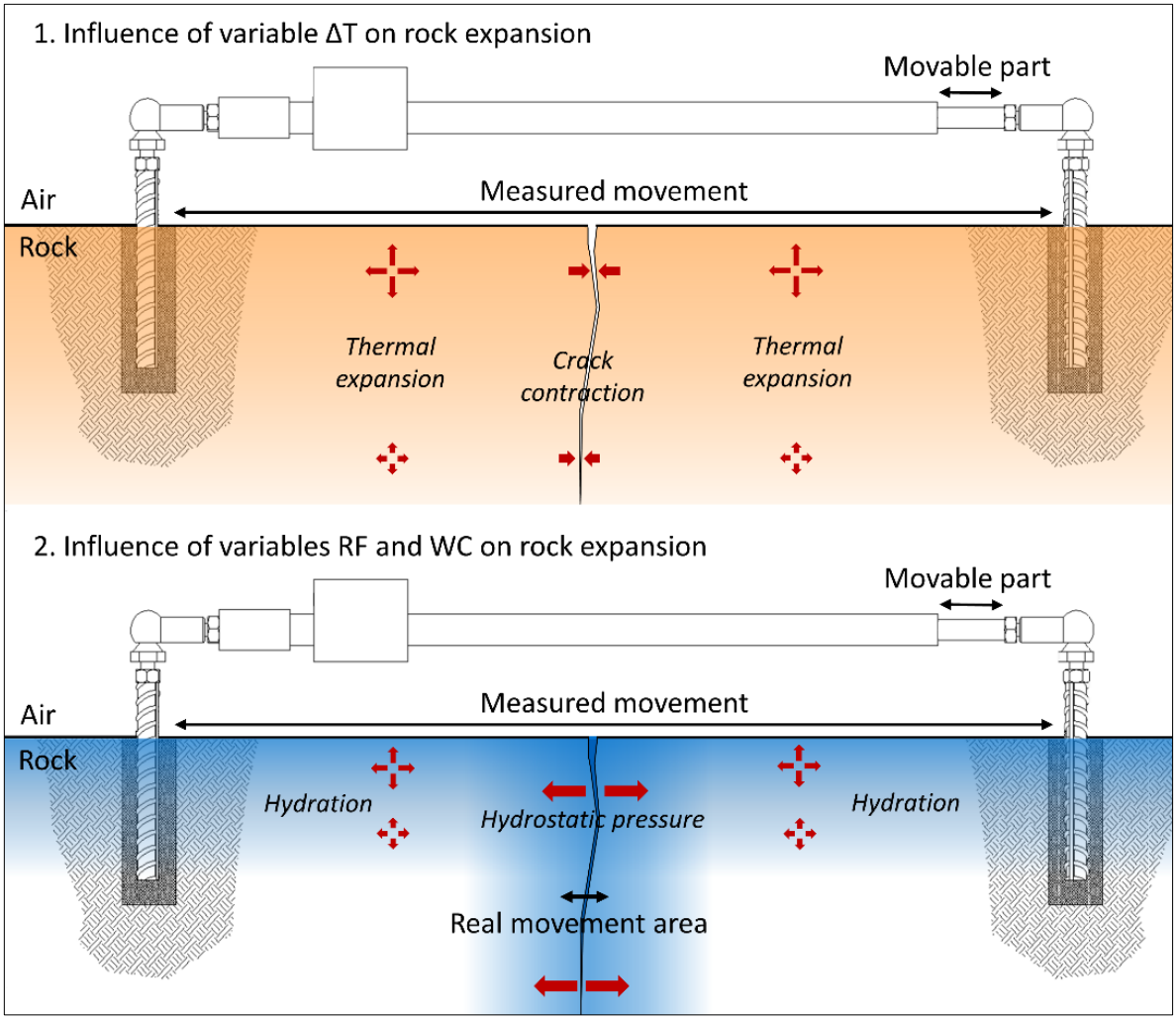

Figure 13. Influence of ΔT (1), WC and RF (2) on rock expansion in a segment of sandstone with a crack. Schematic crack meter draw taken from ©RST.

This study also highlights the compounding effect when weathering processes are combined (Anderson, 2005). Since the occurrence of variables can overlap, their combination likely explains a given deformation. For example, the presence of water in discontinuities and rock cracks is a prerequisite for freeze-thaw cycle deformations (Hall et al., 2002; Rode et al., 2016). In the instrumented siltstone, deformations associated with freeze-thaw cycles were irreversible in 14% of cases when the measured water content was low and in 50% of cases when significant water was available (Figure 11b). When combined with high water

content, the measured effectiveness of freeze-thaw cycles is multiplied by a factor of 3.6. Similarly, a winter freeze-thaw (FT) can be accompanied by rainfall (RF) and a summer rainfall by a sudden and significant change in temperature (ΔT).

Some major deformations in the instrumented rock segment did not coincide with high values of the explanatory variables (Figure 11 and Figure 12). These deformations can be explained by low amplitude variations in temperature and solar radiation and water content. While measured directly on the rock wall, the explanatory climate-dependent variables were not captured at the exact locations of the recorded deformations and biases may be present. For example, rock wall microtopography has a large impact on exposure to solar radiation (Hall, 2004), and the discontinuity network controls preferential water flow (Singhal and Gupta, 2010). Lastly, other meteorological and non-meteorological variables, as earthquakes (e.g. Becker and Davenport, 2003; Coe and Harp, 2007; Keefer, 1984; Marzorati et al., 2002), which are not considered by this study could potentially explain some of these deformations. The time series recorded by crack meter show that, in addition to major deformations, some long-term expansions can also be highlighted. Two progressive expansions of 0.4 and 0.5 mm in the siltstone sequence were respectively recorded from August to October 2018 and from September 2019 to February 2020 while only one 0.5 progressive expansion was recorded in the sandstone sequence from September and November 2018. Because these long-term expansions did not fit with season and were not consistent from one year to next, gravitational compaction for the siltstone sequence and gravitational tilting for the sandstone sequence could explain these tendencies. Longer time series and further research could help to improve our understanding of these long-term deformations.

1.7.2 Development of instabilities

Over the study period, the time series of crack meter-recorded movements in the siltstone sequence had a general trend toward contraction. This was driven by a few sudden contraction events (Figure 9a) that are likely explained by the loss of rock particles and fragments and by gravitational compaction of the sequence. Water from rainfall, snow or ice

melt is an efficient transport agent that can dislodge and wash away detached fine particles (Duszyński et al., 2016; Hall et al., 2002; Higgins and Osterkamp, 1990). Due to its horizontal stratification, the siltstone sequence is under compression and predisposed to settlement in a series of sudden events as material is lost. Between these sporadic irreversible events, a general opening trend can be observed. This trend appears to respond to daily air temperature variations and moderate freeze-thaw and wet-dry cycles (Figure 10a). We suggest that gradual heaving results from in-situ fragmentation of the stratified siltstone.

As the siltstone stratum subsided, the sandstone sequence crack meter recorded a general opening trend (Figure 10a). The time series shows daily fluctuations and a general trend to expansion. This trend points to the progressive opening of the vertical persistent discontinuity between the two crack meter anchors. Assuming the siltstone stratum under the sandstone layer follows the same trend as the instrumented siltstone, the progressive opening of the discontinuity in the sandstone layer likely results from the settlement of the underlying layer. The closing trend measured in the siltstone sequence by the vertical crack meter and the opening trend measured in the sandstone stratum by the horizontal crack meter support the rock instability mechanisms in flysch proposed by Cano and Tomas (2013) and Miščević and Vlastelica (2014). To illustrate this differential weathering, the relative positions of the crack meters used in this study are shown in the conceptual scheme in Figure 14. The first crack meter is oriented vertically, perpendicular to the siltstone bedding plane (Figure 14a). As the siltstone stratum erodes, it simultaneously retreats and settles. Its loss of fragments is reflected in a reduction in the distance between crack meter anchors. This progressive closure can be observed on the study site (Figure 9a) and is illustrated in Figure 14b and Figure 14c.

In the conceptual scheme, the second crack meter is anchored horizontally in a sandstone stratum, straddling a fracture. As in this study, one of the two anchors is shown set in a block of unstable sandstone detached from the rest of the sandstone stratum by a persistent vertical fracture (Figure 14a). The rapid erosion of the stratified siltstone leaves the overlying sandstone block to overhang. The gradual retreat and settlement of the weak siltstone layer causes the bloc to slide or topple down recorded as a progressive opening, as

shown in Figure 10a and illustrated in Figure 14b and Figure 14c of the conceptual scheme. A persistent vertical discontinuity in the sandstone stratum conditions the maximum length of the overhang and the size of the blocks that may fall. When the overhang reaches 50% of that length, the block will topple and fall unless a certain slope is present (Mohr-Coulomb failure criterion), in which case it will slide and fall. The erosion of the underlying clay stratum conditions the failure mode of the overlying sandstone stratum. Thus, sandstone blocks can topple, slide, or have a mixed failure mode, i.e., an initial slide followed by toppling (Figure 14d). This can be expected for flysch slopes and other sedimentary slopes with horizontal or sub-horizontal bedding that are sensitive to differential weathering.

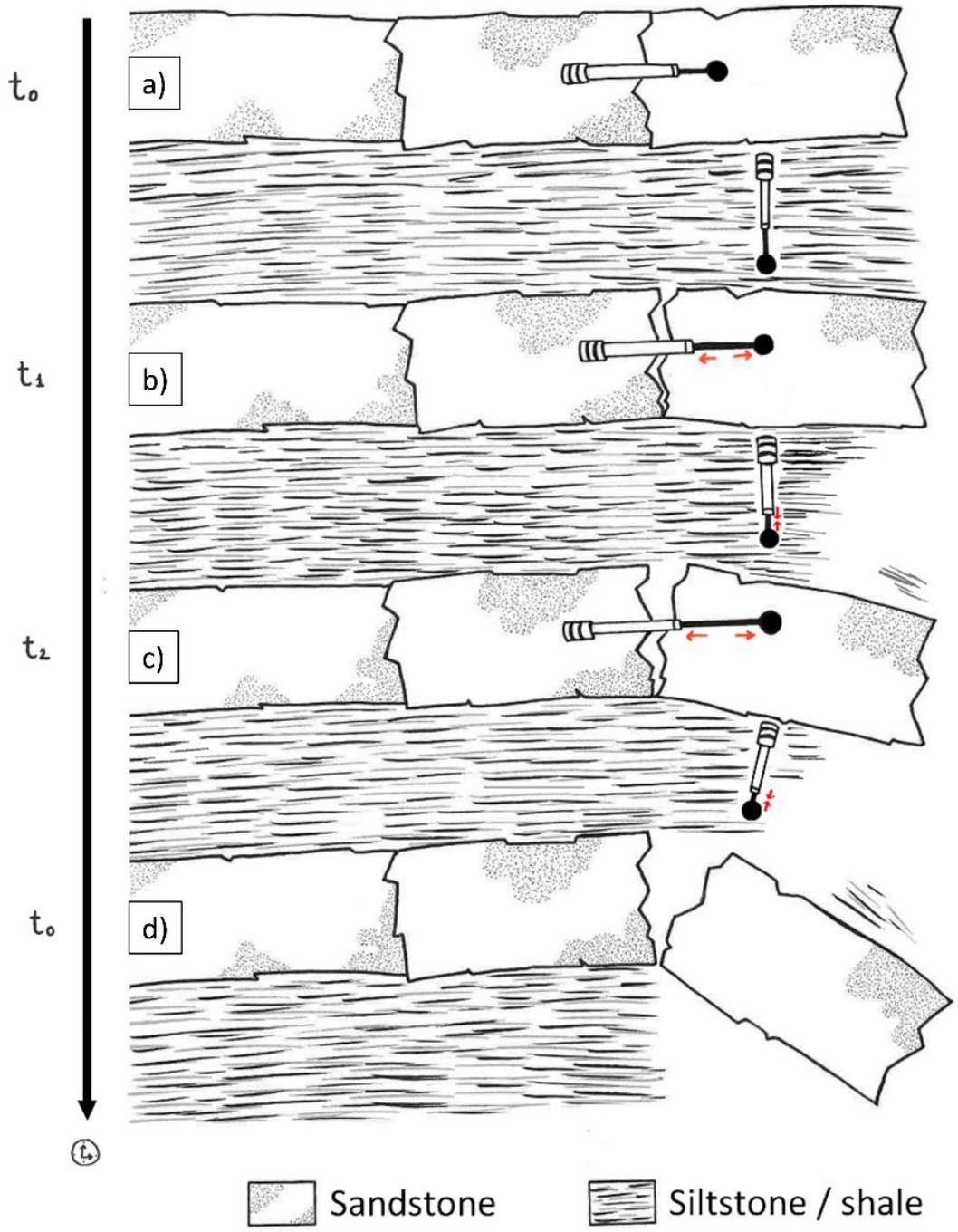

Figure 14. Conceptual scheme of the development of rock instabilities in the flysch sequences (drawn by Leïla Bennour).

1.8 CONCLUSION

This study implemented a protocol that made it possible to identify the major deformations affecting two distinct segments of rock on the surface of a flysch rock wall. One crack meter was used to record vertical movements in a siltstone stratum while a second recorded horizontal movements in a sandstone stratum. Primary component analysis was used to associate these deformations with the climate-dependent variables that cause mechanical weathering. It highlighted that:

1. The irreversible deformations affecting the siltstone segment were primarily contractions and are indicative of its subsidence;

2. The irreversible deformations in the sandstone segment were primarily expansions and are indicative of the opening of a persistent vertical fracture that tends to gradually push and destabilize the overhanging block;

3. The irreversible deformations in the siltstone segment were primarily caused by water content fluctuations (rainfall, snow and ice melt) at the rock surface. These fluctuations affect the impact of the shrink-swell process in clayey rocks and the hydrostatic pressure variations in rock mass discontinuities and should also erode and wash away detached fine particles;

4. The irreversible deformations in the sandstone segment were primarily caused by freeze-thaw cycles and water content fluctuations at the rock surface.

High intensity rainfall events, spring snow melt and temperature fluctuations around the freezing point are effective variables for predicting major deformations in the first decimetres of instrumented sedimentary rock. However, high amplitude thermal variations and freeze-thaw cycles are less effective at generating irreversible deformations in the siltstone than variations in water content at the rock surface. This study has made it possible for the first time to quantify the respective contributions of mechanical weathering processes and thereby compare their relative impacts and discuss the compounding effect when those

processes are combined. Having an overview of the processes makes it possible to limit overestimating or underestimating the individual impact of each process on rock alteration. The crack meter time series also highlight the challenges in distinguishing reversible from irreversible deformations in an environment where not all parameters are controlled. In some cases, it remains difficult to clearly discern the effect of weathering processes on major deformations (e.g., hydrostatic pressure vs. wetting and drying vs. wash away of detached fine particles).

The long-term trends in the sandstone and siltstone strata recorded by crack meters, along with field observations, highlight the differential weathering that leads to the development of the characteristic rock instabilities in these flysch rock walls. The clayey silt strata, which have a lower resistance to weathering and a larger number of fractures, erode more rapidly, leading to the formation of sandstone strata overhangs. The sliding or toppling failure mode of the sandstone blocks is subject to the erosion dynamics of the siltstone and shale strata, which tend to subside and recede more rapidly. The results of this study underscore the importance of studying rock wall dynamics as a whole to understand the mechanisms that lead to the development of hazardous large-scale rock instabilities.

1.9 ACKNOWLEDGMENTS

We thank the ministère des Transports du Québec (MTQ) as well the Natural Sciences and Engineering Research Council of Canada (NSERC) for funding this research. We acknowledge the LGGRM members who help us with the instrumentation process of the study sites, the maintenance, and data collection. We also would like to thank the anonymous referees of *Geomorphology* for valuable comments that improved the quality of the paper.

1.10 DATA AVAILABILITY

Datasets related to this article are available on request.

CHAPITRE 2

ÉVALUER LA RELATION ENTRE LES CONDITIONS MÉTÉOROLOGIQUES ET LES CHUTES DE PIERRES PAR L'UTILISATION DU TLS POUR SOUTENIR LA GESTION DU RISQUE NATUREL

2.1 RÉSUMÉ

Depuis 1987, plus de 13 200 chutes de pierres ont été répertoriées par le ministère des Transports du Québec (MTQ) sur la route nationale 132 en Haute-Gaspésie. Ces instabilités rocheuses représentent un danger quasi-permanent pour les usagers de la route et les mesures de gestion traditionnelles peuvent s'avérer inefficaces sur les parois rocheuses hautement altérées comme celles du nord de la Gaspésie. La mise en place d'une gestion préventive du risque, basée sur les facteurs qui déclenchent ces instabilités, pourrait être la méthode la plus efficace pour diminuer ce risque. Les tremblements de terre, les événements de pluie et les cycles gel-dégel sont communément considérés comme étant les principaux facteurs susceptibles de déclencher des chutes de pierres. Cette étude cherche à mieux comprendre l'influence des conditions météorologiques sur le déclenchement de ces instabilités afin d'apporter les connaissances nécessaires à la mise en place gestion préventive du risque naturel. La fréquence et la magnitude des chutes de pierres ont été quantifiées sur trois sites à l'aide d'un scanner laser terrestre (TLS) pendant 17 périodes météorologiques ciblées au préalable. Des instruments météorologiques et des thermistances jusque 550 cm de profondeur ont également été installées directement à la surface d'une paroi rocheuse. Les relevés ont permis d'identifier 1287 chutes de pierres d'une magnitude supérieure à 0,005 m^3 sur une surface scannée de 12 056 m^2 pendant une période de 18 mois. En été, la fréquence des chutes de pierres était 22 fois plus élevée lors d'un événement pluvieux intense que lors d'une période principalement sèche. En hiver, la fréquence des chutes de pierres était 12 fois

plus élevée lors d'un dégel superficiel (< 30 cm) que lors d'une période froide où la température reste inférieure à 0°C. Ces redoux hivernaux se traduisent par le développement d'instabilités rocheuses de faible magnitude alors que le dégel printanier en profondeur entraîne une fréquence élevée d'événements de grande magnitude. L'influence des conditions météorologiques sur la fréquence et la magnitude des chutes de pierres est cruciale dans une optique de gestion préventive du risque puisque les dommages causés par ces instabilités sont proportionnels à leurs magnitudes. Cette étude propose une classification des conditions météorologiques en fonction de leur capacité à déclencher des instabilités rocheuses de différentes magnitudes. Ces connaissances pourront être utilisées afin de mettre en place une gestion préventive du risque naturel.

Mots-clés : Gel-dégel, Pluie, Facteurs déclencheurs, Chutes de pierres, Gestion du risque; LiDAR, TLS.

Contribution des auteurs :

Cet article, intitulé « *Assessing the relationship between weather conditions and rockfall using terrestrial laser scanner to improve risk management* », a été soumis en mai 2022 à la revue *Natural Hazards Earth System Science.* Il a été révisé en juillet 2022 et soumis dans sa version finale en octobre 2022 (doi : https://doi.org/10.5194/egusphere-2022-326). En tant que premier auteur, j'ai contribué à l'essentiel de la recherche sur l'état de la question, au développement de la méthode, au traitement des données et à la rédaction de l'article. Le professeur Francis Gauthier, second auteur, a fourni l'idée originale et a aidé à la révision de l'article.

Une version abrégée de l'article a été présentée à la 8ème *conférence canadienne sur la géotechnique et les risques naturels* (Géorisques 8) à Québec (Canada) en juin 2022 : Birien, T., et Gauthier, F. 2022. Dynamique des parois de flysch (partie2) : conditions météorologiques propices aux chutes de pierres. *In* 8e conférence canadienne sur la

géotechnique et les risques naturels - Géorisques 8. *Edited by* Société canadienne de géotechnique. Québec. pp. 385-393.

2.2 ASSESSING THE RELATIONSHIP BETWEEN WEATHER CONDITIONS AND ROCKFALL USING TERRESTRIAL LASER SCANNER TO IMPROVE RISK MANAGEMENT

Tom Birien[a], Francis Gauthier[a]

[a] *Département de biologie, géographie, chimie, Centre for Northern Studies (CEN), Université du Québec à Rimouski, Rimouski, Québec, Canada*

Abstract: Since 1987, more than 13,200 rockfalls have been inventoried by the Québec Ministry of Transport (MTQ) as having impacted the National Road 132 in northern Gaspésie. This natural hazard represents a nearly permanent danger for users. Traditional mitigation measures can be ineffective on poorly consolidated, deformed and highly fractured rockwall such as those found in northern Gaspésie. To address this issue, implementing a preventive risk management based on the factors that trigger rock instabilities could be the most effective method. Earthquake, rainfall and freeze-thaw cycles are commonly considered to be the main rockfall triggering factors. This study aims to better understand the climatic conditions conducive to rockfalls in northern Gaspésie in order to provide knowledge to implement an appropriate risk management strategy. Three rockwalls were scanned with a terrestrial laser scanner (TLS) during specific pre-targeted weather conditions. Over a period of 18 months, 17 surveys have allowed to identify 1,287 rockfalls with a magnitude above 0.005 m^3 on a scanned surface of 12,056 m^2. In addition, meteorological instruments and a 550 cm thermistor string have been installed directly on a vertical rockwall. It appears that some weather conditions influence occurrence, frequency, and magnitude of rockfalls. In winter, rockfall frequency is 12 times higher during a superficial thaw than during a cold period in which temperature remains below 0°C. In summer, rockfall frequency is 22 times higher during a heavy rainfall event than during a

period mainly dry. Superficial freeze-thaw cycle (< 50 cm) causes mostly a high frequency of small magnitude events while deeper spring thaw (> 100 cm) results in a high frequency of large magnitude events. Influence of weather conditions on rockfall frequency and magnitude is crucial in order to improve risk management since large magnitude events represent higher potential hazards. This study provides a classification of weather conditions based on their ability to trigger rockfalls of different magnitudes. This knowledge could be used to implement a risk management strategy.

Keywords: Freeze-thaw, Rainfall, Triggering factor, Rockfall, Risk management, LiDAR, TLS.

2.3 INTRODUCTION

Rockfall is hillslope movement in which blocks detach from the surface of rocky escarpments (Budetta, 2004; Michoud et al., 2012; Piteau and Peckover, 1978; Selby, 1993). Rock mass properties, such as lithology, degree of alteration, discontinuity network characteristics and slope, are predisposing factors in the occurrence, magnitude and failure mode (e.g. planar, wedge or toppling) of rock instabilities (e.g. Selby, 1993; Turner and Schustler, 1996). Although they are spontaneous, rockfalls result from the long term interaction of a series of processes (Birien and Gauthier, 2022; Schovanec, 2020). They never result solely from the latest visible change (Draebing and Krautblatter, 2019; Gunzburger et al., 2005). Many factors can contribute to the development of rock instabilities, but two are recurring in the literature: precipitation and freeze-thaw cycles (e.g. Collins and Stock, 2016; Coutard and Francou, 1989; D'Amato et al., 2016; Hungr et al., 1999; Matsuoka and Sakai, 1999; Rapp, 1960; Wieczorek and Jäger, 1996).

While there is consensus in the literature on the influence of meteorological variables on rockfall, quantifying their respective roles is often difficult because they are challenging to differentiate (Schovanec, 2020). Studies of rockwall dynamics have long been complicated by the poor accessibility and dangerous nature of the terrain (Abellán et al., 2014). The recent

development of remote sensing techniques, particularly LiDAR (Light Detection and Ranging), has considerably improved our ability to study rockwall dynamics (Abellán et al., 2014; Guerin et al., 2014; van Veen et al., 2017). Terrestrial laser scanning (TLS) makes it possible to carry out topographical surveys of vast areas with good accuracy and very high resolution (Abellán et al., 2014; Santana et al., 2012; Williams et al., 2018). By comparing the point clouds from several surveys, rock instabilities that occurred between the surveys (e.g. van Veen et al., 2017) and developing future instabilities (e.g. Kromer et al., 2018; Oppikofer et al., 2008, 2009; Royán et al., 2014) can be identified.

Given the unpredictability of rock instabilities, evasive action is near impossible when an event occurs (Volkwein et al., 2011). Rockfall is a daily occurrence in mountainous areas (Dorren, 2003; Laliberté et al., 2022). The literature describes many examples of the resulting infrastructure damage and human mortality (e.g. Badger and Lowell, 1992; Badoux et al., 2016; Bunce et al., 1997; Chau et al., 2003; Hilker et al., 2009; Porter and Orombelli, 1980). To reduce this risk to infrastructure and human life, a better understanding of this hazard is needed (Dorren, 2003; Erismann and Abele, 2001). TLS is a key tool in achieving that objective. It can help identify unstable rockwall portions that require monitoring (e.g. Kromer et al., 2018; Oppikofer et al., 2008; Royán et al., 2014) and improve our understanding of rockfall triggering factors (e.g. Kromer et al., 2018; Oppikofer et al., 2008; Royán et al., 2014).

This study looks at the influence of weather conditions on the rockfall dynamics in Haute-Gaspésie (Quebec, Canada). Composed of Cloridome Formation sedimentary rock (flysch) (Slivitzky et al., 1991), these rockwalls are poorly consolidated, deformed and highly fractured. Weidner and Walton (2021) showed that in similar geology in Colorado, mitigation activities including mechanical scaling, stabilization with reinforcement rock bolts, wire mesh installation and polyurethane resin injections could be ineffective. They even observed a higher frequency of rockfall after mitigation measures were implemented. Some measures, such as mechanical scaling, were unsuited to highly altered rockwalls. Following scaling operations, the newly exposed rockwall could be just as altered and unstable as the previously

exposed surfaces. Traditional mitigation measures are ineffective on low and moderate magnitude (<1 m^3) instabilities, which corresponds to the magnitude of instabilities caused by weather processes (Weidner and Walton, 2021; Wyllie and Mah, 2004). For highly altered rockwalls such as those found in Haute-Gaspésie, implementing hazard mitigation methods based on the factors that trigger rock instabilities could therefore be the most effective method of limiting hazards associated with rockfall (Laliberté et al., 2022).

Recent literature illustrates significant advances in our understanding of the impact of weather variables on rockfall (D'Amato et al., 2016; Delonca et al., 2014; Macciotta et al., 2015; Matsuoka, 2019; Pratt et al., 2019; Ravanel and Deline, 2011; Weidner and Walton, 2021). The primary objective of our study is to strengthen this knowledge for a geological context neglected by the literature and fill in its main gaps:

- LiDAR data makes it possible to accurately quantify rock instabilities, but they are not always linked to suitable weather data. For example, freeze-thaw cycles are often derived from air temperature without consideration of the influence of solar radiation, even on south-facing rockwalls (e.g. Weidner and Walton, 2021). Furthermore, air temperature provides no insight on freezing front depth in the rock. This makes it difficult to relate spring thaw to the rockfalls that occur (e.g. Macciotta et al., 2015).
- The relationship between rock instabilities and weather conditions is often studied at the monthly or seasonal scale (e.g. Kromer et al., 2018; Macciotta et al., 2017). While this temporality can reveal interesting trends, it cannot differentiate the respective impacts of different meteorological events on rockfall dynamics. For example, on a monthly scale, the respective roles of precipitation events and freeze-thaw cycles cannot be easily distinguished since their occurrences can overlap. Consequently, this temporality is not useful in the preventive hazard management of rock instability triggers.
- Many studies highlight the strong relationship between rockfall frequency and magnitude (e.g. Guerin et al., 2014, 2020; Rosser et al., 2005; Santana et al., 2012;

van Veen et al., 2017; Williams et al., 2018). However, studies into the influence of weather variables on rockwall dynamics focus almost exclusively on rockfall frequency. One exception is Matsuoka (2019), who investigated the relationship between weather conditions and rockfall magnitude. In order to mitigate the risk, the relationship between the magnitude of rock instabilities and their triggering factors is an essential area of study since the damage caused by instabilities is proportional to their magnitude.

Our study therefore aims to link rockfall dynamics to specific adequately measured weather conditions. We use TLS to quantify the frequency and magnitude of rock instabilities for each targeted weather condition. We also propose a classification of weather conditions based on their level of concern for preventive hazard management.

2.4 STUDY SITES

In Haute-Gaspésie, Route 132 is the sole transportation corridor linking a number of villages to the rest of the region. For the local population, it is critical infrastructure for accessing essential services. The national road runs along the Gulf of St. Lawrence shoreline and is subject to coastal flooding and erosion (e.g. Drejza et al., 2014). The rockwalls that tower above the road expose it to other natural hazards: snow avalanches (Fortin et al., 2011; Hétu, 2007), falling ice blocks (Gauthier et al., 2017), debris flows (Fortin et al., 2015), and rockfall. Those same rockwalls make moving the roadway inland from the shore unfeasible. To limit risk to road users, the Ministère des Transports du Québec (department of transportation) created a 24/7 patrol to monitor the 70 km of national road that run along the rockwall of Gaspé's uplands. The patrol is also responsible for clearing the road when it is obstructed by rock, snow or ice from hillslope movements. Between 1987 and 2020, the patrol responded to 13,261 rockfall events along the 25 km where rockwalls overhang Route 132 or 16 rockfalls·year^{-1}km^{-1} (Ministère du Transport du Québec, 2021).

LiDAR was used to monitor three rockwalls (Figure 15, Figure 26 and Figure 27) that overhang Route 132 in Haute-Gaspésie. From east to west, the sites are near the villages of Manche-d'Épée (MAE), Gros-Morne (GMO) and Marsoui (MAR). The total area scanned was 12,056 m^2. Rockwalls were selected using five criteria: 1) structural and lithologic characteristics representative of Haute-Gaspésie rockwalls; 2) frequent rockfall incursions onto the national road; 3) year-round accessibility; 4) general morphology (verticality, height) and microtopography (roughness) compatible with LiDAR acquisition from the national road; and 5) absence of vegetation (occlusion) and drainage (signal reflection). The three sites are sedimentary rockwalls (flysch) with horizontal or subhorizontal bedding planes. The easternmost study site, MAE, covers an area of 3,154 m^2. It has a vertical (>80°) natural rockwall that is 35 m high and is oriented north (350°). It rises over an unvegetated 30 m long scree slope with an average gradient of 38°. The rockwall is primarily composed of siltstone (50%), shale (30%) and greywacke (20%). Rockfall of greywacke blocks is most likely to reach the national road, which runs about 10 m from the base of the scree slope. GMO is a rockwall with alternating spurs and re-entrants. On that site, three rock spurs with a total area of 5,370 m^2 were scanned, most of which have been dynamited. The orientation of the spurs ranges from 330° to 20°, and their gradients range between 70° and 90°. Their bases do not have scree slopes, and rockfall regularly reaches the national road. Only the lower 25 m of the three spurs were scanned to limit occlusion as much as possible. The rock spurs are composed of greywacke (50%), siltstone (40%) and shale (10%). Lastly, MAR is a vertical (90°) dynamited rockwall composed primarily of sandstone (70%), siltstone (20%) and shale (10%). The thickness of the siltstone strata tends to result in decimeter sized instabilities. Since the national road runs right along the base of the rockwall (no scree slope is present), these instabilities regularly reach the roadway. However, its low height (<30 m) and verticality limit the distance of rockfall travel from the rockwall.

Haute-Gaspésie has a humid continental climate with short cool summers, according to the Köppen climate classification system (Beck et al., 2018). During the period 1991–2020, it had an annual mean temperature of 3.9 °C The mean temperatures of the warmest (July) and coldest (January) months were 16.3 °C and -9.2 °C, respectively. Over those same

30 years, average annual precipitation was 888 mm, 33% of which fell as snow (Environment Canada, 2021).

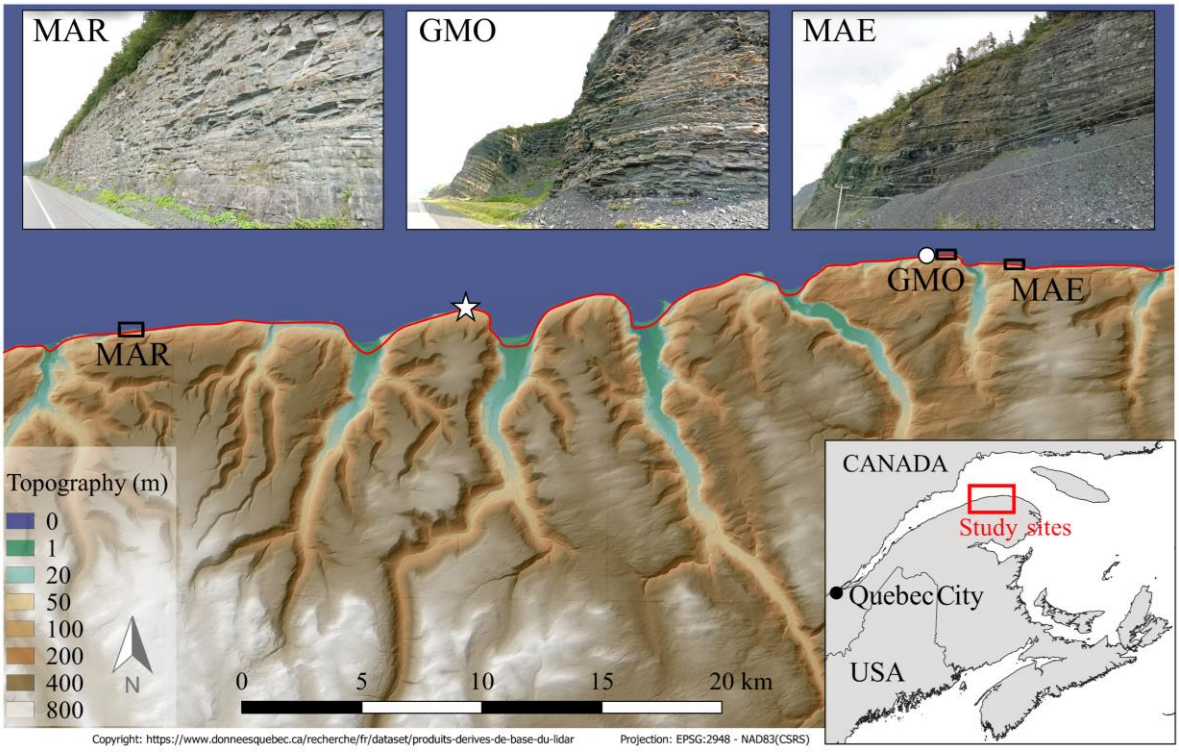

Figure 15. Location of the three study sites (MAR, GMO, MAE), of the rain and snow gauge (white star) and of the thermistor strings that measured the temperature to a depth of 550 cm (white circle). The red line is road 132.

2.5 METHODS

2.5.1 Rockfall detection using a TLS

Over the 554-day period from 14 June 2019 to 18 December 2020, 17 LiDAR surveys were performed. Two TLS were used for data acquisition. The four first surveys used a Leica Geosystems ScanStation C10. A RIEGL VZ-400i was used for the 13 subsequent surveys. To obtain dense point clouds with the fewest possible occlusions, multiple surveys were conducted to adequately cover the scanned surfaces at each site (Figure 16a and Figure 16b).

Depending on site morphology and surface area, four to twelve 360° surveys were needed. The resulting point clouds were processed in the Cyclone 2.5 software. For each date, all these point clouds have been assembled together by a visual alignment using the "2D Scan Thumbnails" tool. Then, the point clouds have been optimized using the "point clouds autocorrelation" tool. This method allows to minimize the number of occlusions and to produce point clouds with a centimeter-level density for each survey (Figure 16c and Figure 16d). The same strategy was used to align the point clouds corresponding to the different dates of acquisition. For each of these dates, we have measured the surface differences between the cloud points using the M3C2 plugin of the open source free software CloudCompare v2.12.4 (Lague et al., 2013). The M3C2 algorithm operates directly on point clouds without meshing or gridding and computes the local distance between cloud points along the normal surface direction which tracks 3D variations in surface orientation. Because it considers the surface roughness, this algorithm is particularly accurate to measure small surface changes and so, it is suitable to compare rockwall surfaces (Lague et al., 2013).

Once the surface differences between each survey have been calculated, we quantified the rockfall volumes between these periods (Figure 16e). Each significative negative change was isolated from the whole point clouds and then, the 2.5D volume calculation method was applied to compute its volume. Štroner et al. (2019) have compared this method, also available in CloudCompare, with software solutions using point clouds capable of calculating volume (Atlas DMT, 3D Reshaper, Leica Cyclone and Trimble RealWorks). They have proven than the 2.5D volume calculation method from CloudCompare provides results identical to those computed by the best commercial solutions and has a much better time demand/accuracy ratio (Štroner et al., 2019). Finally, to avoid misinterpretation of rockfall volumes with, for example, wind deflation of snow or the presence of vegetation, we have focused the analyses on vegetation-free cliff sections. A visual examination of the shape of each of the quantified volumes also helped to minimise interpretation errors (van Veen et al., 2017).

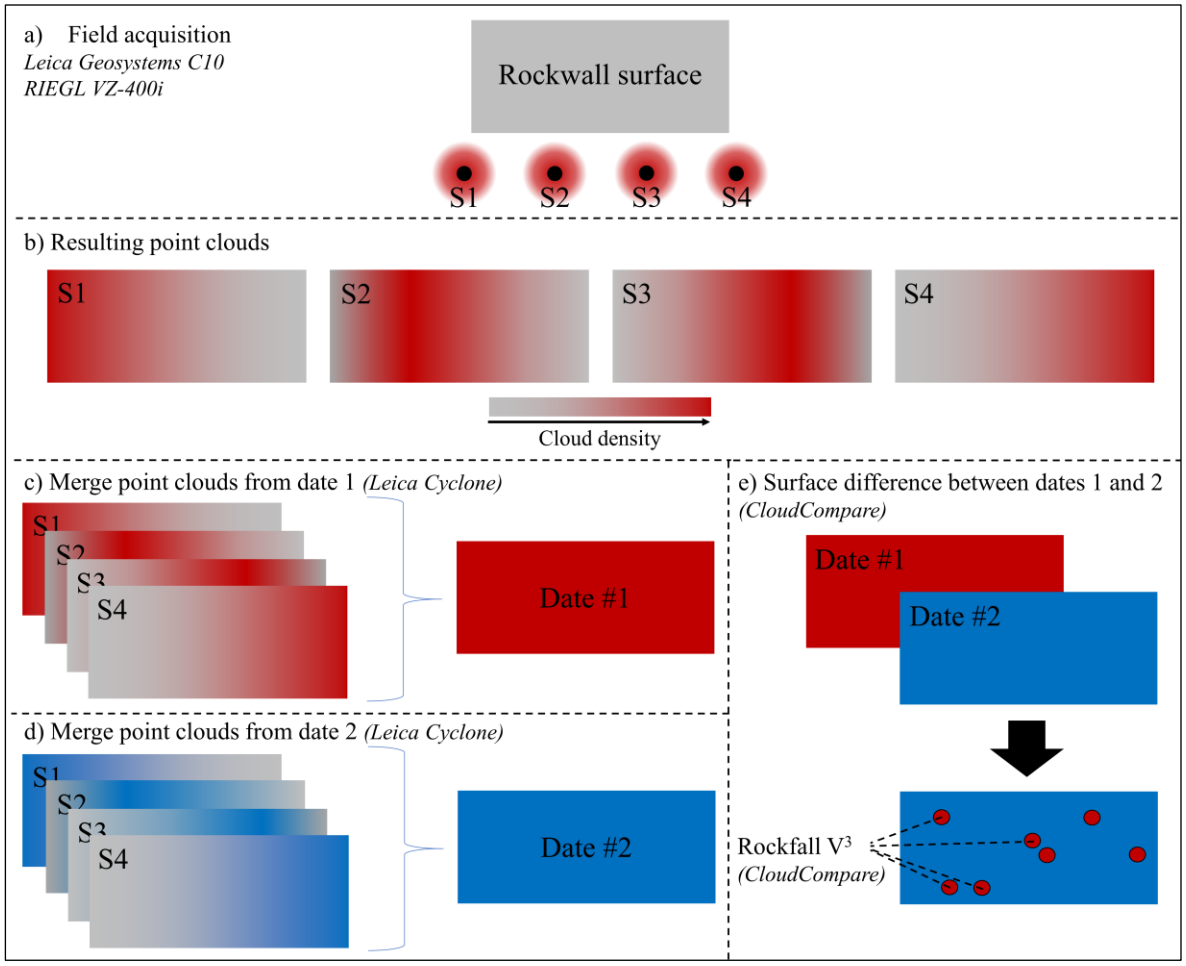

Figure 16. Protocol used to identify and quantify rockfalls from point clouds.

2.5.2 Protocol to monitor the influence of weather conditions on rockfalls

To study the influence of weather conditions on rockfall frequency and magnitude, sufficiently high spatial resolution is needed to identify all events at the lowest quantified magnitude (Abellán et al., 2014). Nevertheless, small-scale rockfalls can be difficult to distinguish from other processes such as wind deflation of snow over the rock slope surfaces. In order to avoid misinterpretation, a threshold of 10 cm for negative change has been

determined and the scarce areas where vegetation is present were excluded of the studied areas. At the end, this method allows exhaustive detection of rockfalls larger than 0.005 m^3.

Regarding the temporal resolution, Barlow et al. (2012) showed that a 19 month interval between surveys leads to an underestimation of small scale events. With overly long intervals, several distinct but spatially overlapping events can be erroneously interpreted as a single larger scale event. Williams et al. (2018) compared rockfall frequencies detected at temporal resolutions of one hour and of 30 days. They found that the number of low magnitude events (<0.1 m^3) detected was three orders of magnitude greater at a temporal resolution of one hour. However, to achieve this high temporal resolution, a fixed scanner is required. This leads to other issues, such as greater occlusion on the rockwall surface and more limited scanned areas. Barlow et al. (2012) showed that while environmental factors influence rockfall, defining a constant frequency is not necessary for data acquisition. LiDAR surveys must be more frequent during periods when a greater rock instability frequency is expected. Conversely, intervals between surveys can be longer during periods with a lower rockfall frequency. The protocol we implemented was designed to limit the scanning effort by targeting selected periods rather than performing regular scans. This resulted in an inconsistent survey frequency that is justified by the influence of weather conditions on rockfalls. The scanning periods were selected based on knowledge of the weather conditions that cause major rock surface deformations and are likely to result in rockfall (Birien and Gauthier, 2022). Target periods could run over several dozen days (dry period, rainy period, autumn period with near-daily freeze-thaw cycles and cold winter period) or monitor specific meteorological events (heavy and high intensity rainfall, winter freeze-thaw cycles and spring surface, 1 m deep and full rockwall thaws).

The periods to scan were determined over the course of the study using Environment Canada weather forecasts and then validated with local weather measurements. A Campbell TE525WS-L rain gauge was used to measure precipitation (mm). In winter, it was equipped with a CS705 adapter to measure the water equivalent of solid precipitation. A thermistor string (with a GeoPrecision data logger operating at 915 MHz) inserted into a

horizontal borehole measured the temperature (°C) every 30 cm to a depth of 550 cm. Using linear interpolation between the thermistors, we produced a temperature profile at different depths over time, quantified the number and depth of freeze-thaw cycles and tracked the depth of the freezing front in winter and the thawing front in spring. All weather instruments took data readings every 15 minutes. The instrumented rockwall is located 200 m west of the study site GMO (49°15'21.0"N 65°33'52.2"W) and the precipitation data comes from a weather station located in a roadside rest area along the Gulf of the St-Lawrence (49°13'49.92"N 65°51'3.53"O) (Figure 15).

Finally, the rockfall spatial distribution as well as its frequency and the rock slopes erosion rates are presented individually for the three study sites but the influence of weather conditions is based on the whole rockfall database. This approach has proved necessary to avoid misinterpretation of the occurrence or non-occurrence of events during short microclimatic periods (e.g. heavy and high intensity rainfall or winter freeze-thaw cycles). Monitoring over a longer period would make it possible to establish links between the meteorological conditions and the geological and structural context of each of the studied rock slopes.

2.5.3 Hazard assessment

LiDAR surveys make it possible to quantify rockfall frequency and to calculate their individual volume. Based on this data, we can study the influence of different weather scenarios on rockfall magnitude. Because a high frequency of high magnitude events does not have the same significance as a high frequency of low magnitude events, the magnitude of rockfalls is a major issue for risk management. Following this precept, we have grouped and classified the 9 main weather scenarios in a matrix according to their ability to trigger rockfalls of different magnitudes. This matrix is composed of three magnitude classes (“low”, “intermediate” and “high”) and five frequency classes from “low” to “extreme”. This table provides a classification of weather conditions based on their ability to trigger rockfalls of

different magnitudes. This knowledge could be used to implement a risk management strategy based on triggering factors.

2.6 RESULTS

2.6.1 Frequency-magnitude

Over the study period, 1,287 rockfalls over 0.005 m^3 in volume were identified and their volumes measured. Rockfall frequency decreased rapidly with magnitude (Figure 17a). The frequency-magnitude curves generally fit a power law (Guerin et al., 2014, 2020; Hungr et al., 1999; Rosser et al., 2005; Santana et al., 2012; van Veen et al., 2017; Williams et al., 2018). In this case, it can be defined as:

$$f(V) = 0.0168\mathrm{V}^{-1.06}$$

where f(V) is the mean daily frequency of rockfalls with a volume greater than or equal to V over the entire study period for the 12,056 m^2 of scanned rockwalls. This frequency is the equivalent of 2.2 rockfalls·d^{-1} for events greater than or equal to 0.01 m^3, 0.2 rockfalls·d^{-1} for events greater than or equal to 0.1 m^3, and 0.02 rockfalls·d^{-1} for events greater than or equal to 1.0 m^3. 69 rockfalls have a volume higher than 0.15 m^3, (i.e. 5.3% of the total) of which 17 have higher than 0.5m^3 (i.e. 1.3% of the total) and 7 higher than 1 m^3 (i.e. 0.5% of the total) (Figure 17). Where the frequency or spatial resolution of the LiDAR surveys is insufficient, low magnitude instabilities are underrepresented (Barlow et al., 2012; Guerin et al., 2014; Malamud et al., 2004). The absence of a rollover in the logarithmic frequency-magnitude distribution obtained in this study makes it possible to validate whether a suitable instability detection threshold was chosen (Figure 17b). This result confirms that the selected survey frequency and spatial resolution were appropriate for individually identifying the large majority of events with a volume exceeding 0.005 m^3.

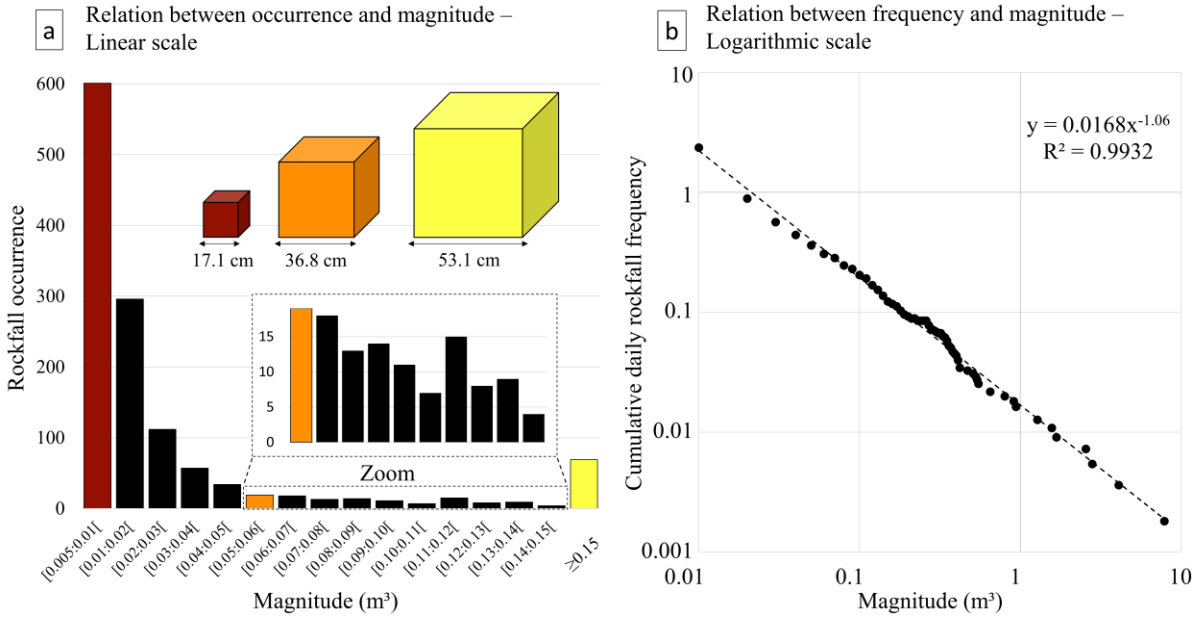

Figure 17. Relationship between rockfall occurrence and magnitude (a) and between cumulative daily rockfall frequency and magnitude (b).

2.6.2 Global rockwall erosion rate

The annual rockwall erosion rates and the rockfall frequency were calculated using the entire 554-day time series of two summers and two autumns but only one winter and one spring. The 1,287 recorded rockfalls were distributed across the three study sites as follows: 363 at MAE, 486 at GMO and 438 at MAR. Figure 18, Figure 26Figure 27 show the surface differential at the three study sites between the first survey in June 2019 and the last survey in December 2020. On these figures, we have filtered out any change less than +/-1 cm and green clusters of points correspond to positive change and red clusters of points correspond to negative changes. Over the 554-day period, many changes were visible on the rockwall surfaces. Most of the positive changes (in green) to the rockwall and scree slope are explained by low snow accumulation during the last LiDAR surveys on 18 December 2020. These positive changes can also be attributed to the development of rock instabilities large enough

to be detected by LiDAR (Kromer et al., 2018; Oppikofer et al., 2009b; Oppikofer et al., 2008; Royán et al., 2014). For example, measurements taken at MAE show that between the months of June 2019 and December 2020, a rock mass measuring 3 m high separated from the rockwall by 4 to 5 cm at its top and 1 to 2 cm at its base (Figure 18a). The increased rate of displacement at the top of the rock mass suggests a toppling failure. This type of pre-failure deformation was not considered in the rockfall volume calculation. Only rockfalls that produced a negative change of more than 0.005 m^3 in the surface differential were considered in the erosion rate calculation. Because rockfalls of very small magnitude (< 0.005 m^3) were not considered, the erosion rates are slightly underestimated. It is important to recall that what appears to be a high magnitude event over the entire study period may correspond to several successive smaller-scale events (Figure 18b) (Abellán et al., 2014; Barlow et al., 2012; van Veen et al., 2017; Williams et al., 2018). The change detection of +/-1 cm applied in Figure 18, Figure 26Figure 27 was only used to visualize the overall picture of the rock slope dynamic (e.g. snow accumulation, pre-failure deformation) but as described before, a filter of +/- 10 cm was applied to quantify rockfalls.

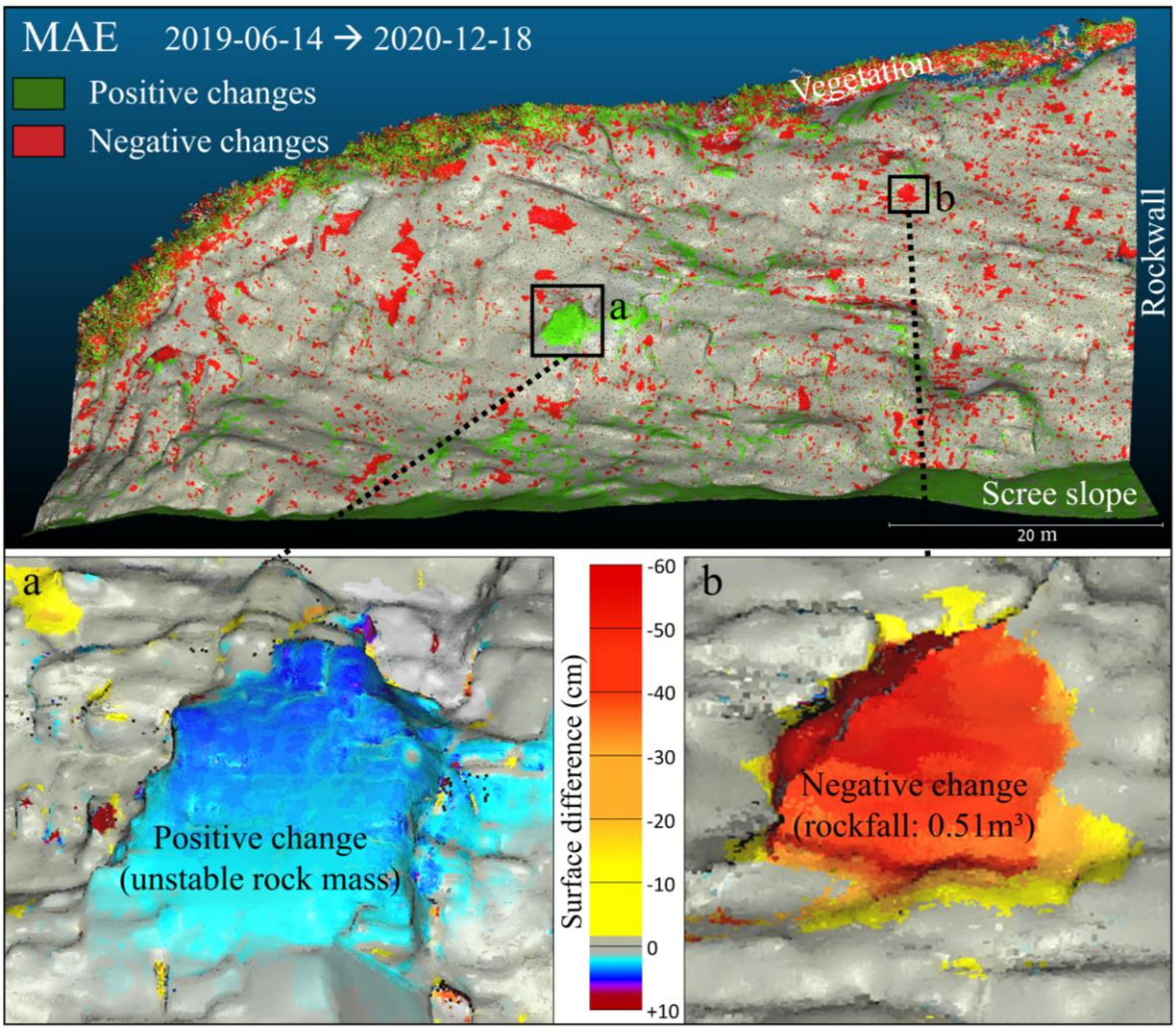

Figure 18. Point clouds of main changes (MAE rockwall) between the first (14 June 2019) and last (18 December 2020) scan surveys. Positive changes are mainly relative to unstable rock mass (a) and negative changes highlight rockfall (b).

Considering the scanned surfaces separately, all three sites had fairly similar annual rockfall frequencies: 0.08 rockfalls·m^{-2} for MAE and MAR, and 0.06 rockfalls·m^{-2} for GMO (Figure 19a). In contrast, the differences between the erosion rates of the three rockwalls were more pronounced. Over the study period, the erosion rate was higher for MAR (5.4 mm·y^{-1}) than for MAE (3.0 mm·y^{-1}) or GMO (2.8 mm·y^{-1}) (Figure 19b). Therefore,

despite comparable rockfall frequencies, MAR had a higher erosion rate than the other sites. This distinction shows that on average, MAR experienced higher magnitude events. This is borne out by the fact that in the entire time series, 5 of the 7 recorded events with a volume of over 1 m^3 occurred at MAR. These events account for 33% of the total volume lost by the three rockwalls in the study period. At MAR, the eight largest magnitude events contributed as much to the erosion rate of the studied surface as the 430 lower magnitude events. Meanwhile, at GMO and MAE, the 5 and 20 highest magnitude events represented the volume of the 481 and 343 smallest events, respectively. Clearly, high magnitude events affect more substantially the erosion rate of the rockwalls (Figure 19c).

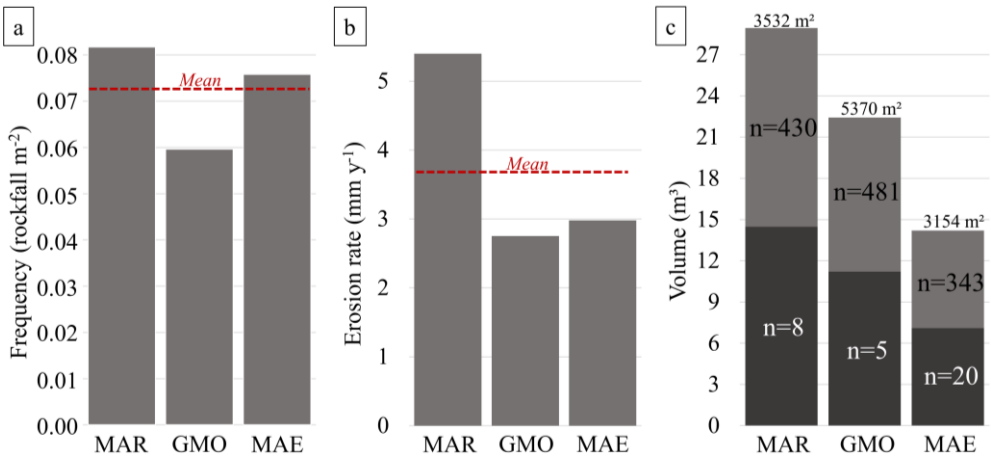

Figure 19. Mean annual rockfall frequency (a), rockwall erosion rate (b) and total volume of rockfall for the overall studied period (c).

2.6.3 Weather conditions related to rockfalls

In this study, LiDAR surveys made it possible to quantify instabilities over 16 distinct periods (Figure 20). Three of them totaling 104 days with a mean precipitation of 1.4 $mm \cdot d^{-1}$ were defined as dry periods (DRY). Two periods totaling 100 days and a mean precipitation of 4.1 mm d^{-1} were defined as rainy periods (RAINY). Two periods totaling 93 d with a mean

air temperature below the freezing point (-6.2 °C) and very low winter freeze-thaw frequency (0.02 thaws·d^{-1}) were defined as cold winter periods (WIN. <0 °C). The autumn periods (AUT. FT) experienced the first freeze-thaw cycles after summer. Two autumn periods totaling 79 days were scanned. The specific meteorological events that were monitored included a heavy (54 mm) and high intensity (4 mm h^{-1} for 12 h 45 min) rainfall event in September 2019 (HEAVY RF) and two winter freeze-thaw cycles (WIN. FT) in winter 2020. One of these two winter freeze-thaw cycles was accompanied by rainfall. Since this kind of liquid precipitation event is only possible because of the thaw occurrence, we made the choice to consider this period as a WIN. FT. Four LiDAR surveys were used to segment the spring thaw (SPR. MELT) into three periods (Figure 21). The first phase corresponds to the initiation of the thawing season including two freeze-thaw events reaching a depth of 50 cm from the rockwall surface (SPR.0:50). The second phase is characterized by a thaw that penetrates to a depth of 95 cm and by a thaw of 77 cm from depth (SPR.50:100). The third phase corresponds to the complete thaw of the rockwall (SPR.100:350) (Figure 21). Lastly, the period between 25 May and 16 September 2020 experienced a range of weather conditions too varied for categorization (Figure 20).

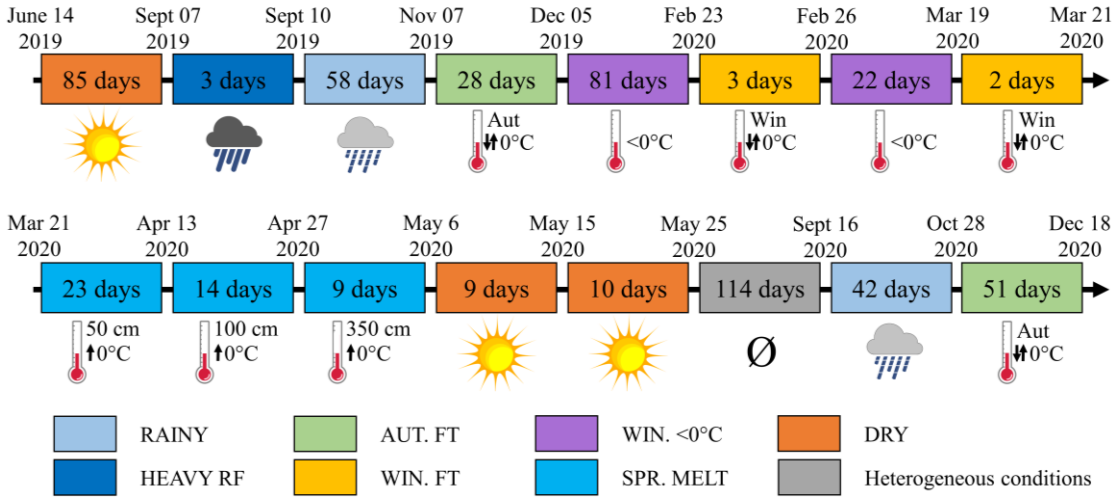

Figure 20. Targeted weather conditions for each scan survey period, 14 June 2019–18 December 2020 (553 d).

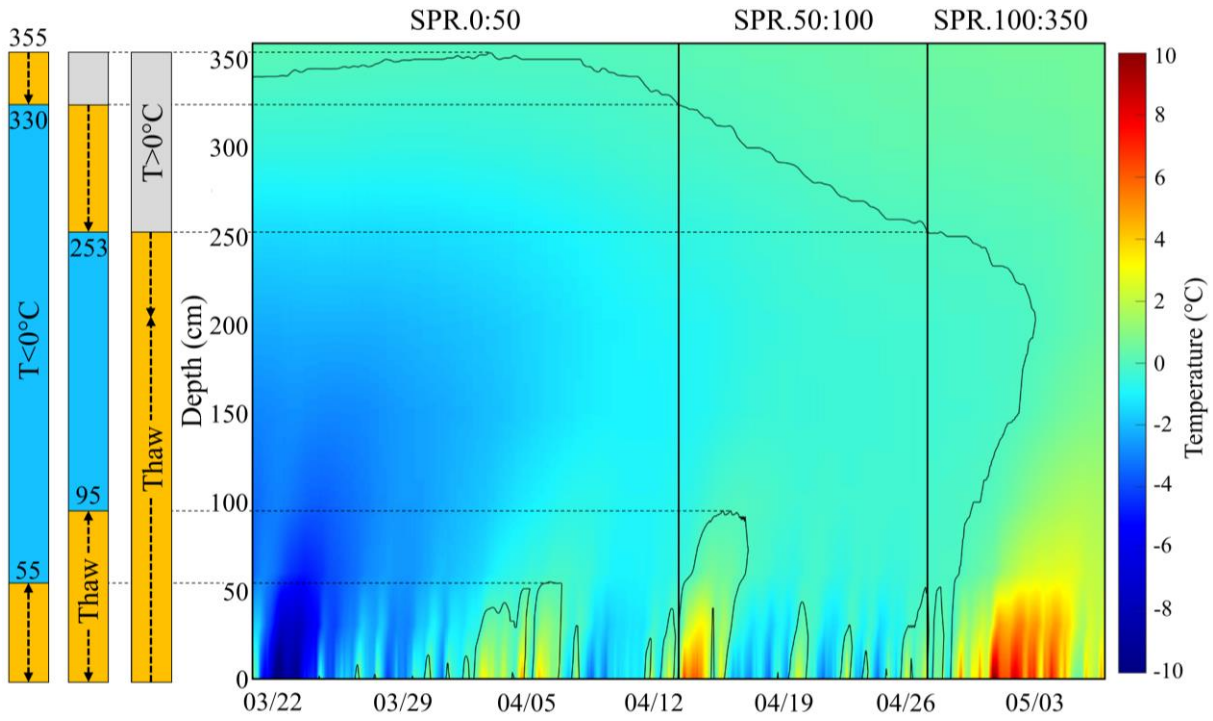

Figure 21. Rock temperature evolution along a perpendicular profile from surface to 360 cm depth, 21 March 2020–6 May 2020. Dark time series are for freeze-thaw depth (0 °C). Vertical lines delimit scan periods.

In decreasing order, 241 rockfalls were associated with RAINY periods, 178 with AUT. FT periods, 145 with DRY periods, 120 with SPR. MELT periods, 97 with WIN. <0 °C periods and 91 with the HEAVY RF period and 44 with WIN. FT periods (Figure 22a). However, rockfall occurrence under these meteorological conditions is not representative of the dynamics of rockwall instability since some of those conditions occur over a much longer period than others. For example, DRY periods total 104 days, while WIN. FT periods total just four. Considering rockfall frequency rather than occurrence revealed different meteorological conditions as triggering factors of instabilities. WIN. <0 °C and DRY were associated with the lowest daily rockfall frequencies, respectively 0.9 and 1.4 events d^{-1} across the full scanned surface area (12,056 m²). This frequency tended to double under AUT. FT (2.2 events·d^{-1}), RAINY (2.4 events·d^{-1}) and SPR. MELT (2.6 events·d^{-1}) conditions. Winter freeze-thaw cycles (WIN. FT) and heavy rainfall events (HEAVY RF) produced the highest rockfall frequencies. Frequencies for WIN. FT and HEAVY RF were 11.0 and 30.3 events d^{-1}, respectively (Figure 22b). Compared to a cold winter period (WIN. <0 °C), rockfall frequency was multiplied by a factor of 1.5 during DRY periods, 2.3 in AUT. FT periods, 2.8 in SPR. MELT periods, 11.7 in WIN. FT periods and 32.3 in HEAVY RF periods.

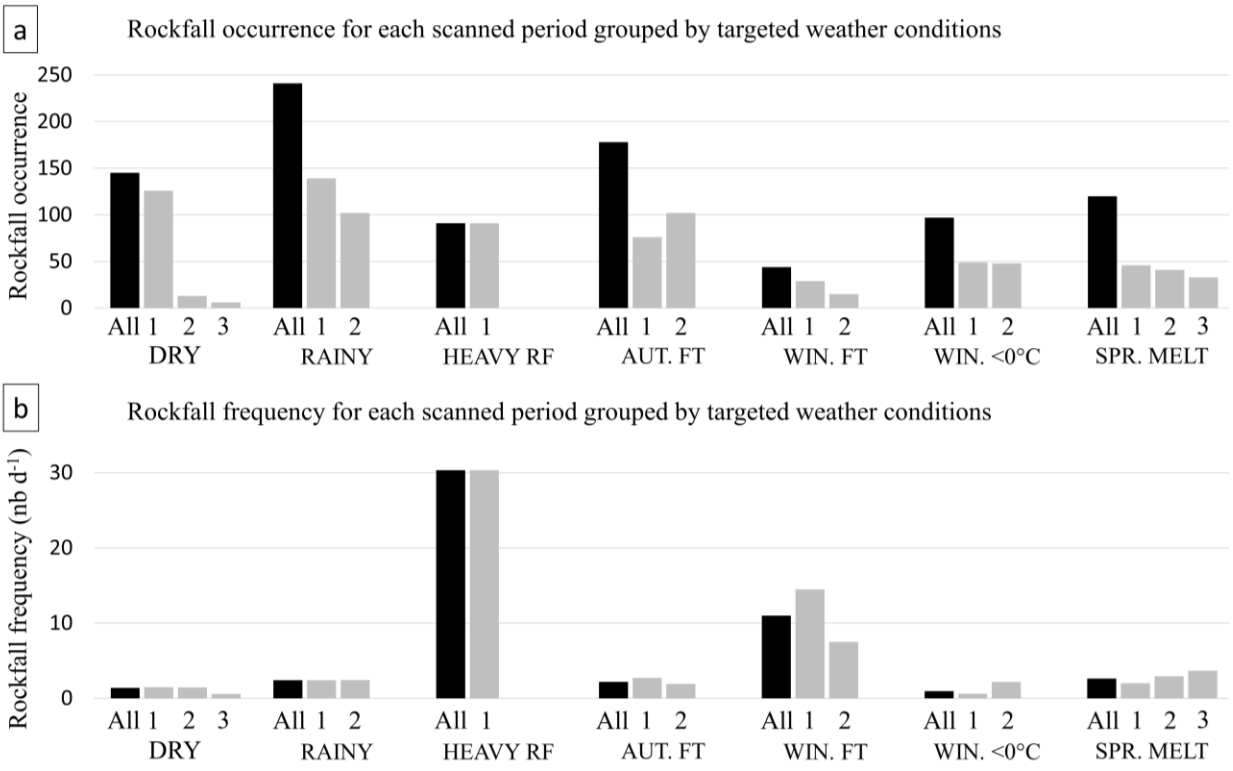

Figure 22. Rockfall occurrence (a) and frequency (b) for each scanned survey period, grouped by targeted weather conditions for all sites.

For each scanned survey period, precipitation intensity and freeze-thaw cycles were compared with rockwall erosion rates and rockfall frequency (Figure 23). The erosion rate and frequency shown for each period are relative to their respective mean values over the entire time series (standard score). Where values for a period were under one, the rockwall erosion rate and rockfall frequency were less than the time series mean. On 7 September 2019, Category 5 hurricane Dorian arrived in the Gulf of St. Lawrence as a post-tropical storm. It dropped 54 mm of heavy rain (4 $mm \cdot h^{-1}$ for 12 h 45 min) on the study site. Between 1987 and 2021, only 16 precipitation events of over 50 mm were recorded in Haute-Gaspésie, which represents a return period of 776 days (Environment Canada, 2021). The heavy rain event resulted in a rockwall erosion rate and rockfall frequencies that were 9.3 and 13.8 times the mean, respectively (Figure 23). Calculated for the full 72 h period between the two

surveys (7 and 10 September 2019), those values would undoubtedly have been higher had they had been based solely on the actual duration of the event (14 h).

Between 23 and 26 February 2020, a series of three freeze-thaw cycles occurred (Figure 23). They followed a long period (70 days) of below freezing point temperatures. During these three freeze-thaw cycles, the air temperature rose to 3.1 °C, 8.3 °C and 2.1 °C, respectively, separated by 8 h periods around -2 °C. They resulted in a thaw 10 cm depth from rockwall surface. The rockwall erosion rate and rockfall frequency were 6.3 and 8.5 above the mean, respectively. The absence of rain during this period highlights the leading role of surface thaws in rockslide dynamics (Figure 23). The air temperature remained below the freezing point until 20 March 2020 before rising above zero for 24 hours, briefly reaching a high of 8.1 °C. This produced a surface thaw to a depth 14 cm accompanied by rockwall retreat and rockfall frequency rates of 2.3 and 4.4 times the mean, respectively (Figure 23). In the spring, the frequency and magnitude of freeze-thaw cycles increased (Figure 21 and Figure 23). Rockfall frequency remained fairly low and lower than during the last winter freeze-thaw event (1.7 times more than the mean). In contrast, erosion rates were higher than during the freeze-thaw event on 23 and 26 February and remained high for a period of 24 days (2.5 times more than the mean). This combination of a high erosion rate and fairly low rockfall frequency indicates an increased mean rockfall volume during the spring thaw.

Over the study period, the weather conditions that most contributed to rock instability dynamics were the winter freeze-thaw cycles, the spring thaw and the heavy and high intensity rainfall event (Figure 23). In contrast, other weather conditions were associated with high stability in the studied rockwalls. In the period 5 December 2019–23 February 2020, both the rockwall erosion rate and rockfall frequency were very low, 0.6 and 0.3 times less than the mean, respectively (Figure 23). Temperatures remained below freezing point on all but two days of this 81-day period. The 19-day period 6–25 May 2020 had very low rockwall erosion rates and rockfall frequency (0.2 and 0.6 times less than the mean, respectively). During that period, rockwall temperature remained constantly below freezing and only 5.6 mm of rain was recorded. In the study period, the cold winter and dry summer periods

experienced the weather conditions associated with the highest stability in the scanned rockwalls (Figure 23).

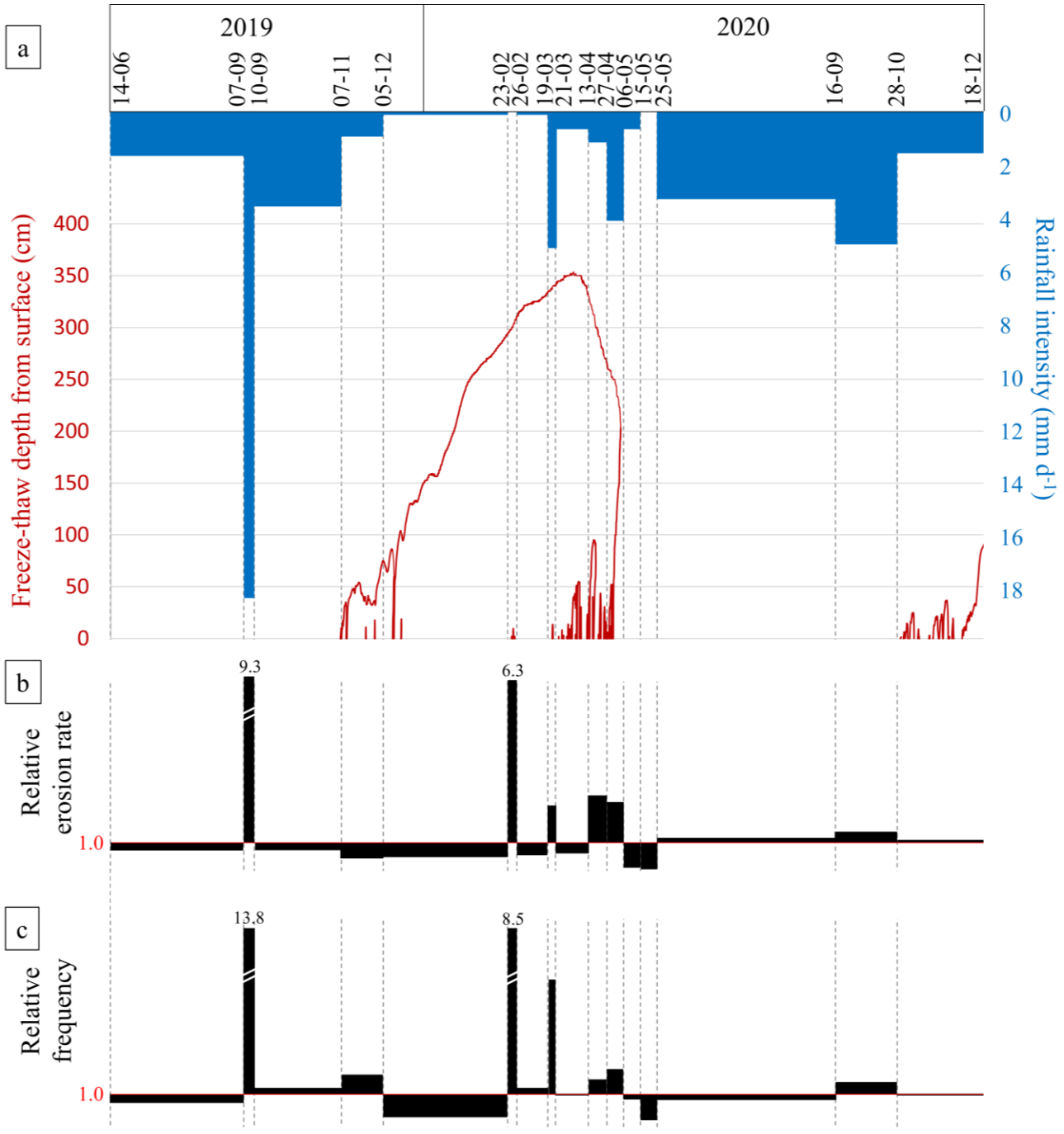

Figure 23. Main weather conditions (a), erosion rates (b) and rockfall frequency (c) for each scanned survey period. Erosion rates and rockfall frequency are respectively relative to mean erosion rates and mean rockfall frequency between 14 June 2019 and 18 December 2020.

2.6.4 Hazard assessment

LiDAR surveys make it possible to quantify rockfall frequency and calculate the individual volume of each rockfall. Using this data, we can study the influence of different weather conditions on rockfall magnitude. Figure 24a presents a matrix of the weather conditions associated with different rockfall frequencies and magnitudes. We defined three classes of "low", "intermediate" and "high" magnitudes. The first one includes 1,100 low magnitude (0.005:0.05 m^3) events. The second class comprises 119 events of intermediate magnitude (0.05:0.15 m^3), while the third includes 68 events of the highest magnitude (≥ 0.15 m^3). We also defined five frequency classes for the matrix: low (<75% mean frequency for the study period), moderate (75:125%), high (125:300%), very high (300:500%) and extreme (> 500%).

HEAVY RF weather condition coincides with extreme rockfall frequency of both low and high magnitude events. In contrast, DRY, WIN. <0 °C, SPR.0:50 and AUT. FT conditions were associated with low frequency rockfall, irrespective of magnitude. All of those weather conditions had an impact on rockfall frequency, resulting in either widespread instability (HEAVY RF) or, conversely, widespread stability (DRY, WIN. <0 °C, SPR.0:50 and AUT. FT). However, while there is no clear relationship between those conditions and rock instability magnitude, the WIN. FT, SPR.50:100, SPR.100:350 and RAINY conditions led to rockfall frequencies that varied by magnitude. WIN. FT is associated with extreme frequencies of low and moderate magnitude instabilities, but only high frequencies of large instabilities. Similarly, RAINY and SPR.50:100 are associated with high frequencies of low magnitude events but moderate to low frequencies of high magnitude events. The inverse relationship was observed during the thawing period in depth (SPR.100:350). This critical period was dominated by high magnitude rockfalls that outnumbered low magnitude ones (Figure 24a).

The cumulative daily occurrence of targeted weather conditions is drawing only on data collected during the first year of the study (14 June 2019–13 June 2020) rather than the entire time series in order to give each season an equal weight (Figure 24b). In that year, HEAVY RF and SPR.100:350 periods accounted for just 11 days. There was therefore a low occurrence of periods with weather conditions favorable to extreme frequency high magnitude events. The WIN. FT, SPR.0:50, SPR.50:100 and AUT. FT periods were also associated with high frequency or high magnitude rockfall and represent a cumulative occurrence of 44 days between 14 June 2019 and 13 June 2020 (Figure 24b). Lastly, the DRY, WIN. <0 °C and RAINY periods, which do not coincide with periods of high instability, accounted for 310 days, or 85% of the year (Figure 24b). Thus, on an annual scale, the weather conditions that resulted in high frequency or magnitude rockfall are in a small minority.

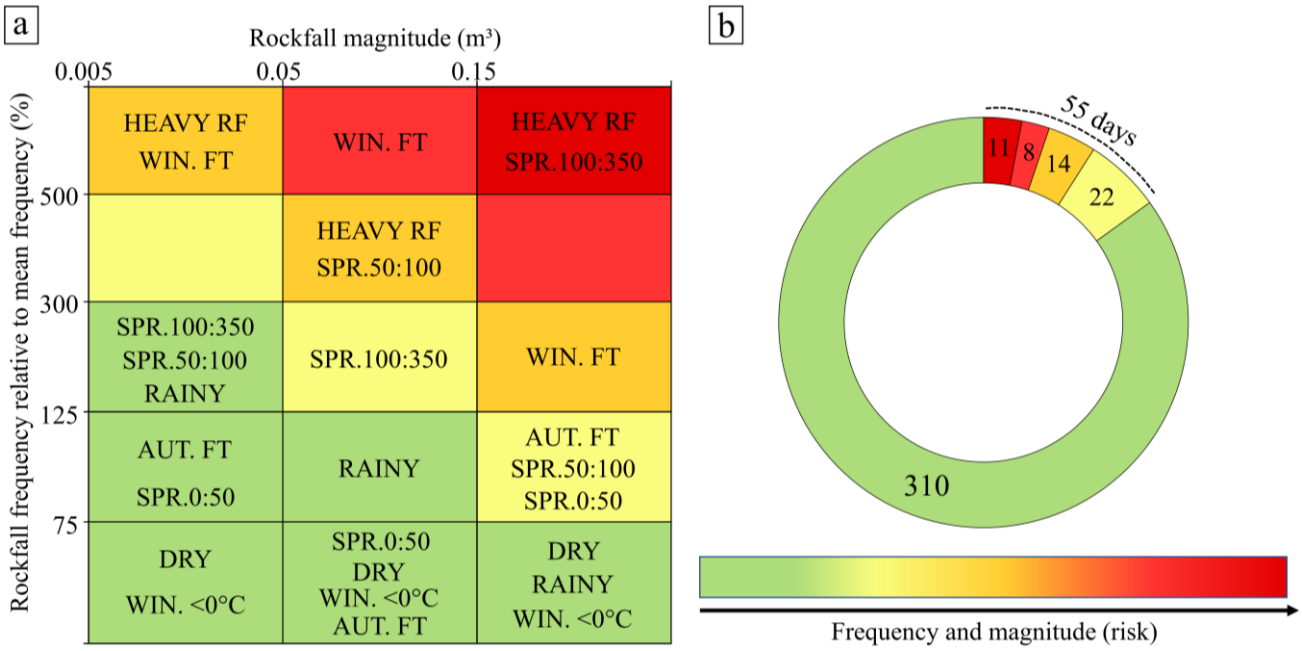

Figure 24. Hazard assessment matrix showing the relationship between rockfall magnitude and frequency for specific weather conditions (a) and cumulative daily occurrence of those conditions during the first complete year of this study (14 June 2019 to 13 June 2020) (b).

2.7 DISCUSSION

2.7.1 Flysch rockwall erosion rate

The annual erosion rates measured over 554 days for the three flysch rockwalls in Haute-Gaspésie are very high (between 2.8 and 5.4 mm·y^{-1}) compared to reported rates for various lithologies and climate patterns (e.g. André, 1997; Barsch, 1977; Beylich, 2000; Curry and Morris, 2004; Hinchliffe and Ballantyne, 1999; Höllerman, 1983; Humlum, 2000; Olyphant, 1983; Sass, 1998). They are nonetheless perfectly consistent with those reported by Hétu and Gray (2000) for a 40 m flysch rockwall in the same study area (3.2 mm·y^{-1}). Those rates were measured by weighing the sediment accumulated on plastic tarps placed at the foot of rockwalls (Hétu and Gray, 2000). Direct measurements by TLS are extremely

accurate, making it possible to quantify the erosion rates of rockwalls in their morphoclimatic environments with a greater degree of certainty. The agreement between the results from the two methods demonstrates that they are both valid. However, surveys over very short periods clearly tend to underestimate actual rates by limiting the likelihood of observing very high magnitude events that would have a significant influence on erosion rate (e.g. Korup and Clague, 2009; Krautblatter and Dikau, 2007). Continuing to survey these rockwalls would confirm the accuracy of the erosion rates presented here. TLS is a modern method that merits more widespread use in monitoring projects of this type and to build on our understanding of rockwall retreat and erosional feature dynamics (e.g. Ballantyne and Kirkbride, 1987; Duszyński et al., 2019; Higgins and Coates, 1990; Rapp, 1960).

2.7.2 Relationship between meteorological conditions and rockfall

Rockfall frequency during RAINY periods was 1.7 times higher than the mean relative to DRY periods. The highest magnitude and strongest intensity rain event (HEAVY RF) was associated with rockfall frequency 9.3 times higher than the study period mean, or 21.6 times higher than during a dry period. Only RAINY conditions led to an increased frequency of low magnitude instabilities, while HEAVY RF conditions resulted in a significant increase in the frequency of high magnitude instabilities (Figure 24). These results agree with those obtained in other geological and climatic contexts. For the limestone rockwalls of Isère, France, D'Amato et al. (2016) showed that rockfall frequency was 2.5 to 3 times higher during rain events than during the dry summer period, up to 7.5 higher during high magnitude rain (> 30 mm) and 27 higher during high intensity rain (> 5 mm h^{-1}). For the rockwalls of Réunion Island, Delonca et al. (2014) showed that high magnitude rain (> 120 mm) resulted in an eightfold increase in the probability of daily rockfall. The lack of a time lag between rain events and instabilities shows that this precipitation has a nearly immediate (<24 h) triggering effect on rock instabilities. In the Japanese Alps, Matsuoka (2019) demonstrated the impact of liquid precipitation on increased water content and subsequent rockfall

triggering. Certain high intensity rain events were associated with instabilities of one to multiple meters in size. These studies, like our own, clearly show that rain events are aggravating and triggering factors of rockfall. However, they do not detail the process by which rainwater contributes to the formation of instabilities or improve our understanding of how water moves through the highly fractured rock layer near rockwall surfaces (Magnin et al., 2021; Stoll, Scandroglio, and Krautblatter, 2020). It is well known that an increase in hydrostatic pressure in discontinuities reduces shear strength (Selby, 1993; Wieczorek and Jäger, 1996; Wyllie and Mah, 2004). Groundwater recharge and hydrostatic pressure at depth have been put forward as kinematic factors in large rockslides (Cloutier et al., 2015; Crosta et al., 2013). However, how rainwater influences the development of superficial instabilities is less well documented. In clay-rich rock, it has been shown that water content variations at the rockwall surface lead to irreversible mechanical deformations (Birien and Gauthier, 2022) that could trigger rockfall. Rockwall surfaces can experience wide fluctuations in water content. Rain events result in subsurface runoff in the altered surface layer of rockwalls and represent a significant water input. This input can be amplified when wind spreads a layer of rain water over rockwall surfaces (Sass, 2005a). This type of subsurface runoff can clearly contribute to reducing shear strength and trigger rockfall during high intensity rain events (Selby, 1993). Conversely, direct solar radiation on rockwall surfaces can lead to rapid and significant drying of the first decimeters of rock (Burnett et al., 2008). Limited access to rockwalls and the challenge of directly measuring water pressure limit our ability to measure moisture dynamics in this surface layer of rock and interpret its influence on the development of rock instabilities.

In this study, rockfall frequency was 11.7 times higher during winter freeze-thaw cycles (WIN. FT) than during cold periods when the temperature remains below the freezing point (WIN. <0 °C). We therefore observe that high rockfall frequencies occur during thawing periods (WIN. FT), while rockwalls remain very stable during the phases of the freezing process (WIN. <0 °C). The freezing phase can cause fractures to open (Coutard and Francou, 1989; Matsuoka, 2008; Matsuoka and Sakai, 1999). However, cohesion at the ice-rock interface is generally sufficient to hold newly unstable blocks of rock in place (Fiorio et

al., 2002; Krautblatter et al., 2013). Consequently, rockfalls occur when the ice melts, such as during winter freeze-thaw cycles. This finding supports those of D'Amato et al. (2016), who showed that in limestone rockwalls in Isère, France, the frequency of rock instabilities is seven times higher during freeze-thaw cycles. Similarly, Delonca et al. (2014) found that rockfall frequency was doubled on basalt and granite rockwalls in Auvergne, France, for freeze-thaw cycles with a minimum temperature of -5 °C. Our results also show that freeze-thaw cycles are associated with a very high frequency of low and moderate magnitude events but that their impact is limited when it comes to higher magnitude events (Figure 24a). This is consistent with the fact that winter freeze-thaw cycles influenced only the first 15 cm from surface (Figure 24a). Winter thaws can be accompanied by rainfall (Figure 23) and a compounding effect of these conditions probably occurs when they are combined. Autumn freeze-thaw cycles (AUT. FT) do not appear to be as effective at developing rock instabilities as winter freeze-thaw cycles. Their associated frequency of rockfall is near the annual mean for both low and high magnitude instabilities (Figure 24a). This is likely partly due to the fact that autumn freeze-thaw cycles were not studied individually. The two AUT. FT periods were 28 and 51 days long, respectively. They also coincided with weather conditions unmarked by high rockfall frequency that decreased the average frequency of rockfall specific to autumn freeze-thaw cycles. Matsuoka (2019) also notes that even if the temperature fluctuations around the freezing point penetrate to 40 cm in depth, the water in the pores and discontinuities does not necessarily freeze – or freeze completely – due to its high heat capacity. Lastly, the high intensity autumn rain events that preceded the period of many autumn freeze-thaw cycles (AUT. FT) may have purged the rockwall surface of its most unstable rock, leaving very little rock in a nearly unbalanced state.

The superficial spring thawing phase (SPR.0:50) does not appear to be a particularly unstable period, even for low magnitude events (Figure 24a). However, the thaw in the first meter of rockwall (SPR.50:100) results in very high frequency of moderate magnitude instabilities. When thawing at depth (SPR.100:350) occurs, the frequency of high magnitude instabilities increases (Figure 24a). This relationship between seasonal freezing depth and rockfall magnitude is widely recognized (e.g. Dramis et al., 1995; Matsuoka, 2019; Matsuoka

and Murton, 2008), but for the first time, this study compares the magnitude of rock instabilities with measurements of the spring thawing front at depth. The winter freeze-thaw cycles (WIN. FT) that occurred before the first thawing phase (SPR.0:50) may have been responsible for purging the first decimeters of rockwall surfaces and explain why SPR.0:50 conditions are not associated with an unstable period. This surface thaw phase lasted 23 days. During that period, negative temperatures continued to dominate (conditions equivalent to WIN. <0 °C) and probably tended to attenuate rockfall frequency throughout the period. At greater depth, the spring thaw is the only thaw of the year (Figure 21 and Figure 23). Consequently, the mechanical action of this high amplitude freeze-thaw cycle has strong potential to destabilize rock portions (Dramis et al., 1995; Matsuoka, 2019; Matsuoka and Murton, 2008). The impact of the spring thaw on high magnitude rockfall is amplified by water advection associated with snow cover melting, groundwater recharge and ice melting in rock discontinuities and pores. As spring progresses, rain precipitation becomes predominant, further increasing water inputs (Hasler et al., 2011). Large magnitude rockfall is likely to result from the reduced cohesion associated with ice melt and increases in hydrostatic and interstitial pressure in the altered layer of rockwall surfaces (Matsuoka, 2019; Schovanec, 2020; Wieczorek and Jäger, 1996).

Among the contributing factors to rock instability development, the roles of precipitation and freeze-thaw cycles are predominant (e.g. Collins and Stock, 2016; Coutard and Francou, 1989; D'Amato et al., 2016; Hungr et al., 1999; Matsuoka and Sakai, 1999; Rapp, 1960; Wieczorek and Jäger, 1996). To a lesser degree, other weather phenomena can trigger rockfall. Large temperature fluctuations cause expansion and contraction within rock masses that can eventually result in rockfall (Collins and Stock, 2016; Eppes et al., 2016; Matsuoka, 2019). The impact of thermal cycles on the rockfall dynamics of the highly altered north-facing rockwalls of Haute-Gaspésie was considered to be minor and was not quantified in this study.

2.7.3 Rockfall hazard management

The magnitude of rockfalls is a major issue in risk management. Large dimension blocks tend to travel longer distances (e.g. Dorren, 2003). If they reach part of the natural or built environment that is exposed, they have a larger probability of causing damage. Therefore, in risk management, a high frequency of high magnitude events does not have the same significance as a high frequency of low magnitude events. The rockfall on 16 April 2019 that occurred 1.3 km west of the MAE site resulted in the temporary closure of Route 132 (Figure 25). It took place 18 hours after the first thaw to 60 cm in depth and coincided with the spring thaw (SPR.50:100). It also occurred immediately after a 20.1 mm rainfall event (HEAVY RF). In retrospect, the SPR.50:100 and HEAVY RF conditions meant that extremely high frequency high magnitude rockfall was likely (Figure 24). From a risk management standpoint, forecasting a major event such as the one on 16 April 2019 is possible using the risk assessment matrix developed in this study. High intensity rain (HEAVY RF) and spring thaw SPR.100:350 were identified as the weather conditions of greatest concern for public safety since they result in extreme frequency high magnitude events (Figure 24a). In our first full year of data collection (14 June 2019–13 June 2020), these conditions only occurred on 11 days (Figure 24b). The other weather conditions that lead to increased rockfall frequency and magnitude (WIN. FT, SPR.0:50, SPR.50:100 and AUT. FT) add 44 more days of concern. From the perspective of rockfall forecasting, it is noteworthy that potentially hazardous conditions are present only 55 days annually for users of Route 132. In the year under study, heightened vigilance was needed only 15% of the days on an annual scale (Figure 24b) that has wide seasonal disparities (Figure 23 and Figure 24). The Ministère des Transports du Québec could implement different risk mitigation measures targeted for the weather conditions forecast by the weather models.

Figure 25. Rockfall that occurred 16 April 2019 obstructing Route 132. © Philippe Langlais, TVA Nouvelles

While RAINY conditions do not stand out in this study for causing high frequency and/or magnitude rock instabilities, rain events should be given special attention. Our methodology did not make it possible to clearly encompass all rain events on an annual scale. Given that HEAVY RF conditions are associated with extreme frequency high magnitude events, moderate intensity rain events must also feed back into frequencies and magnitudes of concern for the safety of Route 132 users. The same reasoning applies to the AUT. FT period. Had it been possible to better monitor fall freeze-thaw cycles, they would likely have shown a frequency of associated rock instabilities more similar to that of winter freeze-thaw cycles (WIN. FT).

This study highlights that rockfall dynamic is strongly controlled by the weather conditions and by the thermal regime of the rock slopes. Some of these conditions are associated with rockwall stability while others significantly increase rockfall frequency and/or magnitude (Figure 22, Figure 23 and Figure 24). Because of the inconsistency of weather conditions in term of duration (e.g. a cold winter period versus a winter thaw), we propose to focus on an event-based monitoring approach rather than a period-based approach to survey rockfalls. This approach allows to differentiate the respective impacts of different

meteorological events that cannot be easily distinguished on a periodic scale since their occurrences overlap. For an equivalent number of surveys and therefore for the same effort, this event-based monitoring approach is more relevant to identify weather conditions conducive to rockfalls of different magnitudes.

2.8 CONCLUSION

The influence of weather conditions on the occurrence of rock instabilities is now widely recognized in the scientific community. This study proposed to quantify rockfall volumes using LiDAR during previously selected weather conditions rather than taking regular surveys (weekly, monthly, seasonal). For an equivalent number of surveys and therefore for the same effort, this protocol made it possible to efficiently monitor the influence of weather conditions on rockfall frequency and magnitude. Over 18 months, 17 surveys were carried out on three rockwalls with a total area of 12,056 m^2. They made it possible to monitor a range of weather conditions and identify 1,287 rockfalls. The rockwall erosion rate during that period was 2.8–5.4 $mm \cdot y^{-1}$, which is among the highest in the world but comparable to other observations in this type of lithology (e.g. André, 1997; Barsch, 1977; Beylich, 2000; Curry and Morris, 2004; Hinchliffe and Ballantyne, 1999; Höllerman, 1983; Humlum, 2000; Olyphant, 1983; Sass, 1998).

Some of the weather conditions are associated with periods of rockwall stability (dry summer and cold winter periods) while others significantly increase rockfall frequency and/or magnitude (winter freeze-thaw cycles, spring thaw, high intensity rainfall). Winter freeze-thaw cycles and moderate rainfall lead to a increase in the frequency of low magnitude rock instabilities. High intensity rainfall and spring thaw coincide with a significant increase in the frequency of large dimension rockfall. In the realm of rockfall prevention, this study showed the importance of quantifying rockfall magnitude since the relationship between weather conditions and rockfall frequency is not necessarily applicable to rockfall magnitude. The results allow weather conditions to be categorized by their ability to trigger rock

instabilities of varying magnitudes. Using this combined with current or forecast weather conditions, different risk mitigation measures to limit safety hazards can be implemented.

2.9 APPENDICES

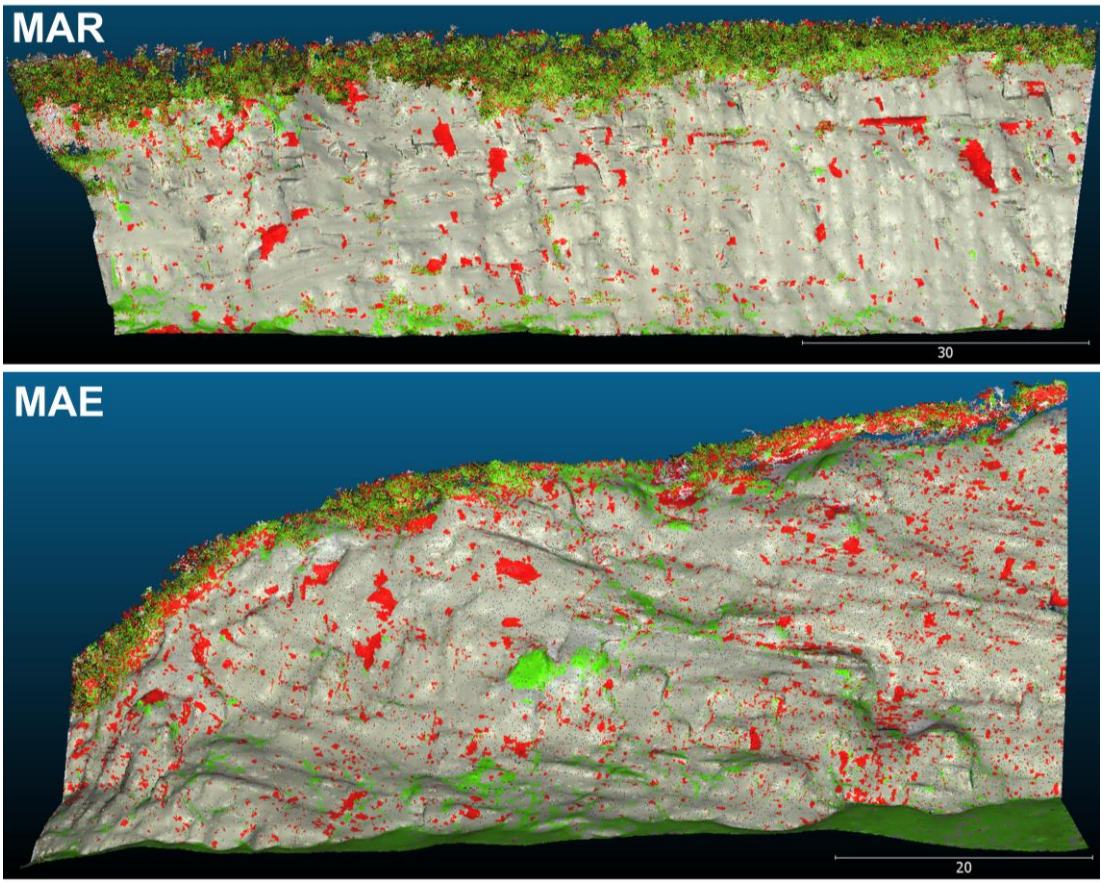

Figure 26. Point cloud of main changes between the first (14 June 2019) and last (18 December 2020) scan surveys of MAR and MAE sites. Red points show negative changes; green points show positive changes.

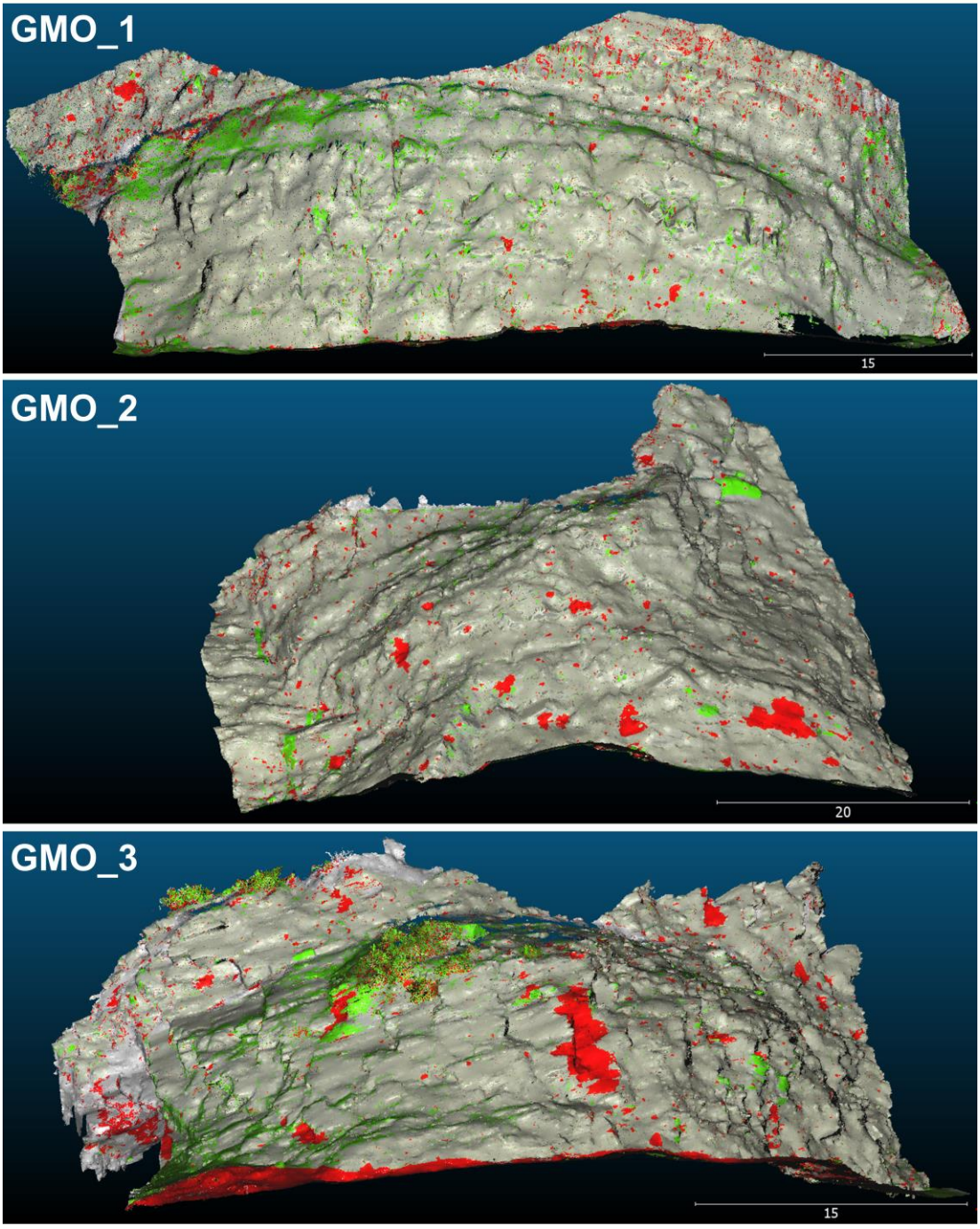

Figure 27. Point cloud of main changes between the first (14 June 2019) and last (18 December 2020) scan surveys of three GMO sites. Red points show negative changes; green points show positive changes.

2.10 DATA AND CODE AVAILABILITY

All the data collected during this study are available on request. Codes were only used to realize the Figure 21 and can also be send on request.

2.11 AUTHOR CONTRIBUTION

Tom Birien made the field work, developed the data processing, carried out the data analysis and wrote the manuscript. Francis Gauthier helped to develop the initial idea and to prepare the manuscript.

2.12 COMPETING INTERESTS

The authors declare that they have no conflict of interest.

2.13 ACKNOWLEDGMENTS

We thank the ministère des Transports du Québec (MTQ) as well the Natural Sciences and Engineering Research Council of Canada (NSERC) for funding this research. We acknowledge the LGGRM members who help us with the instrumentation process of the study sites, the maintenance, and data collection. We also would like to thank the anonymous referees of Natural Hazards and Earth System Sciences for valuable comments that improved the quality of the paper.

CHAPITRE 3

INFLUENCE DU RÉCHAUFFEMENT CLIMATIQUE CONTEMPORAIN SUR L'ALTÉRATION PAR LE GEL ET L'ÉROSION DES PAROIS ROCHEUSES

3.1 RÉSUMÉ

La distribution du gel et du dégel dans les massifs rocheux contrôle l'efficacité du processus de cryoclastie à différentes profondeurs en fonction de la période de l'année. Ce processus contribue grandement au développement des chutes de pierres. En modifiant le régime thermique des parois rocheuses, le réchauffement climatique du 21ème siècle pourrait entraîner des répercussions majeures sur la dynamique des instabilités rocheuses. Cette étude cherche à mieux comprendre l'influence de ce réchauffement sur i) la distribution du gel et du dégel dans les massifs rocheux, ii) sur l'efficacité de la fracturation de la roche par le gel et iii) sur l'évolution de la fréquence et de la magnitude des chutes de pierres. Une instrumentation conséquente déployée sur une paroi rocheuse du nord de la Gaspésie a permis de calculer son bilan d'énergie en surface, de mesurer et de modéliser son régime thermique en profondeur pendant une période de 28 mois. Des données de température de l'air historiques enregistrées localement et des données futures issues de simulations (scénarios RCP4.5 et RCP8.5), ont permis d'étendre la modélisation du régime thermique de la paroi rocheuse entre 1950 et 2100. Le modèle thermomécanique développé par Rempel a été utilisé pour quantifier l'efficacité de la fracturation par le gel pendant cette période de 150 ans. Selon les scénarios, un réchauffement de 3.3°C à 6.2°C est attendu dans le nord de la Gaspésie d'ici la fin du 21ème siècle. Ce réchauffement rapide devrait se répercuter par une diminution d'un à deux mètres de la profondeur maximale atteinte par le front de gel saisonnier et par un raccourcissement de sa durée d'un à trois mois. La fréquence des cycles gel-dégel sporadiques pourrait être multipliée par 12 en janvier. L'efficacité de la fracturation par le gel devrait s'intensifier autour de 70 cm de profondeur et s'estomper au-delà (RCP4.5) ou bien diminuer dès 10 cm de profondeur (RCP8.5). Dans cette région soumise à des cycles gel-dégel saisonniers, la fréquence des chutes de pierres de faible magnitude pourrait

s'accroître considérablement en hiver mais être largement réduite à l'automne et au printemps. Les processus associés au gel-dégel ne contribueront plus au développement d'instabilités de plus grande magnitude.

Mots-clés *:* Réchauffement climatique, Cycle gel-dégel, Cryoclastie, Chutes de pierres.

Contribution des auteurs :

Dans l'élaboration de ce chapitre, j'ai contribué à l'essentiel de la recherche sur l'état de la question, au développement de la méthode, au traitement des données et à la rédaction de l'article. Le professeur Francis Gauthier a participé au processus de réflexion et de développement de l'approche méthodologique ainsi qu'à la révision de ce chapitre et Francis Meloche a contribué à l'élaboration des simulations thermomécaniques.

3.2 INFLUENCE OF GLOBAL WARMING ON FROST WEATHERING AND EROSION OF ROCKWALL

Tom Birien[a], Francis Gauthier[a], Francis Meloche[a].

[a] *Département de biologie, géographie, chimie, Centre for Northern Studies (CEN), Université du Québec à Rimouski, Rimouski, Québec, Canada*

Abstract: The distribution of freezing and thawing within rock masses controls the effectiveness of the frost weathering process at different depths depending on the time of year. These processes are major contributors to the development of rock instabilities. By altering the thermal regime of rockwalls, global warming could have a major impact on rockfall dynamics by the end of the 21st century. This study seeks to improve our understanding of the influence of this warming on i) the distribution of freezing and thawing within rock masses, ii) the effectiveness of frost weathering and iii) the frequency and magnitude of rockfall. An instrument array installed on a rockwall on the northern Gaspé

Peninsula was used to calculate its surface energy balance and measure and model its thermal regime at depth over a period of 28 months. Combining locally recorded historical air temperature data with simulated future data (scenarios RCP4.5 and RCP8.5) made it possible to extend the rockwall thermal regime model over the period 1950 to 2100. The thermomechanical model developed by Rempel was used to quantify the effectiveness of frost weathering over this 150-year period. Depending on the scenario, warming of 3.3°C to 6.2°C is expected on the northern Gaspé Peninsula by the end of the 21st century. This rapid warming is likely to decrease the maximum depth of the seasonal freezing front by one to two metres and shorten its duration by one to three months. The frequency of sporadic freeze-thaw cycles could increase twelvefold in January. Frost weathering effectiveness should intensify around 70 cm in depth and disappear beyond that (RCP4.5) or diminish starting at 10 cm in depth (RCP8.5). In this region subject to seasonal freeze-thaw cycles, small magnitude rockfall frequency could grow considerably in winter but be significantly reduced in fall and spring. Furthermore, frost weathering would cease contributing to the development of larger magnitude instabilities.

Keywords: global warming, freeze-thaw cycle, frost weathering, frost damage, rockfall

3.3 INTRODUCTION

Through perturbation to the precipitation and temperature regimes, climate change has significant impacts on hillslope dynamics and processes (Crosta and Clague, 2009; Crozier, 2010; Gariano and Guzzetti, 2016; Huggel et al., 2012; Keiler et al., 2010; Korup et al., 2012; Sidle and Ochiai, 2006). However, how these perturbations interact with the occurrence, frequency and magnitude of slope movements remains challenging to understand (Alvioli et al., 2018; Gariano and Guzzetti, 2016; Huggel et al., 2012). The influence of climate change on those movements is a function of the material, type of movement and the initial and new climatic conditions (Crozier, 2010).

Rockfall, while spontaneous, results from a series of processes that interact over long periods. It never results solely from the latest apparent change (Draebing and Krautblatter, 2019; Gunzburger et al., 2005; Schovanec, 2020). The two principal weather factors contributing to the development of rock instabilities in hillslope and mountain environments are precipitations and freeze-thaw cycles (e.g. Birien and Gauthier, 2022; Collins and Stock, 2016; Coutard and Francou, 1989; D'Amato et al., 2016; Delonca et al., 2014; Hungr et al., 1999; Matsuoka and Sakai, 1999; Rapp, 1960; Wieczorek and Jäger, 1996). While the influence of climate change on precipitation regimes is highly variable on the global scale, rising air temperatures affect the entire planet and are particularly significant at high latitudes and altitudes (Hartmann et al., 2013). Global warming alters the distribution of freezing and thawing within rock masses and, by extension, the effectiveness of the frost weathering process (Rode et al., 2016). The repercussions of these changes are already apparent in the frequency of rockfalls of varying magnitudes in alpine periglacial environment (e.g. Gobiet et al., 2014; Gruber et al., 2004; Gruber and Haeberli, 2007; Harris et al., 2009; Hartmeyer et al., 2020; Huggel, 2009; Huggel et al., 2012; Paranunzio et al., 2016; Ravanel and Deline, 2011).

Modern climate warming is only in its infancy (Collins et al., 2013; Hartmann et al., 2013) and the already considerable impact of global warming on rockfall dynamics (e.g. Hartmeyer et al., 2020; Ravanel and Deline, 2011b) can make human populations and infrastructure more vulnerable (Haque et al., 2019; Mourey et al., 2022; Mourey et al., 2020; Pröbstl-Haider et al., 2021). The intensification of climate warming expected over the coming decades (Collins et al., 2013) raises a number of questions. To what extent will climate warming in the 21st century alter the distribution of freezing and thawing within rock? What repercussions on the effectiveness of frost weathering can be expected? What will be the impact on rockwall dynamics and on rockfall frequency and magnitude in particular?

Most studies on the impacts of climate warming on rockfall dynamics between the present and the end of the 21st century are qualitative and speculative in nature (e.g. Gruber et al., 2004a; Huggel, 2009; Ravanel and Deline, 2011). The development of some models

that allow to calculate the surface and near-surface temperature of rock slopes using meteorological data as input (Schnepfleitner et al., 2018) can be used to quantify the effects of future global warming on rock slopes affected by permafrost or dominated by seasonal frost or sporadic FT cycles. Noetzli et al. (2007), who modeled high mountain permafrost distribution 100 and 200 years in the future, assumed surface warming of 2.5°C to 3.5°C, depending on slope aspect. They showed that even if permafrost degradation could occur in few decades near the rock mass surface, relict permafrost could persist at greater depth for centuries. Rode et al. (2016) compared periods favorable to frost weathering in the Austrian Alps in 2010 and 2100. They showed that by the end of the 21st century, such periods can be expected to dwindle at low elevations. In contrast, in high elevation permafrost zone, these periods are likely to be longer due to more frequent thaw periods and a higher availability of liquid water. The aim of this study, however, was neither to quantify the evolution of the effectiveness of frost weathering, nor to discuss the evolution of the frequency and magnitude of rock instabilities within the larger context of modern climate change. Several frost cracking models developed in the last decades (e.g. Anderson et al., 2013; Hales and Roering, 2007; Rempel et al., 2016; Walder and Hallet, 1985) could be used to simulate the evolution of the efficiency of frost weathering by the end of the 21st century.

In a literature review, Coe and Godt (2012) identified three major categories of approaches used to assess the effect of climate change on slope movements: long-term monitoring (e.g. Matsuoka, 2008), retrospective approaches (e.g. Draebing et al., 2022; Ravanel and Deline, 2011) and prospective approaches (e.g. Rode et al., 2016). For the purposes of this study, we combined the last two categories by modeling the thermal regime of a rockwall on the northern Gaspé Peninsula using a dataset comprised of air temperature data collected from 1950 to present along and simulated data from present to 2100. Based on this 150-year air temperature time series, our objectives are to analyse the climate warming influence on (1) the evolution of the freezing and thawing distribution within the rockwall , (2) to quantify the effectiveness of frost damage over time and at different depths. and (3) to assess the effects of climate warming on the frequency and magnitude of rock instabilities in environments subject to freeze-thaw cycles.

3.4 STUDY AREA

This study was carried in northern Gaspésie (Figure 28), where the continental extent of the Appalachian fold and thrust belt, the Chic-Choc mountains, meets the Gulf of St. Lawrence (Hétu and Gray, 2000). The local relief is dominated by glacial valleys (Hétu and Gray, 1985) that separate rocky plateaus reaching 400 to 600 m in altitude. The junction between these plateaus and the Gulf of St. Lawrence is marked by rock walls. Cut into Ordovician flysch, these rockwalls are mainly composed of alternating strata of sandstone, greywacke, siltstone and pelagic shale of multi-decimeter thickness (Enos, 1969a, 1969b). These rocks are highly fissile and promote a high density of rock discontinuities (Hétu and Vandelac, 1989). They show a high retreat rate (3 mm·a-1) and high frequency of rockfall (1 per 13 $m^2 \cdot a^{-1}$) (CHAPITRE 2). Most rock slopes are facing north, which limits the influence of solar radiation on rock temperature. They are in constant shade from mid-October to mid-March and become exposed again to the late afternoon sun in spring (Birien and Gauthier, 2022).

The area is characterized by a humid continental climate with short cool summers, according to the Köppen climate classification system (Beck et al., 2018). Weather data for the period 1991–2020 from Cap-Madeleine weather station (49°15'03.0"N 65°19'29.0"W) (Figure 28), show that it has an annual mean temperature of 3.9°C and warmest (July) and coldest (January) month mean temperatures of 16.3°C and -9.2°C, respectively. Over this 30-year period, it received a total annual precipitation of 888 mm, 33% of which fell as snow (Environnement Canada, 2021).

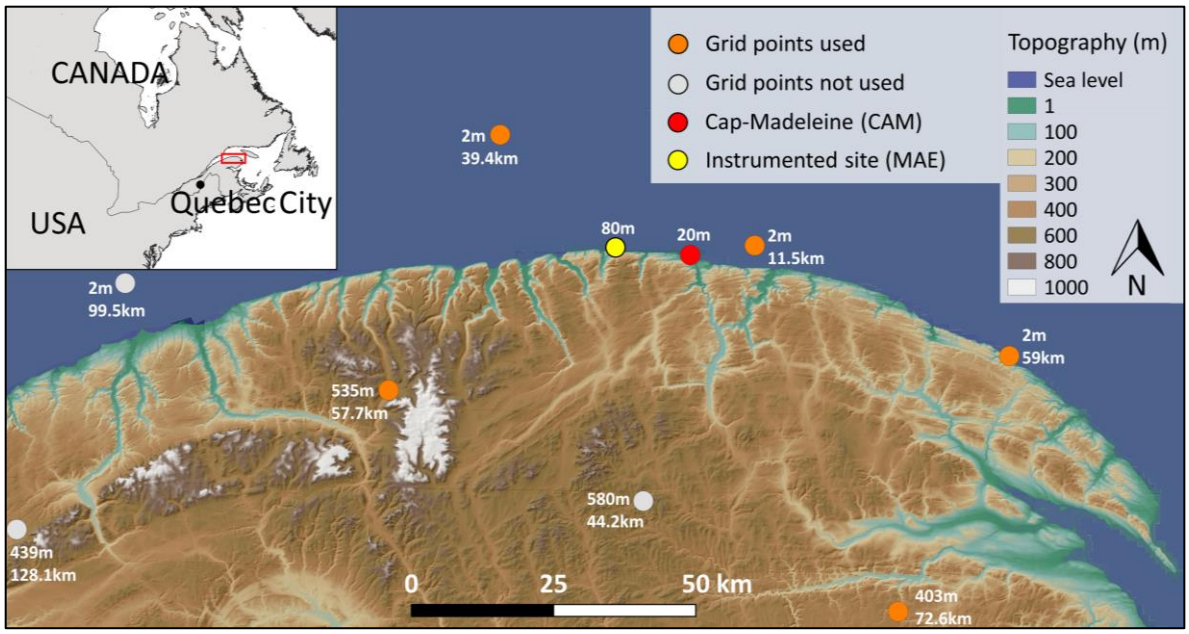

Figure 28. Location map showing the Environment Canada weather station at Cap-Madeleine (red dot), the instrumented rockwall with weather station and temperature logger (yellow dot) and the NAM-44 grid points (orange dots) used for climate projection. Altitude is given for each grid point, like the distance between these points and the weather station of Cap-Madeleine.

3.5 METHODS

A time series of air temperatures from 1 January 1950 to 31 December 2099 was constructed using locally recorded historical data (1950-2020) and simulated data (2021-2099). This time series was then used to model the thermal regime of a rockwall, which was previously calibrated with temperatures measured at varying depths between 10 June 2018 and 8 October 2020 (Site MAE, Figure 28). Based on this thermal regime model, the evolution of the freeze-thaw characteristics and the frost cracking intensity within the rockwall were analyzed and compared for typical 30-year climatic normal periods: 1950–1979, 1980–2009, 2010–2039, 2040–2069 and 2070–2099 (Figure 29).

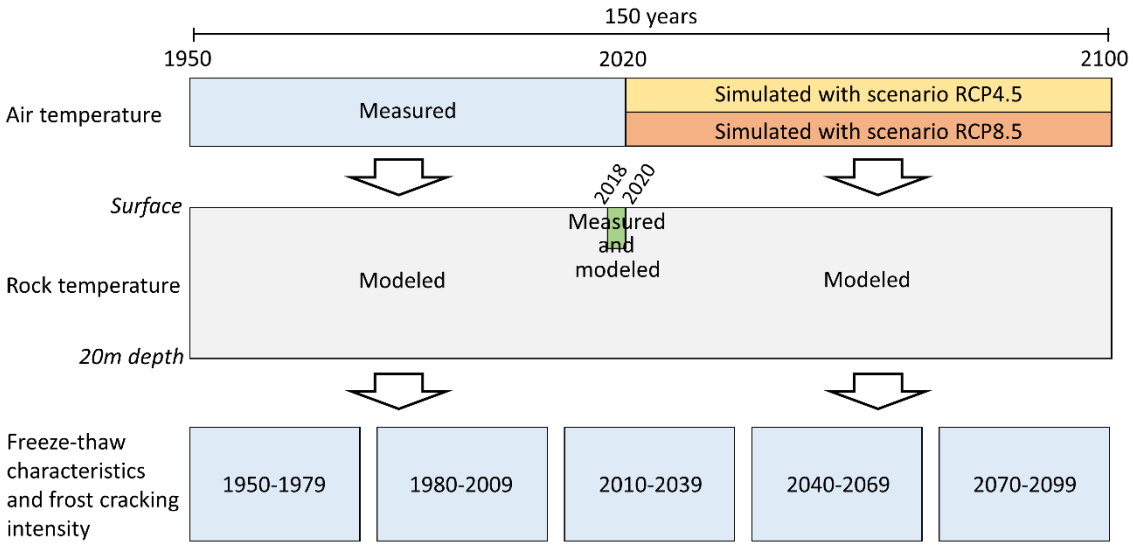

Figure 29. Summary of methodological steps used to analyze the influence of global warming on rockwall thermal regime and frost weathering.

3.5.1 Air temperature datasets

The historical data (1950-2020) comes from hourly air temperature collected at the Environment Canada weather station at Cap-Madeleine (Figure 28). Five simulated daily air temperature time series (1970-2100) were extracted from three Regional Climate Models (RCMs) driven by three Coupled Global Climate Models (GCMs) (Table 3). These five simulations, characterized by a 0.44° grid mesh (around a 50 km grid resolution), were obtained from the North America Coordinated Regional Climate Downscaling Experiment (CORDEX-NA) project (Mearns et al., 2017). The simulations were done under moderate (RCP4.5) and high (RCP8.5) Representative Concentration Pathways (RCPs). We selected RCP4.5 and RCP8.5 as they represent middle- and worst-case climate change scenarios (van Vuuren et al., 2011).

Table 3. The five simulations used in this study from Regional Climate Models (RCMs) driven by different Coupled Global Climate Models (GCMs). The simulations used two Representative Concentration Pathways (RCP4.5 and RCP8.5). This North American climate data was obtained from the NA-CORDEX database (Mearns et al., 2017).

Regional Climate Models	Driven conditions from Coupled Global Climate	Institutions for cGCMs
HIRHAM Christensen et al., 2007	ICHEC-EC-EARTH	Irish Centre for High End Computing (ICHEC), Ireland
CRCM5 Martynov et al., 2013; Šeparović et al., 2013; Zadra et al., 2008	CCCma-CanESM2 MPI-M-MPI-ESM	Canadian Centre for Climate Modelling and Analysis (CCCma), Canada Max Planck Institut (MPI), Germany
RCA4 Samuelsson et al., 2011	CCCma-CanESM2 ICHEC-EC-EARTH	Canadian Centre for Climate Modelling and Analysis (CCCma), Canada Irish Centre for High and Computing (ICHEC), Ireland

The 50 km resolution of the GCMs data need to be downscaled for a better representativity of the temperature measured at the weather station (CAM). These measured temperatures were compared with simulated temperatures from the GCMs during a historical period (1970-1999) to support the grid points selection. A combination of five grid points has been chosen (Figure 28) according to the goodness-of-fit of the simulated mean temperature (from the five GCMs) on the measured temperature during this historical period. The grid points selection has also been guided by their respective distances from CAM, their elevation and their geographical location (maritime and continental influence). Then, air temperatures were simulated until 2100 using the same grid points of the five GCMs. The models output included the minimum, mean and maximum daily temperatures. Using linear interpolation between the minimum and maximum daily temperatures, we simulated hourly data for the future period to match the time scale of the historical period. At this point, the temperatures simulated with the five models were not averaged to avoid loss of information on climate extremes.

3.5.2 Meteorological and rockwall temperature datasets

A small weather station was installed at 20 m from the top of a 100 m high rockwall facing north (MAE) located 15 km west of Cap-Madeleine weather station (Figure 28). The weather station measures air temperature, incident and reflected solar radiation perpendicular to the rockwall and wind speed and direction. Atmospheric pressure and incident and reflected long wavelength radiation were recorded from another weather station located on the scree slope under the rockwall (Table 4). The rockwall temperature was measured with a thermistor string inserted into a borehole perpendicular to the surface. Thermistors were installed on the surface and at depths of 0.3, 0.6, 1.0, 1.5, 2.0, 2.5, 3.0, 3.5, 4.0, 4.5, 5.0 and 5.5 m. A continuous temperature profile of rock was produced using linear interpolation between the thermistors. The purpose of this instrumentation was to (1) calculate the energy balance at the rockwall surface and (2) measure its thermal regime up to 5.5 m in depth. The data collection period covered 28 months from 10 June 2018 to 8 October 2020. Readings were taken every 15 minutes and averaged to get hourly data.

Table 4. Instruments used to assess the energy balance at the rockwall surface and ii) measure its thermal regime from the surface to 5.5 m in depth.

Data	Unit	Instrument (Company)	Accuracy
Air temperature	°C	Air temperature sensor TMC6-HD + Solar radiation shield M-RSA (HOBO by Onset)	±0.25°C
Rock temperature	°C	Thermistor string 915 MHz + minilogger M-Log5W-DALLAS-US (Geoprecision)	±0.25°C
Incident Solar radiation Reflected Solar radiation	W/m²	Pyranometer S-LIB-M003 (HOBO by Onset)	±10 W/m²
Incident infrared radiation Reflected infrared radiation	W/m²	Pyrgeometer SN-500-SS (Apogee Instruments)	±8.5 W/m²
Wind and gust speed Wind direction	m/s Ø	Wind speed and direction sensor S-WSET-B (Onset)	± 1.1 m/s ± 5 degrees
Air pressure	mbar	Barometric pressure sensor S-BPB-CM50 (Onset)	±5.0 mbar

3.5.3 Rock temperature and frost damage modeling

Modeling surface thermal signal propagation to depth requires detailed knowledge of site lithology. Several intact sample blocks about 20 cm long were collected directly from the rockwall surface: 7 blocks of greywacke, 9 blocks of siltstone and 3 blocks of shale. Natural discontinuities in the rock masses, particularly in the stratified siltstone and shale blocks, made it possible to separate the samples without weakening them. At the Laboratoire de géomorphologie et de gestion des risques en montagne (LGGRM), the volume, dry mass and water saturated mass of each sample were measured to calculate their density and porosity (ISRM, 1979). The thermal properties of the samples were measured at the Laboratoire ouvert de géothermie (LOG) at the Institut National de la Recherche Scientifique Eau Terre Environnement Research Centre (INRS-ETE). The LGM Lippmann TCSCAN infrared scanner was used to measure the thermal conductivity and diffusivity of each sample (Lippmann and Rauen GbR, 2022). Since siltstone and shale are anisotropic rocks, thermal signals that are perpendicular or parallel to the bedding plane do not propagate at the same speed. The method developed by Popov *et al.* (2016) was used to calculate the average thermal conductivity and diffusivity values of the anisotropic samples. Thermal capacity of each sample was then calculated from the thermal density, conductivity and diffusivity values. In this way, average values of the thermal parameters for each type of rock were calculated from collection of samples.

WUFI® Pro, a software originally designed to calculate energy and moisture conditions in building walls, was used to model the rockwall temperature. It had previously been used to successfully model the thermal regime and moisture of rock masses (Rode et al., 2016; Sass, 2005; Schnepfleitner et al., 2018). The weather conditions measured at the rockwall surface between 10 June 2018 to 8 October 2020 (Table 4) and the physical (density, porosity) and rock thermal properties (conductivity, capacity and diffusivity) served as inputs to model the thermal regime of the rockwall. The modeled surface temperatures were then validated using measurements taken directly at the rockwall surface. Similarly, the propagation of the modeled thermal signal was calibrated using measured data by modulating

the thickness and nature (thermal properties) of the rock layers traversed. That combination of thickness and nature had to correspond to the geological units observed on the rockwall surfaces. Figure 30 summarizes the protocol used in this study. Although our instrumentation limited the temperature measurements to 5.5 m in depth, we modeled them to a depth of 20 m. At that depth, the year-to-year variability of surface temperatures is negligible, and only climate changes can influence the thermal regime (Lachenbruch et al., 1988). In the Alps, Sass (2005) modeled the degree of saturation in a rockwall that stabilized around 80% in the first decimetres below the surface. In the absence of local measurements, this average value was used on the entire modeled profile.

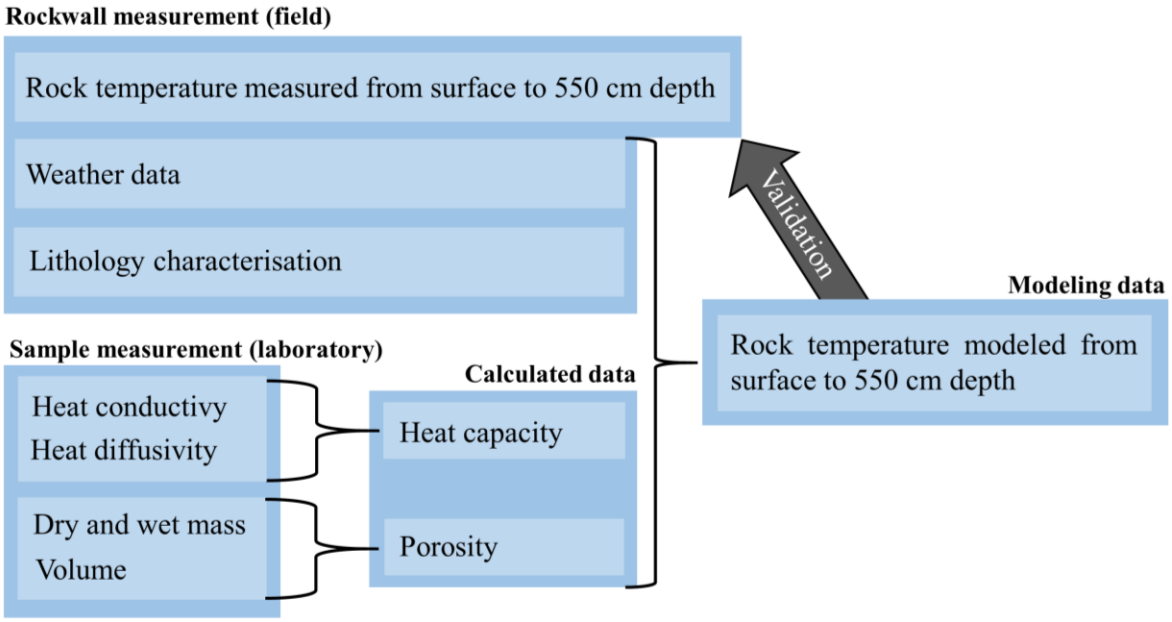

Figure 30. Data obtained from our field and laboratory measurements to model rock temperature in WUFI® Pro.

After the model was calibrated with the rockwall temperature measured between 1 June 2018 and 8 October 2020, it has been used to simulate the thermal regime between 1 January 1950 to 31 December 2099. The time series of air temperatures, constructed from historical and simulated data (Figure 29), was used as input in themodel. Given the context of global warming, a moving average of air temperature over the 30 years preceding the modeled year

was used to set the temperature at 20 m in depth. The values for short and long wavelength radiation, atmospheric pressure and wind speed and direction for the year 2019 were looped for each year of the covered period. Further studies should help to improve our ability to forecast the evolution of these parameters in the current climate change context (Collins et al., 2013; Hartmann et al., 2013). Furthermore, since the instrumented rockwall has a northerly exposure and remains in shadows from mid-October to mid-March, it is mostly affected by air temperature fluctuations in winter (Birien and Gauthier, 2022; Gauthier et al., 2015; Gauthier et al., 2013).

In order to quantify the global warming influence on the effectiveness of frost weathering, the thermomechanical model developed by Rempel et al. (2016) was used. The authors assume that porosity increases driven by the formation of ice lenses occurs parallel to the frost weathering front. Under conditions where frost cracking takes place, their model measures the porosity change in a rock slope over time and that change should be correlated with frost-driven rock damage. In our study we used the 150-year period of thermal regime simulated to drive this thermomechanical model. For all depths affected by freezing temperatures during winter, we compared the total change of porosity over time. We used a fracture toughness (F_t) value of 0.345 MPa $m^{-1/2}$ as measured by Dwivedi et al. (2000) on a sandstone sample at 0°C with a porosity equal to that measured on the greywacke samples collected in the field. To simplify our analysis, we have chosen to use a constant value of F_t, even if over such long analysis periods, its value should normally decrease over time (Gauthier et al., 2022a; Gauthier et al., 2022b). Except for rock temperatures and fracture toughness, all other values proposed by Rempel et al. (2016) were preserved in the model.

3.5.4 Trend analyses

We analyzed the seasonal evolution of freezing and thawing distribution within the rockwall and the effectiveness of frost damage over typical 30-year climatic periods: 1950–1979, 1980–2009, 2010–2039, 2040–2069 and 2070–2099. Based on those periods, we

quantified the impact of climate warming on five parameters used as indicator of the intensity of cryogenic processes: 1) the duration between the earliest autumnal and the last spring FT cycle during a season, 2) the frequency of sporadic FT cycles between the earliest autumnal and the last spring FT cycle each season, 3) the duration and 4) the maximum depth of the seasonal freezing front, and 5) the intensity of frost damage (porosity change) at all depths affected by freezing temperatures into the rockwall (Figure 31).

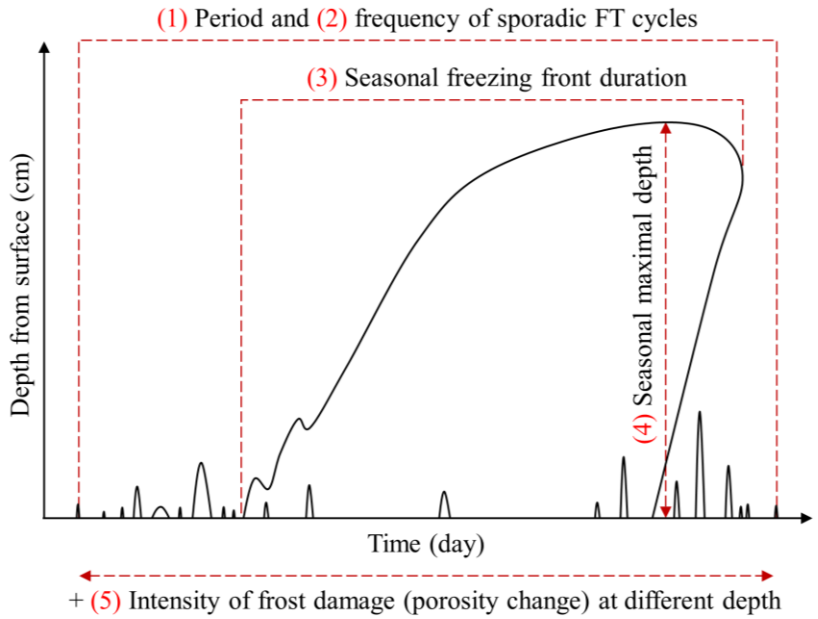

Figure 31. Diagram showing the rockwall parameters quantified for the five climatic periods. Continuous black lines represent occurrences of 0°C.

We defined a sporadic FT cycle as any cycle, irrespective of duration, that reaches a minimum depth of 10 cm. The seasonal freezing front is defined as the longest uninterrupted period of rockwall temperatures below the freezing point over a winter season. It is the only FT cycle that is not considered as a sporadic cycle during a season. By definition and as a rule, a threshold temperature of 0°C is considered as the freezing temperature of water in rock masses in different morphoclimatic environments (e.g. Fahey and Lefebure 1988, Coutard and Francou 1989, Gruber et al. 2004b, Noetzli et al. 2007, D'Amato et al. 2016,

Kromer et al. 2018). To maintain consistency with those studies, we used 0°C for counting sporadic FT cycles and quantifying the depth and duration of seasonal freezing front.

Averaging the air temperatures produced by the five models (Table 3) attenuate climate extremes and prevented meaningful quantification of the target parameters (Figure 31). To address this issue, rockwall thermal regime was simulated separately for each GCMs. The target parameters were then counted (e.g. frequency of sporadic FT cycles) or quantified (e.g. maximum depth of seasonal freezing front) for each simulation. Finally, an average of those parameters from all simulations were calculated.

3.6 RESULTS

3.6.1 Rock physical and thermal properties

The instrumented rockwall is made up of alternating strata of shale, siltstone and greywacke. The shale strata are on the order of centimetres in thickness, while the siltstone and greywacke strata thickness are more variable (decimeter to meter). The density, porosity, conductivity, diffusivity and thermal capacity values measured in laboratory from the study site samples are detailed in Table 5. All thermal property values shown in this table are for 80% of water saturation. The thermal regime of the first 20 metres of the rockwall has been modeled and the proportions of greywacke, siltstone and shale used as input in the model give average values of heat conductivity, thermal diffusivity and heat capacity of 3.52 W m^{-1} K^{-1}, 1.41e^{-06} m^2 s^{-1} and 964.12 J kg^{-1} K^{-1} respectively.

Table 5. Bulk density, porosity and thermal parameters measured in the laboratory for the three main types of rock characteristics of our study sites. Values of thermal parameters are for 80% water saturation.

Rock type	Bulk density (kg/m^3)	Porosity (%)	Heat conductivity (W/mK)	Thermal diffusivity (m^2/s)	Heat capacity (J/kgK)
Greywacke	2467	11.32	1.76	$5.89e^{-07}$	1379.24
Siltstone	2987	4.50	3.14	$1.24e^{-06}$	895.04
Shale	2574	3.88	3.93	$1.58e^{-06}$	980.06

3.6.2 1950-2100 air temperature trends

Averaging the temperature from several models is relevant to make sure that annual mean air temperature modeled fits the value measured. For the historical period used to downscale the modeled temperatures from the GCMs (1970-1999), the mean annual air temperature modeled was equal to 3.28°C and the value measured at Cap-Madeleine during this same period was equal to 3.30°C (Figure 32). Nevertheless, since they are averaged over five grid points of five simulations, the modeled data show less year-to-year variability than the Cap-Madeleine data (Figure 32).

On the northern Gaspé Peninsula, the measured annual mean air temperature was 3.42°C for the period 1950–1979, compared with 6.41°C modeled according to RCP4.5 and 8.72°C modeled according to RCP8.5 for the period 2070–2099 (Table 6). Over the 21st century, air temperature can be expected to rise on average by 0.33°C per decade considering RCP4.5 (+3.3°C) and by 0.62°C per decade considering RCP8.5 (+6.2°C). Climate warming should be more pronounced in winter (+0.4°C per decade with RCP4.5, +0.8°C with RCP8.5) than in summer (+0.2°C per decade with RCP4.5, +0.4°C with RCP8.5). Following the RCP8.5, the mean winter temperature should rise above the freezing point (+0.33°C) by the end of the 21st century.

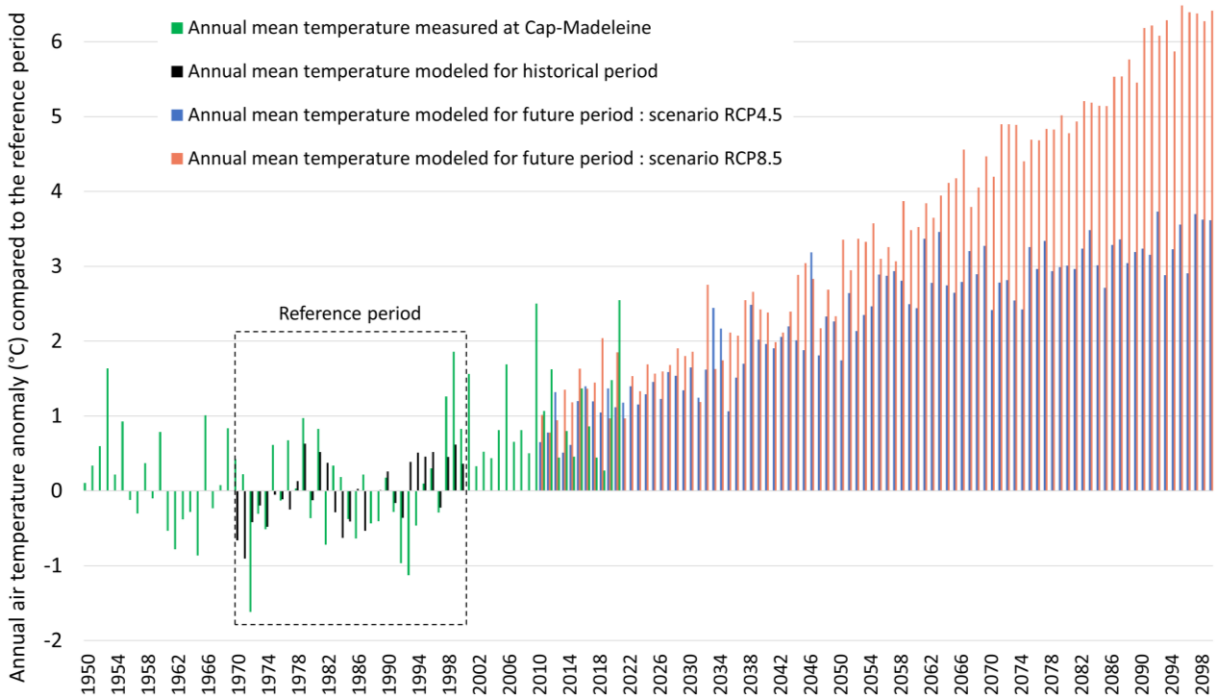

Figure 32. Mean annual air temperature anomalies measured at the weather station of Cap-Madeleine (green) and modeled (black) during the reference period and between 2010 and 2100 with scenario RCP4.5 (blue) and RCP8.5 (orange). The temperature of the reference period (1970-1999) is 3.3°C.

Table 6. Mean air temperature for the five consecutive 30-year periods from 1950 to 2100 for two representative concentration pathways (RCP4.5 and RCP8.5).

Period	RCP4.5	RCP8.5	
1950-1979	3.42		Temperature measured (Cap-Madeleine)
1980-2009	3.55		Temperature measured (Cap-Madeleine)
2010-2039	4.73	4.91	Temperature measured (Cap-Madeleine) and simulated from 2021
2040-2079	5.85	6.58	Temperature simulated
2070-2099	6.41	8.72	Temperature simulated

3.6.3 Rockwall contemporary thermal regime

From 10 June 2018 to 8 October 2020, the modeled thermal regime is consistent with the measurements recorded in the rockwall (Figure 33). The coefficient of determination of the surface temperature is very high (R^2=0.986) and rises further with depth (R^2=0.996 at 0.3 m) as temperature variability decreases. The thermal regime measurements show that the annual temperature amplitude in the rock decreases rapidly with depth (Figure 33): 45°C at the surface, 34°C at 0.3 m, 22°C at 1.0 m and only 6°C at 5.5 m. Modeled amplitude is similar to measured amplitude.

The general characteristics of the seasonal distribution of freezing and thawing in the rockwall are equally apparent in the measured and the modeled data (Figure 33). In winter 2018–2019, the modeled period of occurrence of freezing was 4 days longer (194 days) than the measured period (190 days). The modeled seasonal freezing front was 6 days shorter (127 days) and the modeled maximum depth was lower by 7 cm (404 cm). In winter 2019–2020, the modeled period of occurrence of freezing was identical in duration to the measured period

(173 days), the modeled seasonal freezing front was two days shorter (141 days) and the modeled maximum depth was greater by 7 cm (360 cm). During the winter 2019–2020, the number of measured and modeled FT cycles reaching the surface (36 vs. 34), 10 cm depth (23 vs. 21) and 50 cm depth (7 vs. 5) were also similar (Figure 33). Because the surface thermistor was over isolated with insulating foam during the previous winter (by mistake), less sporadic FT cycles were probably recorded that it really occurred during the winter 2018-2019. At the onset of these winters (2019, 2020), major surface thaws have resulted in a brief interruption in the freezing front in depth. Most sporadic FT cycles occurred in April (Figure 33) as the intensity of solar radiation rose (Birien and Gauthier, 2022).

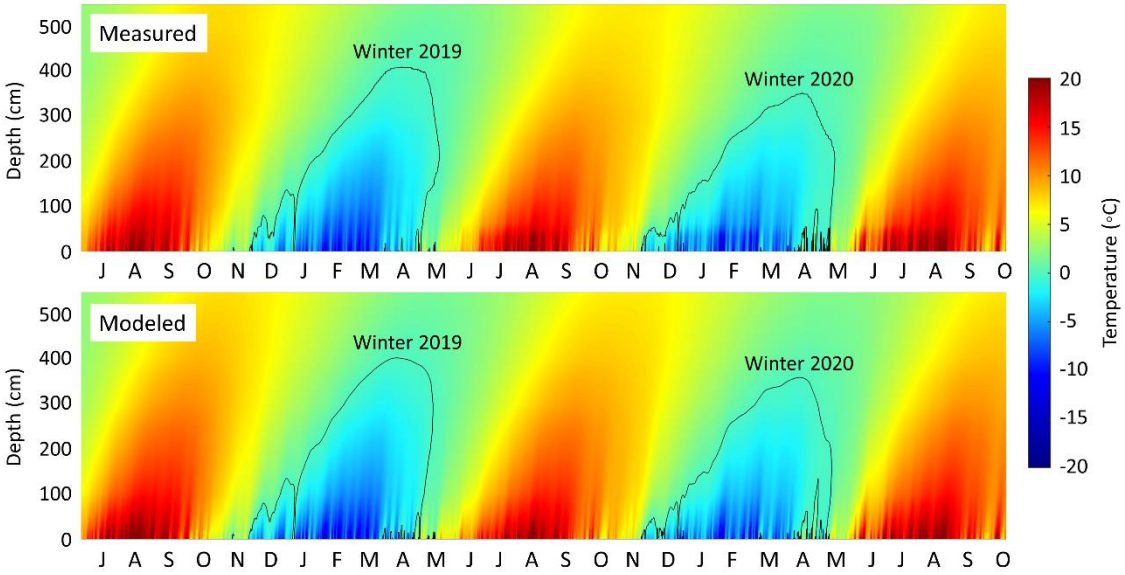

Figure 33. Measured and modeled thermal regime perpendicular to the surface of a flysch rockwall, 0 to 550 cm in depth. Continuous black lines represent occurrences of 0°C in the rockwall.

3.6.4 Freeze-thaw and frost damage indicator trends

According to the simulation results, modern climate change can be expected to have a significant influence on the period of occurrence and the maximum depth of the seasonal freezing front. According to RCP4.5, the duration of the seasonal freezing front would

decrease by 47 days between the periods of 1950-1979 (148 days) and 2070-2099 (101 days). According to RCP8.5, the seasonal freezing front would only persist for 39 days in the period 2070–2099 (Figure 34). The maximum winter depth would decrease from 4.10 m in the period 1950–1979 to 3.13 m in 2010–2039 and 2.13 m in 2070–2099 considering RCP4.5. The drop is even more pronounced considering RCP8.5: the seasonal freezing front would reach a depth of 3.01 m during the period 2010–2039 and just 1.05 m in 2070–2099 (Figure 34).

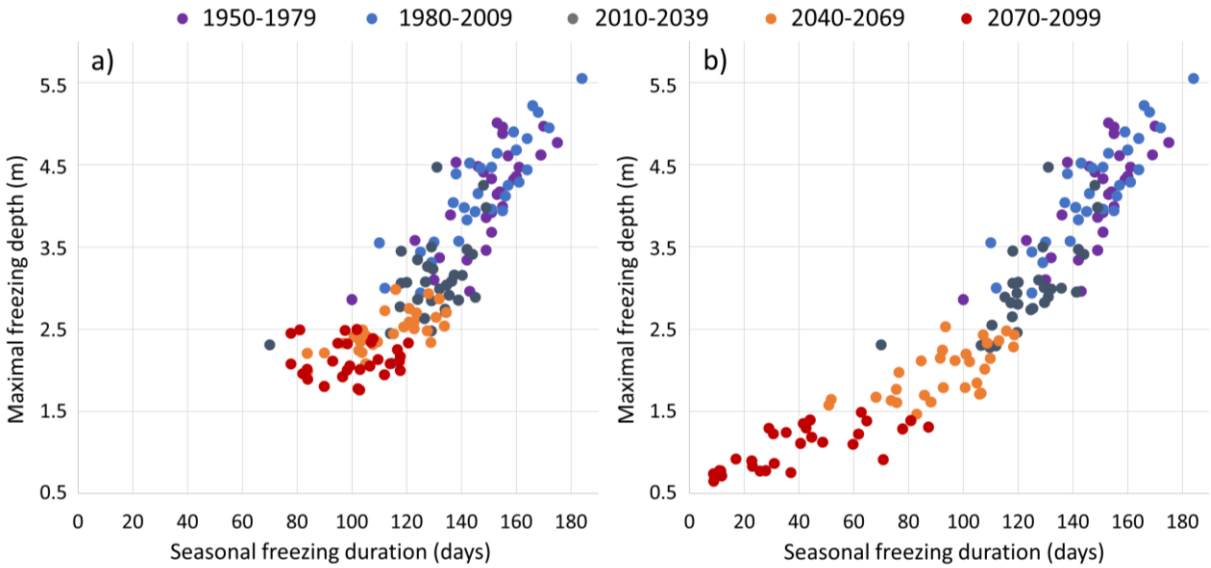

Figure 34. Duration and maximum depth of the seasonal freezing front, winters 1950 to 2100. From 1950 to 2020, the models used the air temperature measured at Cap-Madeleine. From 2021 onward, simulated temperatures from scenarios a) RCP4.5 and b) RCP8.5 were used.

It is expected that global warming will be accompanied by a change in the period of occurrence of sporadic FT cycles. For the period 1950–1979, those cycles were concentrated in fall (7.3 a^{-1} on average in November) and spring (8.2 a^{-1} in April) while they were rare in winter (0.5 a^{-1} in January and 0.8 a^{-1} in February) (Figure 35). By the end of the 21st century, winter can be expected to become the period with the highest number of sporadic FT cycles. They could become 2.4, 4.8, 2.9 and 1.5 times more frequent in December, January, February

and March, respectively according to RCP4.5 (Figure 35a) and 2.2, 12.1, 7.7 and 2.0 times more frequent according to RCP8.5 (Figure 35b). Conversely, the previously highly eventful months of November and April can be expected to become periods with a low occurrence of sporadic cycles. Their frequency could be divided by 3 in November and by 1.6 in April considering RCP4.5 (Figure 35a). According to RCP8.5, they should become 11.8 and 4.6 less frequent in November and April, respectively (Figure 35a). The disappearance of October and May FT cycles in the late 21st century are indicative of a shorter freezing period.

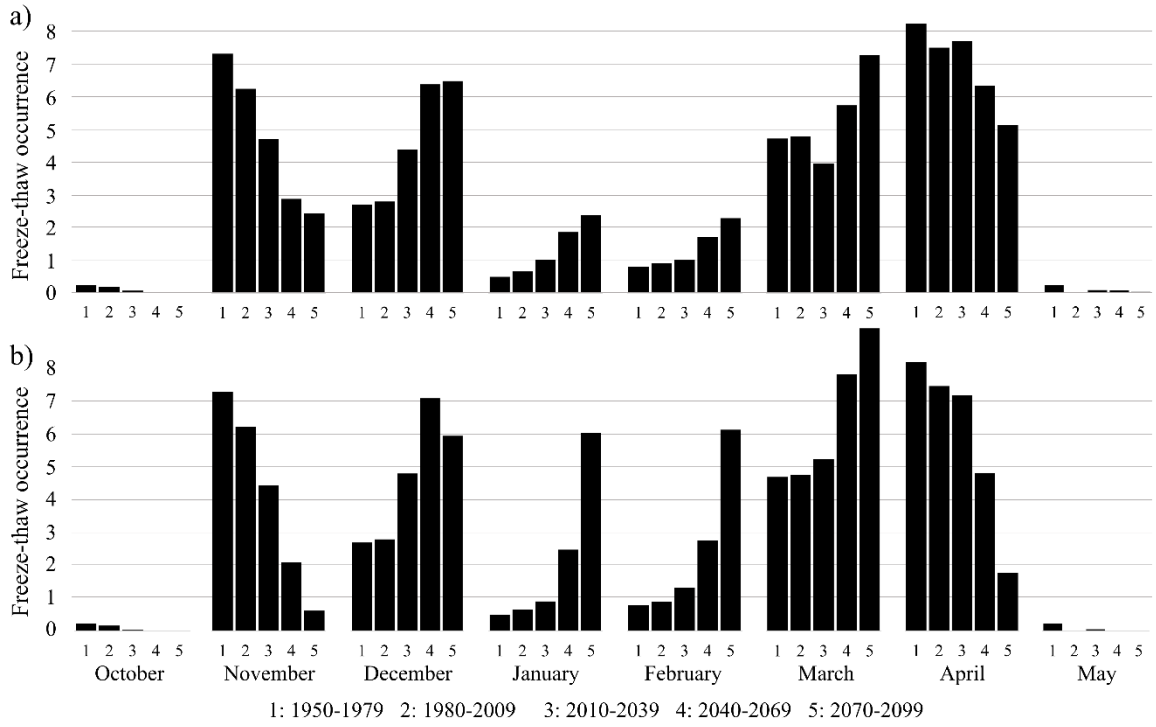

Figure 35. Mean monthly occurrence of sporadic FT cycle during five 30-years periods from 1950 to 2099. The two first periods (1950–1979 and 1980–2009) were built with measured air temperature data whereas the three last ones were partially (2010–2039) or fully (2040–2069, 2070–2099) built with simulated air temperature data from a) RCP4.5 and b) RCP8.5.

Between 1950 and 2099, an inverse relationship can be observed between the sporadic FT cycle frequency during the whole period of FT occurrence and the maximum depth of the seasonal freezing front (Figure 36a). In general terms, the more the climate warms, the more

the maximum depth of the freezing front can be expected to decrease (Figure 36b) and the frequency of sporadic FT cycles can be expected to increase (Figure 36c). During the 150-year study period, the maximum depth of the seasonal freezing front is expected to decrease from 4.15 m to 2.13 m according to RCP4.5 and from 4.15 m to 1.05 m according to RCP8.5 (Figure 36b). The frequency of sporadic FT cycles did not increase between the periods 1950–1979 and 1980–2009, in fact, it decreased slightly (0.14 vs. 0.13 cycles d^{-1}). In contrast, between the periods 1980–2009 and 2070–2099, this frequency increase by 1.3 considering RCP4.5 and by 1.7 considering RCP8.5 (Figure 36c). Global warming also appears to result in a lower FT cycle frequency at greater depth (Figure 36c).

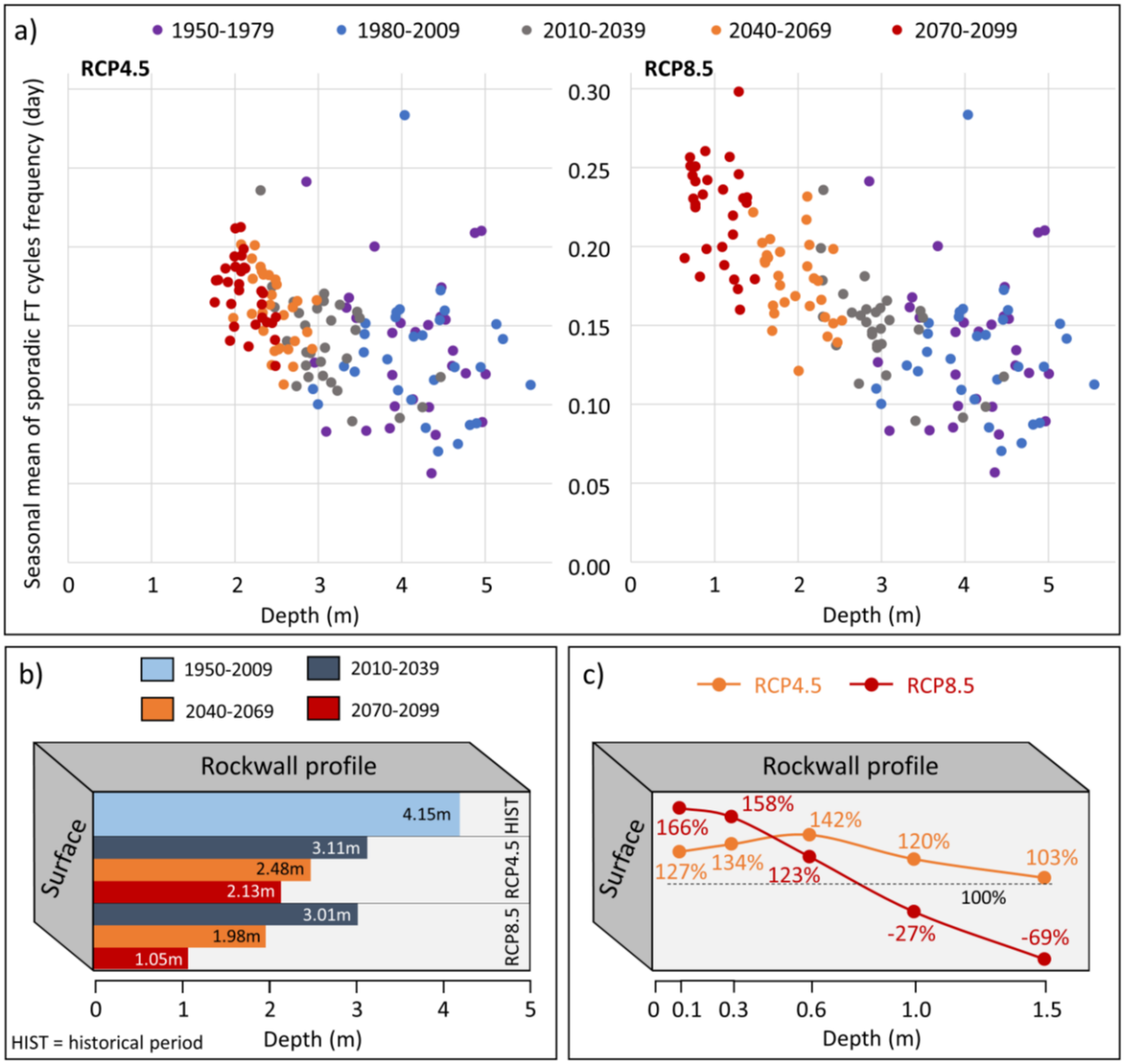

Figure 36. a) Relationship between seasonal mean of sporadic FT cycle frequency and the maximum depth of the seasonal FT cycle, 1950 to 2100. b) Mean maximum freezing front depth during the historical period and for future periods according to RCP4.5 and RCP8.5, c) Relative FT cycle frequency at different depths for the period 2070–2099 compared to the historical period (1950–2009) according to RCP4.5 and RCP8.5. Data from 1950 to 2020 were built with measured air temperature data whereas data from 2021 to 2099 were built with simulated air temperature data from RCP4.5 and RCP8.5.

For the periods 1950–1979 and 1980–2009, increased porosity caused by the formation of segregated ice had an impact on the rock to a depth of 3.5 m. The formation of ice lenses caused damage at four preferential depths: at the surface, and around 0.7 m, 1.3 m and 2.7 m (Figure 37). The period 2010–2039 is expected to experience climate warming of over one degree Celsius compared to the two previous 30-year periods (Table 6). This warming would be enough to prevent ice lenses from forming deeper than 2.7 m (Figure 37). The following period (2040–2069) is expected to be marked by increased frost damage around 0.7 m in depth compared to historical periods and by decreased damage at greater depths (Figure 37). While this trend continues during the period 2070–2099 according to RCP4.5 (Figure 37a), effectiveness of frost cracking is predicted to decrease starting at 10 cm in depth considering RCP8.5 (Figure 37b). Climate warming could result in an increase in frost damage around 0.7 m in depth and a significant decrease past that depth. At the surface, frost cracking effectiveness is likely to remain as significant in the 2070–2099 period as in the historical periods (Figure 37).

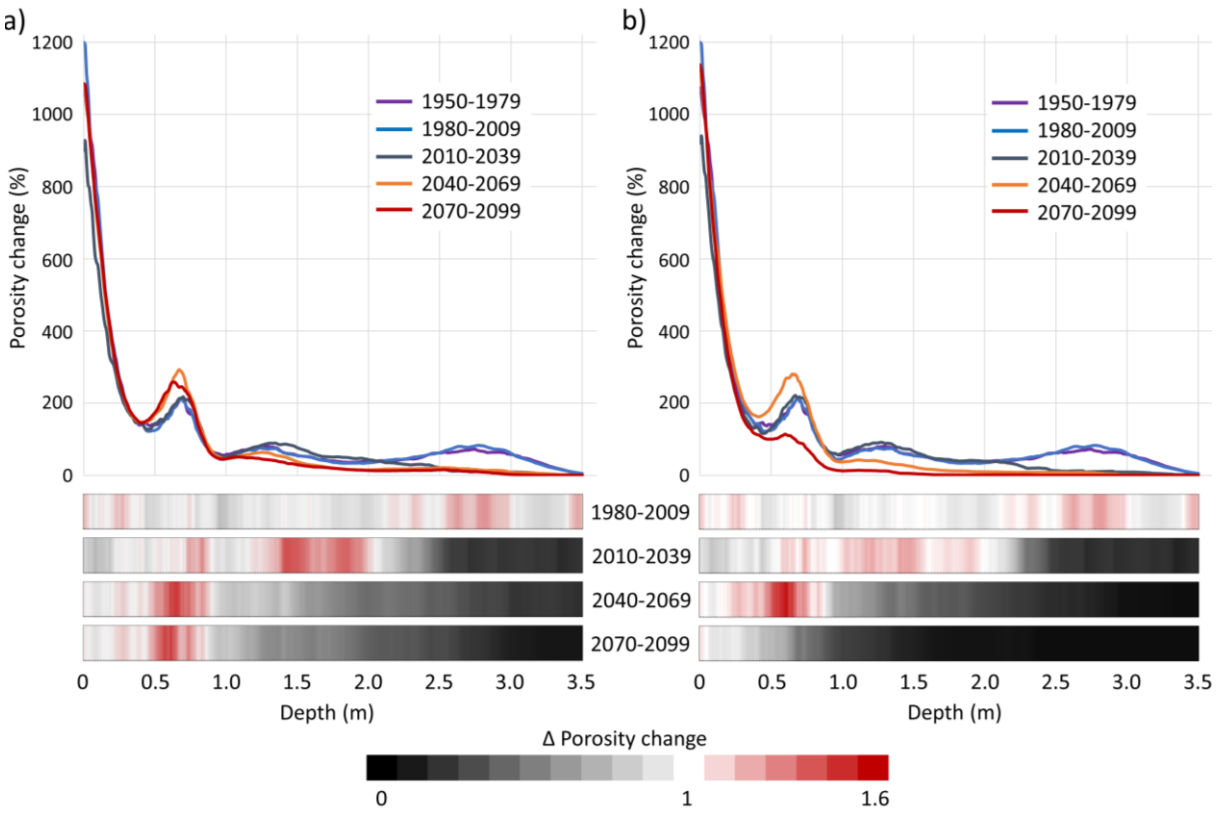

Figure 37. Simulations of total change in porosity based on simulated rock temperatures for the five consecutive 30-year periods from 1950 to 2099 according to a) RCP4.5 and b) RCP8.5. The bars below the graphs represent the porosity change during the periods 1980–2009, 2010–2039, 2040–2069 and 2070–2099 compared to the period 1950–1979.

3.7 DISCUSSION

3.7.1 Effect of global warming on rockfall frequency and magnitude

The influence of global warming on frost distribution has been studied during a 150-year period (1950-2100) using the RCP4.5 and RCP8.5 greenhouse gases concentration pathways. Depending on the scenario, warming of 3.3°C to 6.2°C is expected on the northern Gaspé Peninsula during the 21st century (Figure 32). This rapid warming is likely to decrease the maximum depth of the seasonal freezing front by one to two metres and shorten its

duration by one to three months (Figure 34). The frequency and magnitude of sporadic FT cycles could increase in January and February and decrease in November and April (Figure 35). During the whole season, global warming appears to result in a higher FT cycle frequency near the surface and lower at greater depth (Figure 36). These change in the frost distribution in depth and over time would have a major impact on frost weathering effectiveness. The thermomechanical model developed by Rempel *et al.* (2016) was used to study the effectiveness of frost weathering in the current context of climate warming (Figure 37). This model quantifies porosity changes caused by the capillary migration of liquid water from unfrozen to frozen rockwall sections.

The porosity changes simulated during 30-year periods between 1950 and 2100 are very high and exceed 100% at certain depths (Figure 37). The sustained rates of porosity change can be explained by the favorable climatic conditions and the high porosity of the greywacke strata in rockwalls located in northern Gaspésie. It could also be the fact that we used a constant value of fracture toughness and porosity over time and because these values come from samples collected at the rockwall surface, they are probably overestimated at greater depths. Porosity changes values cannot exceed 100% and when this value is reached, this attest to the development of crack at these specific depths. These cracks can lead to the dissociation of blocks from the greywacke strata. The sliding or toppling failure mode of these blocks depends of the underlying strata. This erosion dynamic, reported by Birien and Gauthier (2022) and by Gauthier et al. (2022a), involves a gradual cantilevering of less weathered rock over time. This dynamic was not included in our simulation of porosity change because the objective of this study is not to quantify but to compare the effectiveness of frost weathering in the context of global warming. Thus, the authors assume that porosity increases driven by the formation of ice lenses is an indicator of frost-driven rock damage at different depths over time. In the historical periods, ice lens formation resulted in a preferential increase in porosity at the surface and at 0.7 m, 1.3 m and 2.7 m in depth (Figure 37). Prolonged exposure of certain depths to temperatures that promote water migration explains the presence of these peaks of porosity change (Rempel et al., 2016). At the end of the 21st century, this preferential increase is expected to persist at the surface, intensify at 0.7

m and diminish at greater depths according to RCP4.5. The marked rise in porosity change at 0.7 m in the late 21st century (Figure 37a) may be due to the increased number of oscillations around the freezing point at this depth than in the historical periods (Figure 36c). Considering RCP8.5, frost cracking effectiveness is predicted to decrease as of 10 cm in depth (Figure 37b) as a consequence of the reduction in the duration of freezing occurrence at greater depths (Figure 35).

Frost damage induced by the volumetric expansion of freezing water requires a rock water saturation of over 90% (Walder and Hallet, 1986; White, 1976) while frost damage due to ice segregation within the rock requires a saturation above 60% and temperatures between -8°C and -3°C (Rode et al., 2016). The increasing number of winter thaws in the late 21st century (Figure 35), will favor a greater availability of liquid water from melted interstitial ice and surface snow and from more frequent winter rain events (Gauthier et al., 2022b; Hall et al., 2002; Rode et al., 2016). Given the greater water saturation of the rock and increased numbers of FT cycles, weather conditions in 2100 should be more favorable to develop frost damage by volumetric expansion of freezing water near the rockwall surface. However, starting in the first decimeters below the surface, periods of rock temperatures within the range that promotes ice segregation can be expected to dwindle because of climate warming. While the effectiveness of frost cracking could increase near the surface and decrease at depth (Figure 37), low magnitude rockfall frequency should increase and high magnitude rockfall frequency should drop (Figure 38). In environments subject to seasonal freezing, global warming should favor the development of low magnitude rock instabilities over high magnitude ones.

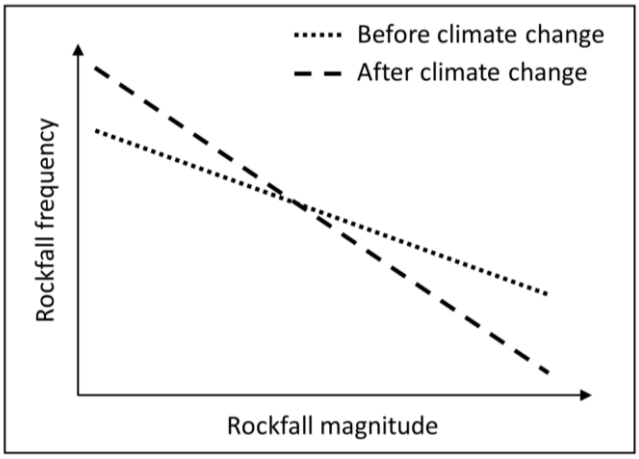

Figure 38. Relationship between rockfall frequency and magnitude in the context of global warming in environments subject to seasonal freezing.

The effectiveness of other processes than frost weathering could also be altered by modern climate change. An increase in mean air temperature of 3 to 6°C by the end of the 21st century (Figure 32 and Table 6) would likely result in more rainfall and less snowfall in winter (Rode et al., 2016) and thus, increased liquid water availability. Rain events are particularly effective rockfall triggering factors (Birien and Gauthier, 2022; D'Amato et al., 2016; Delonca et al., 2014; Matsuoka, 2019), and most other weathering processes are also dependent on liquid water inputs (Hall et al., 2002). This is particularly the case for dissolution, carbonation, hydrolysis and redox (Dixon and Thorn, 2005). Given the higher availability of liquid water in winter expected by the late 21st century, the effectiveness of these processes on rockwall surfaces and the resulting rates of weathering and erosion can be expected to rise.

The 21st century's climate changes are likely to result in the progressive disappearance of October and May frosts. Between 1950 and 2100, the frequency of sporadic FT cycles in November could be divided by 3 according to RCP4.5 and by 12 according to RCP8.5 (Figure 35). A decrease in both the effectiveness of frost weathering at the surface and the depth at which it operates can be expected. This should reduce the frequency of rockfall

triggered by FT cycles, particularly large magnitude rock instabilities (Figure 39a). In December, the frequency of sporadic FT cycles can be expected to double (Figure 35), but the freezing depth will decrease. By extension, the frequency of low magnitude rockfall triggered by freeze-thaw cycles should increase while the frequency of higher magnitude instabilities should decrease (Figure 39b).

Historically, the winter period was particularly stable (Laliberté et al., 2022) since the ice in cracks provided unstable blocks with significant cohesion (Fiorio et al., 2002; Krautblatter et al., 2013). At the end of the 21st century, this period could be regularly interrupted by winter thaws. Compared to the period 1950–1979, their frequency could increase fivefold in January and threefold in February considering RCP4.5 and twelvefold and eightfold considering RCP8.5 (Figure 35). The volumetric expansion caused by short-term FT cycles can be expected to be exacerbated at the rockwall surface. This trend would extend to greater depths since the intensity and duration of winter thaws favor higher amplitude FT cycles. As a result, the rockfall frequency should increase proportionally with rockfall magnitude (Figure 39c and Figure 39d). In March, the frequency of sporadic FT cycles would double (Figure 35), but the lower seasonal freezing front depth in winter (Figure 34 and Figure 36b) would not favor FT cycles of very high amplitude. The frequency of rockfall should therefore substantially increase at the surface and significantly decrease at depth (Figure 39e). In April, sporadic FT cycles would be two times (RCP4.5) to five times (RCP8.5) less frequent (Figure 35) and the freezing depth of these cycles should decrease. This should result in a lower frequency of small magnitude rockfall and the end of frost weathering at greater depths (Figure 39f).

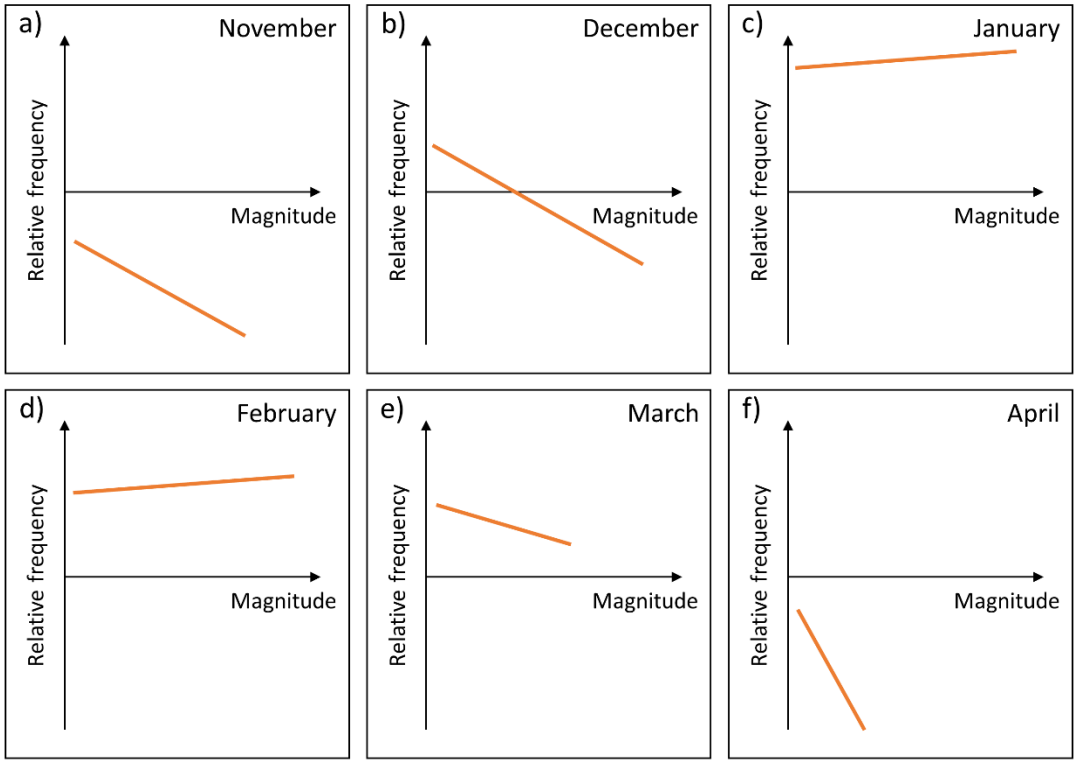

Figure 39. Relative frequency of rockfalls of varying magnitudes triggered by freeze-thaw cycles in 2100 compared to 1950, in a) November, b) December, c) January, d) February, e) March and f) April.

3.7.2 Global warming effect on rockwalls affected by permafrost, by seasonal frost and by sporadic frost

In periglacial environments, permafrost has a significant influence on rockfall dynamics (Draebing et al., 2022; Paranunzio et al., 2016; Rabatel et al., 2008; Ravanel and Deline, 2011). Climate change leads to permafrost degradation, resulting at the very least in an increase in the thickness of its active layer in summer and even by the complete loss of relict permafrost (Farbrot et al., 2013; Gray et al., 2017; Gruber and Haeberli, 2007; Gruber et al., 2004a; Noetzli et al., 2007). The increasing thickness of the active layer, along with a greater availability of liquid water (Rode et al., 2016) results in increased rockfall frequency

and, above all, magnitude in periglacial environments (Draebing et al., 2022; Gobiet et al., 2014; Hartmeyer et al., 2020; Ravanel and Deline, 2011) (Figure 40a).

In rock masses subject to seasonal frost, global warming is likely to lead to more frequent sporadic FT cycles, particularly in winter (Figure 35 and Figure 36), and greater liquid water availability (Rode et al., 2016). The periods of occurrence of these cycles should be shorter (Figure 35) and the freezing front should reach shallower depth (Figure 36). Compared to the historical period, late 21st century weather conditions would favor a rate of frost damage that is higher in rock close to the surface but significantly lower at depth (Figure 37). An increased frequency of small magnitude rockfall triggered by frost weathering and a decreased frequency of higher magnitude instabilities can be expected (Figure 40b).

Some midlatitude climates such as those of the low mountain in the European Alps (e.g. D'Amato et al., 2016; Rode et al., 2016), the Japanese Alps (e.g. Matsuoka, 1991), the Sierra Nevada (e.g. Wieczorek and Jäger, 1996) or the Canadian coast mountain (e.g. van Veen et al., 2017) are more temperate than those of northern Gaspésie (Beck et al., 2018). They experience a higher frequency of sporadic FT cycles, shorter winter periods and an absence of seasonal freezing fronts. In this context, frequent winter temperature oscillations around the freezing point promote the development of small magnitude rock instabilities (D'Amato et al., 2016; Delonca et al., 2014; Kromer et al., 2018; Macciotta et al., 2015; van Veen et al., 2017). Climate warming by the end of the 21st century in these regions can be expected to reduce the frequency and amplitude of winter FT cycles, or even eliminate them (Rode et al., 2016). This should reduce the frequency of small magnitude rockfall triggered by sporadic FT cycles (Figure 40b).

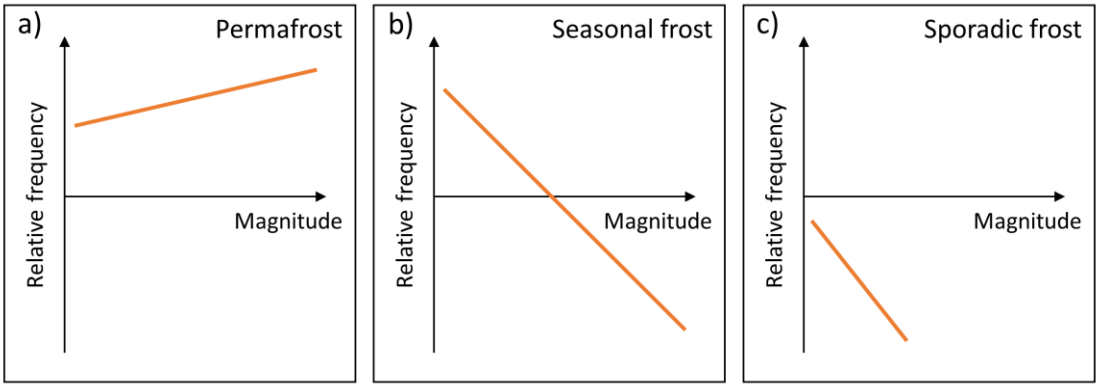

Figure 40. Relative frequency of rockfalls of varying magnitudes triggered by freeze-thaw cycles in 2100 compared to 1950 in regions affected by a) permafrost, b) seasonal frost and c) sporadic frost.

3.8 CONCLUSION

An instrument array installed on a rockwall of the northern Gaspé Peninsula was used to calculate its surface energy balance and measure its thermal regime to a depth of 5.5 m over a period of 28 months (2018–2020). These measurements were used to calibrate a thermodynamic model (WUFI® Pro) and simulated the rockwall thermal regime to a depth of 20 m. A combination of locally recorded historical air temperature data (1950–2020) and climate simulation data (2021–2099) based on RCP4.5 and RCP8.5 made it possible to simulate the thermal regime over a period of 150 years. This time series was then used as input in a frost damage model that calculate rock porosity change through time (Rempel et al., 2016). Five freeze-thaw and frost damage indicators were quantified to explain the effects of global warming on rockwall frost weathering and rockfall dynamic by the end of the 21st century.

Depending on the scenario, the climate of the northern Gaspé Peninsula can be expected to warm by 3.3°C (RCP4.5) to 6.2°C (RCP8.5) during the 21st century. This rapid warming will likely result in a significant decrease in the maximum depth of the seasonal freezing front, a truncated period of occurrence of sporadic FT cycles and a very substantial

increase in their frequency in winter. Compared to the historical period (1950–2009) and following RCP4.5, frost cracking effectiveness should intensify around 70 cm in depth and disappear beyond that. According to RCP8.5, frost cracking effectiveness is predicted to decrease as of 10 cm in depth. In rock masses subject to seasonal freezing, the changes predicted in frost weathering process effectiveness by the end of the 21st century should favor the development of small magnitude rock instabilities over high magnitude ones. The frequency of rockfall triggered by sporadic FT cycles could grow considerably in winter but be significantly diminished in fall and spring.

In colder environments, where rockslope are affected by permafrost, the increasing thickness of the active layer, along with a greater availability of liquid water (Rode et al., 2016) should result in increased rock instability frequency and, above all, magnitude. In warmer environments, where rockslope are only affected by sporadic FT cycle, global warming is likely to diminish the frequency and intensity of winter FT cycles. This would also reduce the frequency of small magnitude rockfalls triggered by those cycles.

Future work should focus on other mechanical and chemical weathering processes that will be altered by the changing weather conditions and availability of liquid water. These processes could also influence the rockwall retreat rate and thus the frequency and magnitude of rock instabilities in the late 21st century and may interact with the cryogenic process presented in this study.

3.9 ACKNOWLEDGMENTS

We acknowledge the World Climate Research Programme's Working Group on Regional Climate, and the Working Group on Coupled Modelling, former coordinating body of CORDEX and responsible panel for CMIP5. We also thank the climate modelling groups (listed in Table 3 of this paper) for producing and making available their model output. We also acknowledge the U.S. Department of Defense ESTCP for its support of the NA-

CORDEX data archive. We are grateful for the work and support of Guillaume Dueymes for the preparation of the data and their distribution, and of the Centre pour l'Étude et la Simulation du Climat à l'Échelle Régionale (ESCER) at the Université du Québec à Montréal (UQAM). Finally, we thank the Laboratoire ouvert de géothermie (LOG) of the Institut National de la Recherche Scientifique (INRS) for their help and we are particularly grateful for the assistance provided by Nicolo Giordano. This work was financially supported by the ministère des Transports du Québec (MTQ) and by the Natural Sciences and Engineering Research Council of Canada (NSERC).

CONCLUSIONS GÉNÉRALES

1. SYNTHESE

Une instrumentation conséquente et inédite a été déployée sur cinq parois rocheuses de la Haute-Gaspésie. Les conditions météorologiques ont été enregistrées à leur surface et leur régime thermique a été mesuré jusqu'à 5,5 m de profondeur. Les déformations majeures affectant deux segments de roche distincts d'une paroi de flysch ont été mesurées pendant une période de 28 mois. Un premier extensomètre enregistrait les déplacements verticaux dans une strate de siltstone altérée et un second extensomètre enregistrait les mouvements horizontaux dans une strate de grès au niveau d'un fracture ouverte. La fréquence et la magnitude des chutes de pierres ont également été quantifiées au LiDAR sur trois parois rocheuses pour une surface totale de 12 000 m² pendant une période de 18 mois. Cette instrumentation a notamment permis de :

- Mesurer la température de parois rocheuses à une profondeur excédant celle atteinte par le front de gel saisonnier ;
- Quantifier le rôle respectif de processus de météorisation mécanique sur l'altération et sur l'érosion des parois rocheuses ;
- Calculer le bilan d'énergie à la surface des parois rocheuses et modéliser leur régime thermique en profondeur.

Les résultats du chapitre 1 permettent de brosser un portrait d'ensemble des processus qui entraînent des déformations mécaniques et qui contribuent à l'altération des parois de roche sédimentaire. Les déformations irréversibles enregistrées à la surface de la roche sont principalement induites par les variations brèves et soutenues de la teneur en eau (pluies et

fonte des neiges), par les fluctuations de température autour du point de congélation (cycles gel-dégel) et dans une moindre mesure, par les fortes amplitudes thermiques. L'utilisation des ACP a permis de 1) discriminer l'influence respective des processus de météorisation et plus spécifiquement les processus d'hydroclastie et de cryoclastie, 2) de mettre en évidence l'effet décuplé des processus de météorisation lorsqu'ils s'additionnent, et 3) de limiter la surestimation ou la sous-estimation de leurs effets individuels.

Les tendances sur le long terme enregistrées par les extensomètres attestent des mécanismes qui conduisent à l'érosion différentielle des parois de flysch. Les strates silto-argileuses moins résistantes et plus fracturées s'érodent rapidement et entraînent la mise en surplomb des strates de grès sus-jacentes. L'érosion des strates moins résistantes se matérialise par leur recul et par leur amincissement à la suite de la perte de fragments de roche. Leur recul conduit au basculement des blocs de grès sus-jacents alors que leur affaissement ou tassement conduit au glissement de ces blocs. La dynamique d'érosion des strates silto-argileuses conditionne donc le mode de rupture des blocs de grès sus-jacents ainsi que leur période d'occurrence. Ce résultat souligne l'importance d'étudier la dynamique de la paroi rocheuse dans sa globalité puisque la chute des blocs de grès (qui représente un risque pour la sécurité des usagers des routes) peut être une conséquence directe de la perte de fragments dans les strates de siltstone ou de shale sous-jacentes.

Le second chapitre est la suite logique du premier puisqu'il s'intéresse aux processus responsables du déclenchement des chutes de pierres. Les relevés LiDAR montrent que certaines conditions météorologiques sont associées à une stabilité marquée des parois rocheuses (période sèche estivale, période froide hivernale) alors que d'autres augmentent significativement la fréquence et/ou la magnitude des chutes de pierres (redoux hivernal, dégel printanier, pluie de forte intensité). Les redoux hivernaux ou les pluies modérées entraînent une augmentation marquée de la fréquence des instabilités rocheuses de faible magnitude. Les pluies de forte intensité se répercutent par une augmentation de la fréquence des instabilités rocheuses de faible et de grande magnitude. À l'inverse, le dégel printanier en profondeur favorise une fréquence importante des chutes de pierres de grandes

magnitudes. Cette étude démontre l'importance de quantifier la magnitude des chutes de pierres puisque la relation entre les conditions météorologiques et la fréquence de ces instabilités rocheuses ne s'applique pas forcément à la magnitude. Ce résultat est particulièrement important dans une optique de gestion préventive du risque, dans la mesure où l'intensité du risque naturel est proportionnelle à la magnitude des chutes de pierres. Les résultats obtenus dans ce chapitre permettent de hiérarchiser les conditions météorologiques en fonction de leur capacité à déclencher des instabilités rocheuses de différentes magnitudes. Le protocole mis en place dans ce chapitre est novateur et présente de nombreux avantages. Les relevés LiDAR sont traditionnellement effectués sur une base régulière (e.g. fréquence hebdomadaire, mensuelle ou saisonnière), même lorsque l'objectif est de mettre en relation les conditions météorologiques avec la dynamique des chutes de pierres (e.g. Kromer et al. 2018). Nous avons fait le choix d'utiliser les prévisions météorologiques afin de cibler des conditions spécifiques au préalable. Les périodes de relevés circonscrivaient des conditions considérées comme favorables aux instabilités ou au contraire, propices à la stabilité. Pour un nombre de relevés équivalent et donc pour un même effort de collecte de données, ce protocole a permis de suivre plus efficacement l'influence des conditions météorologiques sur la fréquence et sur la magnitude des chutes de pierres que les relevés effectués à période régulière. Ainsi, l'originalité de la méthode ne réside pas dans l'utilisation du LiDAR pour quantifier la dynamique des chutes de pierres, mais bien dans l'approche utilisée pour optimiser l'acquisition de données pertinentes.

Le chapitre 3 avait pour objectif d'étudier l'influence du réchauffement climatique contemporain sur l'efficacité de la cryoclastie et sur la dynamique des chutes de pierres. Pour y parvenir, le régime thermique de la paroi rocheuse de MAE a été modélisé entre 2018 et 2020 à partir de mesures de son absorptivité de surface et de la conductivité, de la capacité et de la diffusivité thermique de ses principales unités géologiques. Le régime thermique modélisé au cours de cette période a pu être validé par les mesures de températures enregistrées jusque 550 cm de profondeur dans la paroi. Des données de température de l'air historiques enregistrées localement (1950-2020) et des données de simulation issues de cinq modèles régionaux du climat (2021-2100) ont permis d'étendre la modélisation du régime

thermique sur une période de 150 ans. Le régime thermique de la paroi rocheuse a été modélisé suivant les scénarios RCP4.5 et RCP8.5 du GIEC. En Haute-Gaspésie, le réchauffement climatique du 21ème siècle serait compris entre 3.3°C (RCP4.5) et 6.2°C (RCP8.5). Ce réchauffement rapide de la température de l'air devrait se répercuter par une diminution d'un à deux mètres de la profondeur maximale atteinte par le front de gel saisonnier. La fréquence des cycles gel-dégel sporadiques devrait être divisée par 12 en novembre et par 5 en avril alors qu'elle devrait être respectivement multipliée par 12 et par 8 en janvier et en février. Un raccourcissement de la période d'occurrence de ces cycles – mais une augmentation importante de leur fréquence en hiver – sont attendues d'ici la fin du 21ème siècle. Le modèle thermomécanique développé par Rempel et al. (2016) a été utilisé pour quantifier l'efficacité de l'altération par le gel au sein d'une paroi rocheuse entre 1950 et 2100. D'ici la fin du 21ème siècle, l'efficacité de la cryoclastie pourrait s'intensifier autour de 70 cm de profondeur et s'estomper au-delà (RCP4.5). Dans le cas du scénario RCP8.5, l'efficacité de ce processus deviendrait moindre dès 10 cm de profondeur. Dans les massifs soumis à des gels saisonniers, la redistribution de l'efficacité du processus de cryoclastie d'ici la fin du 21ème siècle devrait favoriser le développement d'instabilités rocheuses de faible magnitude au détriment de celles de plus grande magnitude. La fréquence des chutes de pierres déclenchées par les cycles FT sporadiques pourrait s'accroître considérablement en hiver mais être largement réduite à l'automne et au printemps.

En s'appuyant sur les résultats des trois chapitres de cette thèse, l'influence du réchauffement climatique contemporain sur la fréquence et la magnitude des chutes de pierres dans les environnements périglaciaires ainsi que dans les environnements soumis à des gels saisonniers ou sporadiques a été discutée dans la dernière partie du chapitre 3. L'effet du réchauffement climatique sur la fréquence et la magnitude des chutes de pierres est largement dépendant des caractéristiques du climat initial et de celles du climat nouvellement atteint. Dans le pergélisol, la progression de la profondeur de sa couche active, accompagnée d'une plus grande disponibilité en eau liquide (Rode et al., 2016) devrait se traduire par une augmentation de la fréquence et surtout, de la magnitude des instabilités rocheuses d'ici la fin du 21ème siècle (Draebing et al., 2022; Gobiet et al., 2014; Hartmeyer et al., 2020; Ravanel

and Deline, 2011). Dans les massifs rocheux soumis à des gel saisonniers, l'augmentation de la fréquence des redoux hivernaux se traduirait par une fréquence plus soutenue des chutes de pierres de faible magnitude. À l'inverse, la plus faible pénétration du front de gel en profondeur ne favorisera plus les instabilités de grande magnitude lors du dégel printanier. Dans les environnements actuellement caractérisés par la présence de cycles gel-dégel sporadiques uniquement en hiver, le réchauffement climatique du 21ème siècle entrainera une raréfaction de la fréquence et de l'intensité de ces cycles. Il en découlerait une diminution de la fréquence des chutes de pierres de faible magnitude déclenchées par le processus de cryoclastie.

2. CONTRIBUTION A LA GESTION PREVENTIVE DES CHUTES DE PIERRES

Les connaissances acquises dans les chapitres 1 et 2 de ce projet permettent de mieux cerner les mécanismes de développement des instabilités rocheuses dans les massifs de flysch. En mettant en relation les conditions météorologiques à la surface des parois rocheuses ainsi que leur régime thermique avec la fréquence et la magnitude des instabilités rocheuses, cette étude propose une classification des conditions météorologiques en fonction de leur capacité à déclencher des instabilités rocheuses de différentes magnitudes. Dans une optique de gestion du risque naturel, la magnitude des instabilités rocheuses susceptibles de survenir à un instant donné est un paramètre essentiel à prendre en compte puisque les dommages causés par ces instabilités sont proportionnels à leur magnitude. Selon les conditions météorologiques occurrentes ou prédites à court terme, différentes mesures de mitigation du risque pourraient être mises en place par les gestionnaires afin de limiter les risques d'accident. Pendant des périodes précises, des panneaux indicateurs mobiles avertissant les usagers des routes qu'ils pénètrent dans une zone à risque ou la fermeture d'une voie (circulation en alternance) sont des mesures simples et peu onéreuses qui pourraient être déployées par les gestionnaires du MTQ. La mise en place d'une gestion préventive permettrait de diminuer la vulnérabilité des usagers des routes nationales 132 et

198. En s'intéressant à l'influence du réchauffement climatique sur la dynamique des chutes de pierres, le chapitre 3 apporte des connaissances essentielles aux gestionnaires en anticipant dès à présent l'évolution des périodes favorables aux instabilités et des périodes propices à la stabilité des parois rocheuses. Les connaissances acquises à travers ce projet pourraient s'exporter à d'autres parois rocheuses, et notamment à celles soumises à des gels saisonniers, afin de mettre en place ce type de gestion du risque de chutes de pierres dans d'autres secteurs problématiques.

3. PERSPECTIVES DE RECHERCHE

Les résultats de ce projet soulèvent d'autres problématiques qui mettent en évidence de nouvelles perspectives de recherche. À l'avenir, nous recommandons de poursuivre les recherches en approfondissant notre compréhension des grandes thématiques suivantes :

- Cette étude apporte les connaissances nécessaires à l'élaboration d'un outil de gestion préventive du risque de chutes de pierres en Haute-Gaspésie, basé sur les facteurs qui les déclenchent. De futures investigations pourraient porter sur les modalités nécessaires à la mise en place de cet outil de façon opérationnelle.

- Il s'est avéré complexe de discerner clairement le processus de météorisation qui entraînent certaines déformations majeures. Par exemple, une déformation qui coïncide avec une augmentation de la teneur en eau pourrait être causée par une variation de la pression hydrostatique, par le processus d'hydratation-dessiccation ou simplement par la perte de particules et de fragments de roche dans une discontinuité. Une instrumentation affinée pourrait être pensée afin d'améliorer notre capacité à discriminer ces processus.

- Bien que les résultats présentés dans les différents chapitres de cette thèse devraient pouvoir s'exporter à d'autres parois rocheuses exposées à des gels

saisonniers, ils n'en demeurent pas moins des résultats spécifiques aux sites d'étude. Des études similaires effectuées dans d'autres types de géologie et contextes climatiques pourraient venir compléter nos résultats.

- Pour quantifier l'efficacité du processus de cryoclastie, l'évolution de la teneur en eau dans les pores et dans les discontinuités des massifs rocheux, à travers le temps et à différentes profondeurs est un prérequis primordial. À ce jour, aucune étude ne mesure le degré de saturation des roches en profondeur. Quelques auteurs la modélisent mais ils font abstractions des fluctuations éventuelles du niveau de la nappe phréatique et des apports par advection d'eau qui pourraient jouer un rôle important dans le degré de saturation des roches hautement fracturées. Le développement d'instruments de mesure adaptés serait nécessaire pour répondre à cette problématique.

- De nombreux auteurs discutent de la température à partir de laquelle l'eau sous pression gèle dans les pores de la roche ainsi que de la température nécessaire pour que ce gel entraîne des dommages. Définir une température critique universelle n'est pas envisageable car le point de congélation dépend de plusieurs paramètres dont l'intensité et la durée du gel, la pression, la porosité de la roche ou la résistance à la fracturation. Afin de quantifier l'efficacité du processus de cryoclastie, considérer la valeur de 0°C comme point de congélation est trop simpliste et pourrait ne pas être représentatif de la réalité, notamment pour des roches caractérisées par une faible porosité. Davantage de travaux sont nécessaires dans ce domaine.

- Le réchauffement climatique devrait se traduire par une plus forte disponibilité en eau liquide, notamment en hiver, dans les environnements périglaciaires et dans les régions soumises à des gels saisonniers. L'efficacité des processus de météorisation mécaniques et chimiques dépendants de cette disponibilité en eau pourrait être quantifiée.

- Les changements climatiques se répercuteront également par une modification du régime de précipitations. Étant donné que les événements de pluie sont susceptibles de déclencher des chutes de pierres, de nouvelles investigations permettraient de mieux anticiper l'influence des changements climatiques sur la dynamique des chutes de pierres.

Le LGRRM assure la pérennité de l'instrumentation du site de GMO et de nombreux nouveaux équipements ont été installés depuis le début du projet, faisant de ce site un véritable laboratoire à ciel ouvert. Cette instrumentation devrait nous permettre de continuer à contribuer à approfondir notre compréhension des mécanismes responsables de l'altération et de l'érosion des parois rocheuses dans les prochaines années.

RÉFÉRENCES

Abellán, A., Oppikofer, T., Jaboyedoff, M., Rosser, N. J., Lim, M. et Lato, M. J. (2014). Terrestrial laser scanning of rock slope instabilities. *Earth Surface Processes and Landforms*, *39*(1), 80–97. https://doi.org/10.1002/esp.3493

Alvioli, M., Melillo, M., Guzzetti, F., Rossi, M., Palazzi, E., von Hardenberg, J., … et Peruccacci, S. (2018). Implications of climate change on landslide hazard in Central Italy. *Science of the Total Environment*, *630*, 1528–1543. https://doi.org/10.1016/j.scitotenv.2018.02.315

Anders, K., Winiwarter, L., Lindenbergh, R., Williams, J. G., Vos, S. E. et Höfle, B. (2020). 4D objects-by-change: Spatiotemporal segmentation of geomorphic surface change from LiDAR time series. *ISPRS Journal of Photogrammetry and Remote Sensing*, *159*, 352–363. https://doi.org/10.1016/j.isprsjprs.2019.11.025

Anderson, R. S., Anderson, S. P. et Tucker, G. E. (2013). Rock damage and regolith transport by frost : an example of climate modulation of the geomorphology of the critical zone. *Earth Surface Processes and Landforms*, *38*(3), 299–316. https://doi.org/10.1002/esp.3330

Anderson, T. L. (2005). *Fracture mechanics: fundamentals and applications*. (CRC Press, Ed.) (3rd edn). Boca Raton.

André, M. F. (1997). Holocene rockwall retreat in Svalbard : a triple-rate evolution. *Earth Surface Processes and Landforms*, *22*, 423–440. https://doi.org/10.1002/(SICI)1096-9837(199705)22:5<423::AID-ESP706>3.0.CO;2-6

Badger, T. C. et Lowell, S. M. (1992). Rockfall Control in Washington State, rockfall prediction and control and landslide case histories. *Transportation Research Record*, *1343*, 14–19.

Badoux, A., Andres, N., Techel, F. et Hegg, C. (2016). Natural hazard fatalities in Switzerland from 1946 to 2015. *Natural Hazards and Earth System Sciences*, *16*(12), 2747–2768. https://doi.org/10.5194/nhess-16-2747-2016

Ballantyne, C. K. et Kirkbride, M. P. (1987). Rockfall activity in upland Britain during the Loch Lomond Stadial. *The Geographical Journal*, *153*(1), 86–92. https://doi.org/10.2307/634474

Barlow, J., Lim, M., Rosser, N., Petley, D., Brain, M., Norman, E. et Geer, M. (2012). Modeling cliff erosion using negative power law scaling of rockfalls. *Geomorphology*, *139–140*, 416–424. https://doi.org/10.1016/j.geomorph.2011.11.006

Barsch, D. (1977). Eine Abschätzung von Schuttproduktion und Schutttransport im Bereich aktiver Blockgletscher in den Sch weitzer Alpen. *Zeitschrift FürGeomorphologie, Neue Folge, Supplement*.

Beck, H. E., Zimmermann, N. E., McVicar, T. R., Vergopolan, N., Berg, A. et Wood, E. F. (2018). Present and future köppen-geiger climate classification maps at 1-km resolution. *Scientific Data*, *5*, 1–12. https://doi.org/10.1038/sdata.2018.214

Becker, A. et Davenport, C. A. (2003). Rockfalls triggered by the AD 1356 Basle Earthquake. *Terra Nova*, *15*(4), 258–264. https://doi.org/10.1046/j.1365-3121.2003.00496.x

Bernstein, L., James, N. P. et Lavoie, D. (1992). Cambro-Ordovician stratigraphy in the Quebec reentrant, Grosses-Roches - Les Mechins Area, Gaspesie, Quebec. *Geological Survey of Canada*, *92*, 381–392.

Beylich, A. A. (2000). Geomorphology, Sediment Budget, and Relief Development in Austdalur, Austfirðir, East Iceland. *Arctic, Antarctic, and Alpine Research*, *32*(4), 466–477. https://doi.org/10.1080/15230430.2000.12003391

Birien, T. et Gauthier, F. (2022). Dynamique des parois de flysch (partie2) : conditions météorologiques propices aux chutes de pierres. *In* Société canadienne de géotechnique (Ed.), *8e conférence canadienne sur la géotechnique et les risques naturels - Géorisques 8* (pp. 385–393). Québec.

Birien, T. et Gauthier, F. (2022). Influence of climate-dependent variables on deformation and differential erosion of stratified sedimentary rocks. *Geomorphology*, *421*, 108518. https://doi.org/10.2139/ssrn.4046480

Blikra, L. H. et Christiansen, H. H. (2014). A field-based model of permafrost-controlled rockslide deformation in northern Norway. *Geomorphology*, *208*, 34–49. https://doi.org/10.1016/j.geomorph.2013.11.014

Bost, M. (2008). *Altération par le gel des massifs rocheux : Etude expérimentale et modélisation des mécanismes de génération des contraintes dans les fissures*. Ecole des Ponts ParisTech. Retrieved from https://pastel.archives-ouvertes.fr/tel-00360420

Brázdil, R., Šilhán, K., Pánek, T., Dobrovolný, P., Kašičková, L. et Tolasz, R. (2012). The influence of meteorological factors on rockfall in the Moravskoslezské Beskydy Mts. *Geografie-Sbornik CGS*, *117*(1), 1–20. https://doi.org/10.37040/geografie2012117010001

Brisebois, D. et Nadeau, J. (2003). *Géologie de la Gaspésie et du Bas-Saint-Laurent (SNRC 22A, 22B, 22C, 22G, 22H, 21N et 21O). Ministère des Ressources Naturelles, de la Faune et des Parcs (MRNFP), Québec. DV 2003-08, échelle 1/250 000*.

Budetta, P. (2004). Assessment of rockfall risk along roads. *Natural Hazards and Earth System Science*, *4*(1), 71–81. https://doi.org/10.5194/nhess-4-71-2004

Bunce, C. M., Cruden, D. M. et Morgenstern, N. R. (1997). Assessment of the hazard from rock fall on a highway. *Canadian Geotechnical Journal*, *34*(3), 344–356. https://doi.org/10.1139/cgj-34-3-344

Burnett, B. N., Meyer, G. A. et McFadden, L. D. (2008). Aspect-related microclimatic influences on slope forms and processes northeastern Arizona. *Journal of Geophysical Research: Earth Surface*, *113*(3), 1–18. https://doi.org/10.1029/2007JF000789

Cano, M. et Tomás, R. (2013). Characterization of the instability mechanisms affecting slopes on carbonatic Flysch: Alicante (SE Spain), case study. *Engineering Geology*, *156*, 68–91. https://doi.org/10.1016/j.enggeo.2013.01.009

Chau, K T, Wong, R. H. C., Liu, J. et Lee, C. F. (2003). Rockfall Hazard Analysis for Hong Kong Based on Rockfall Inventory. *Rock Mechanics and Rock Engineering*, *36*, 383–408. https://doi.org/10.1007/s00603-002-0035-z

Chau, Kam Tim, Wong, R. H. C., Liu, J. et Lee, C. F. (2003a). Rockfall Hazard Analysis for Hong Kong Based on Rockfall Inventory. *Rock Mechanics and Rock Engineering*, *36*(5), 383–408. https://doi.org/10.1007/s00603-002-0035-z

Chau, Kam Tim, Wong, R. H. C., Liu, J. et Lee, C. F. (2003b). Rockfall Hazard Analysis for Hong Kong Based on Rockfall Inventory. *Rock Mechanics and Rock Engineering*, *36*(5), 383–408. https://doi.org/10.1007/s00603-002-0035-z

Christensen, O. B., Drews, M., Christensen, J. H., Dethloff, K., Ketelsen, K., Hebestadt, I. et Rinke, A. (2007). *The HIRHAM Regional Climate Model Version 5 (beta). Technical Report 06-17;* (Vol. 5). Retrieved from http://orbit.dtu.dk/fedora/objects/orbit:118724/datastreams/file_8c69af6e-acfb-4d1a-aa53-73188c001d36/content

Cloutier, C., Locat, J., Charbonneau, F. et Couture, R. (2015). Understanding the kinematic behavior of the active Gascons rockslide from in-situ and satellite monitoring data. *Engineering Geology*, *195*, 1–15. https://doi.org/10.1016/j.enggeo.2015.05.017

Coe, J. A. et Harp, E. L. (2007). Influence of tectonic folding on rockfall susceptibility, American Fork Canyon, Utah, USA. *Natural Hazards and Earth System Science*, *7*(1), 1–14. https://doi.org/10.5194/nhess-7-1-2007

Coe, Jeffrey A. et Godt, J. W. (2012). Review of approaches for assessing the impact of climate change on landslide hazards. *In* Eberhardt, E., Froese, C., Turner, A.K., Leroueil, S. (Eds.), Landslides and Engineered Slopes, Protecting Society Through Improved Understanding: Proceedings 11th International and 2nd North American Symposium on Landslides and Engineered Slopes, Ban (pp. 371–377).

Collins, B. D. et Stock, G. M. (2016). Rockfall triggering by cyclic thermal stressing of exfoliation fractures. *Nature Geoscience*, *9*(5), 395–400. https://doi.org/10.1038/ngeo2686

Collins, M., Knutti, R., Arblaster, J., Dufresne, J.-L., Fichefet, T., Friedlingstein, P., … et Wehner, M. (2013). Long-term climate change: Projections, commitments and irreversibility. *In* Climate Change 2013 the Physical Science Basis: Working Group I Contribution to the Fifth Assessment Report of the Intergovernmental Panel on Climate Change. https://doi.org/10.1017/CBO9781107415324.024

Coutard, J. P. et Francou, B. (1989). Rock temperature measurements in two alpine environments: implications for frost shattering. *Arctic & Alpine Research*, *21*(4), 399–416. https://doi.org/10.2307/1551649

Cripps, C. C. et Taylor, R. K. (1981). The engineering properties of mudrocks. *Quarterly Journal of Engineering Geology and Hydrogeology*, *14*(4), 325–346. https://doi.org/10.1144/GSL.QJEG.1981.014.04.10

Crosta, G. B. et Clague, J. J. (2009). Dating, triggering, modelling, and hazard assessment of large landslides. *Geomorphology*, *103*(1), 14. https://doi.org/10.1016/j.geomorph.2008.04.007

Crosta, G. B., di Prisco, C., Frattini, P., Frigerio, G., Castellanza, R. et Agliardi, F. (2013). Chasing a complete understanding of the triggering mechanisms of a large rapidly evolving rockslide. *Landslides*, *11*(5), 747–764. https://doi.org/10.1007/s10346-013-0433-1

Crozier, M. J. (2010). Deciphering the effect of climate change on landslide activity: A review. *Geomorphology*, *124*(3–4), 260–267. https://doi.org/10.1016/j.geomorph.2010.04.009

Curry, A. M. et Morris, C. J. (2004). Lateglacial and Holocene talus slope development and rockwall retreat on Mynydd Du, UK. *Geomorphology*, *58*, 85–106. https://doi.org/10.1016/S0169-555X(03)00226-5

D'Amato, J., Hantz, D., Guerin, A., Jaboyedoff, M., Baillet, L. et Mariscal, A. (2016). Influence of meteorological factors on rockfall occurrence in a middle mountain limestone cliff. *Natural Hazards and Earth System Sciences*, *16*(3), 719–735. https://doi.org/10.5194/nhess-16-719-2016

Davidson, G. P. et Nye, J. F. (1985). A photoelastic study of ice pressure in rock cracks. *Cold Regions Science and Technology*, *11*(2), 141–153. https://doi.org/10.1016/0165-232X(85)90013-8

Delonca, A., Gunzburger, Y. et Verdel, T. (2014). Statistical correlation between meteorological and rockfall databases. *Natural Hazards and Earth System Sciences*, *14*(8), 1953–1964. https://doi.org/10.5194/nhess-14-1953-2014

Dixon, J. C. et Thorn, C. E. (2005). Chemical weathering and landscape development in mid-latitude alpine environments. *Geomorphology*, *67*(1-2 SPEC. ISS.), 127–145. https://doi.org/10.1016/j.geomorph.2004.07.009

Données Québec. (2022). Débits de circulation (Transports Québec). Retrieved July 18, 2022, from https://www.donneesquebec.ca/recherche/dataset/debit-de-circulation/resource/2bd6ea5d-ba7f-44d5-afcd-4ca968897c1d

Dorren, L. K. A. (2003). A review of rockfall mechanics and modelling approaches. *Progress in Physical Geography*, *27*(1), 69–87. https://doi.org/10.1191/0309133303pp359ra

Douglas, G. R. (1980). Magnitude frequency study of rockfall in Co. Antrim, N. Ireland. *Earth Surface Processes*, *5*, 123–129. https://doi.org/10.1002/esp.3760050203

Draebing, D. (2021). Identification of rock and fracture kinematics in high alpine rockwalls under the influence of elevation. *Earth Surface Dynamics*, *9*(4), 977–994. https://doi.org/10.5194/esurf-9-977-2021

Draebing, D. et Krautblatter, M. (2019). The Efficacy of Frost Weathering Processes in Alpine Rockwalls. *Geophysical Research Letters*, *46*(12), 6516–6524. https://doi.org/10.1029/2019GL081981

Draebing, D., Krautblatter, M. et Hoffmann, T. (2017). Thermo-cryogenic controls of fracture kinematics in permafrost rockwalls. *Geophysical Research Letters*, *44*(8), 3535–3544. https://doi.org/10.1002/2016GL072050

Draebing, D. et Mayer, T. (2021). Topographic and Geologic Controls on Frost Cracking in Alpine Rockwalls. *Journal of Geophysical Research: Earth Surface*, *126*(6). https://doi.org/10.1029/2021JF006163

Draebing, D., Mayer, T., Jacobs, B. et McColl, S. T. (2022). Alpine rockwall erosion patterns follow elevation-dependent climate trajectories. *Communications Earth and Environment*, *3*(1), 1–12. https://doi.org/10.1038/s43247-022-00348-2

Dramis, F., Govi, M., Guglielmin, M. et Mortara, G. (1995). Mountain permafrost and slope instability in the Italian Alps: The Val Pola Landslide. *Permafrost and Periglacial Processes*, *6*(1), 73–81. https://doi.org/10.1002/ppp.3430060108

Drejza, S., Bernatchez, P., Marie, G. et Friesinger, S. (2019). Quantifying road vulnerability to coastal hazards: Development of a synthetic index. *Ocean and Coastal Management*, *181*, 104894. https://doi.org/10.1016/j.ocecoaman.2019.104894

Drejza, S., Michaud, M. et Bernatchez, P. (2014). *Vulnérabilité des infrastructures routières de l'est du Québec à l'érosion et à la submersion côtière dans un contexte de changements climatiques*. *Rapport remis au ministère des Transports du Québec* (Vol. 3). Rimouski.

Dunn, J. R. et Hudec, P. P. (1972). Frost and Sorption Effects in Argillaceous Rocks. *Highway Research Record*, (39), 65–78. Retrieved from http://onlinepubs.trb.org/Onlinepubs/hrr/1972/393/393-007.pdf

Duszyński, F., Migon, P. et Kasprzak, M. (2016). Underground erosion and sand removal from a sandstone tableland , Stołowe Mountains, SW Poland. *Catena*, *147*, 1–15. https://doi.org/10.1016/j.catena.2016.06.032

Duszyński, F., Migon, P. et Strzelecki, M. C. (2019). Escarpment retreat in sedimentary tablelands and cuesta landscapes – Landforms, mechanisms and patterns. *Earth-Science Reviews*, *196*, 42. https://doi.org/10.1016/j.earscirev.2019.102890

Dwivedi, R. D., Soni, A. K., Goel, R. K. et Dube, A. K. (2000). Fracture toughness of rocks under sub-zero temperature conditions. *International Journal of Rock Mechanics and Mining Sciences*, *37*(8), 1267–1275. https://doi.org/10.1016/S1365-1609(00)00051-4

Eberhardt, E., Stead, D. et Coggan, J. S. (2004). Numerical analysis of initiation and progressive failure in natural rock slopes-the 1991 Randa rockslide. *International Journal of Rock Mechanics and Mining Sciences*, *41*(1), 69–87. https://doi.org/10.1016/S1365-1609(03)00076-5

Enos, P. (1969a). Anatomy of a flysch. *Journal of Sedimentary Petrology*, *39*(2), 680–723.

Enos, P. (1969b). *Cloridorme formation, middle ordovician flysch, Northern Gaspé peninsula, Québec*. (Geological Society of America INC, Ed.). Colorado building, Boulder, Colorado: Geological Society of America.

Environnement Canada. (2021). Compilation des données historiques à la station météorologique de Cap-Madeleine. Retrieved November 22, 2021, from https://climat.meteo.gc.ca/historical_data/search_historic_data_f.html

Eppes, M.-C., et Keanini, R. (2017). Mechanical weathering and rock erosion by climate-dependant subcritical cracking. *Reviews of Geophysics*, *55*(2), 470–508. https://doi.org/10.1002/2017RG000557

Eppes, M. C., Magi, B., Hallet, B., Delmelle, E., Mackenzie-Helnwein, P., Warren, K. et

Swami, S. (2016). Deciphering the role of solar-induced thermal stresses in rock weathering. *Bulletin of the Geological Society of America*, *128*(9–10), 1315–1338. https://doi.org/10.1130/B31422.1

Erismann, T. et Abele, G. (2001). *Dynamics of rockslides and rockfalls*. (Springer, Ed.). Berlin: Heidelberg New York. https://doi.org/10.1007/978-3-662-04639-5

Fahey, B. D. et Lefebure, T. H. (1988). The freeze-thaw weathering regime at a section of the Niagara escarpment on the Bruce Peninsula, Southern Ontario, Canada. *Earth Surface Processes and Landforms*, *13*(4), 293–304. https://doi.org/10.1002/esp.3290130403

Farbrot, H., Isaksen, K., Etzelmüller, B. et Gisnås, K. (2013). Ground thermal regime and permafrost distribution under a changing climate in Northern Norway. *Permafrost and Periglacial Processes*, *24*(1), 20–38. https://doi.org/10.1002/ppp.1763

Fiorio, B., Meyssonnier, J. et Boulon, M. (2002). Experimental study of the friction of ice over concrete under simplified ice-structure interaction conditions. *Canadian Journal of Civil Engineering*, *29*(3), 347–359. https://doi.org/10.1139/l02-012

Fischer, L., Amann, F., Moore, J. R. et Huggel, C. (2010). Assessment of periglacial slope stability for the 1988 Tschierva rock avalanche (Piz Morteratsch, Switzerland). *Engineering Geology*, *116*(1–2), 32–43. https://doi.org/10.1016/j.enggeo.2010.07.005

Fortin, G., Hétu, B., Gauthier, F. et Germain, D. (2015). Extrêmes météorologiques et leurs impacts géomorphologiques : le cas de la Gaspésie. In *XXVIIIe Colloque de l'Association Internationale de Climatologie, Liège* (pp. 469–474).

Fortin, G., Hétu, B. et Germain, D. (2011). Climat hivernal et régimes avalancheux dans les corridors routiers de La Gaspésie septentrionale (Québec, Canada). *Climatologie*, *8*, 9–25. https://doi.org/10.4267/climatologie.202

Gariano, S. L. et Guzzetti, F. (2016). Landslides in a changing climate. *Earth-Science Reviews*, *162*, 227–252. https://doi.org/10.1016/j.earscirev.2016.08.011

Gauthier, F., Allard, M. et Hétu, B. (2015). Ice wall growth and decay: Meteorological analysis and modelling. *Permafrost and Periglacial Processes*, *26*(1), 84–102. https://doi.org/10.1002/ppp.1835

Gauthier, F., Birien, T. et Meloche, F. (2022a). Dynamique des parois de flysch (partie1) : développement des instabilités et modes de rupture. *In* Société canadienne de géotechnique (Ed.), *8e conférence canadienne sur la géotechnique et les risques naturels - Géorisques8* (pp. 373–380). Québec.

Gauthier, F., Germain, D. et Hétu, B. (2017). Logistic models as a forecasting tool for snow

avalanches in a cold maritime climate: northern Gaspésie, Québec, Canada. *Natural Hazards*, *89*(1), 201–232. https://doi.org/10.1007/s11069-017-2959-3

Gauthier, F., Hétu, B. et Allard, M. (2015). Forecasting method of ice blocks fall using logistic model and melting degree–days calculation: a case study in northern Gaspésie, Québec, Canada. *Natural Hazards*, *79*(2), 855–880. https://doi.org/10.1007/s11069-015-1880-x

Gauthier, F., Laliberté, J., Birien, T., Boulet, Y., Meloche, F. et Buffin-Bélanger, T. (2022b). *Influence des variables météorologiques et des changements climatiques sur l'occurrence, la fréquence et la magnitude des mouvements de versant (avalanche de neige, chute de blocs de glace et chute de pierre) affectant certains tronçons des routes 132 et 198 dans le nord de la Gaspésie.* Rapport final. Laboratoire de géomorphologie et de gestion des risques en montagne, Université du Québec à Rimouski. Rapport remis au ministère des Transports du Québec. Rimouski.

Gauthier, F., Montagnat, M., Weiss, J., Allard, M. et Hétu, B. (2013). Ice cascade growth and decay: A thermodynamic approach. *Journal of Glaciology*, *59*(215), 507–523. https://doi.org/10.3189/2013JoG12J206

Gauthier, F., Thériault, N. et Birien, T. (2020). *Influence des variables météorologiques et des changements climatiques sur l'occurrence, la fréquence et la magnitude des mouvements de versant (avalanche de neige, chute de blocs de glace et chute de pierre) affectant certains tronçons des routes 132 et 198 dans le nord de la Gaspésie*. Rapport d'étape 4 : État d'avancement des travaux. Laboratoire de géomorphologie et de gestion des risques en montagne, Université du Québec à Rimouski. Présenté au ministère des Transports du Québec.

Gauthier, F., Truchon, F., Ringuet, E., Birien, T., Boulet, Y. et Meloche, F. (2018). *Influence des variables météorologiques et des changements climatiques sur l'occurrence, la fréquence et la magnitude des mouvements de versant (avalanche de neige, chute de blocs de glace et chute de pierre) affectant certains tronçons des routes 132 et 198 dans le nord de la Gaspésie.* Rapport d'étape 2 : Méthodologie préliminaire. Laboratoire de géomorphologie et de gestion des risques en montagne, Université du Québec à Rimouski. Présenté au ministère des Transports du Québec.

Giani, G. P. (1992). *Rock Slope Stability Analysis*. Boca Raton, FL, USA: CRC Press.

Gischig, V. S., Moore, J. R., Evans, K. F., Amann, F. et Loew, S. (2011a). Thermomechanical forcing of deep rock slope deformation: 1. Conceptual study of a simplified slope. *Journal of Geophysical Research: Earth Surface*, *116*(4), 1–18. https://doi.org/10.1029/2011JF002006

Gischig, V. S., Moore, J. R., Evans, K. F., Amann, F. et Loew, S. (2011b). Thermomechanical forcing of deep rock slope deformation: 2. the Randa rock slope

instability. *Journal of Geophysical Research: Earth Surface*, *116*(4), 1–17. https://doi.org/10.1029/2011JF002007

Gobiet, A., Kotlarski, S., Beniston, M., Heinrich, G., Rajczak, J. et Stoffel, M. (2014). 21st century climate change in the European Alps-A review. *Science of the Total Environment*, *493*, 1138–1151. https://doi.org/10.1016/j.scitotenv.2013.07.050

Gray, J., Davesne, G., Fortier, D. et Godin, E. (2017). The Thermal Regime of Mountain Permafrost at the Summit of Mont Jacques-Cartier in the Gaspé Peninsula, Québec, Canada: A 37 Year Record of Fluctuations showing an Overall Warming Trend. *Permafrost and Periglacial Processes*, *28*(1), 266–274. https://doi.org/10.1002/ppp.1903

Gruber, S. et Haeberli, W. (2007). Permafrost in steep bedrock slopes and its temperatures-related destabilization following climate change. *Journal of Geophysical Research: Earth Surface*, *112*(2). https://doi.org/10.1029/2006JF000547

Gruber, S., Hoelzle, M. et Haeberli, W. (2004a). Permafrost thaw and destabilization of Alpine rock walls in the hot summer of 2003. *Geophysical Research Letters*, *31*(13). https://doi.org/10.1029/2004GL020051

Gruber, S., Hoelzle, M. et Haeberli, W. (2004b). Rock-wall temperatures in the Alps: Modelling their topographic distribution and regional differences. *Permafrost and Periglacial Processes*, *15*(3), 299–307. https://doi.org/10.1002/ppp.501

Gruber, S., Peter, M., Hoelzle, M., Woodhatch, I. et Haeberli, W. (2003). Surface temperatures in steep alpine rock faces - a strategy for regional-scale measurement and modelling. *In* Swets et Zeitlinger Lisse (Ed.), *Proceedings of the 8th International Conference on Permafrost* (Vol. 1, pp. 325–330).

Gruner, U. (2008). Climatic and meteorological influences on rockfall and rockslides ("Bergsturz"). *In* Proceedings 11th Interpraevent Congress (Ed.), *Protection of populated territories from floods, debris flow, mass movements and avalanches* (pp. 147–158).

Guerin, A., Hantz, D., Rossetti, J.-P. et Jaboyedoff, M. (2014). Brief communication "Estimating rockfall frequency in a mountain limestone cliff using terrestrial laser scanner." *Natural Hazards and Earth System Sciences Discussions*, *2*(1), 123–135. https://doi.org/10.5194/nhessd-2-123-2014

Guerin, A., Stock, G. M., Radue, M. J., Jaboyedoff, M., Collins, B. D., Matasci, B., … et Derron, M. H. (2020). Quantifying 40 years of rockfall activity in Yosemite Valley with historical Structure-from-Motion photogrammetry and terrestrial laser scanning. *Geomorphology*, *356*, 107069. https://doi.org/10.1016/j.geomorph.2020.107069

Gunzburger, Y., Merrien-Soukatchoff, V. et Guglielmi, Y. (2005). Influence of daily surface temperature fluctuations on rock slope stability: Case study of the Rochers de Valabres slope (France). *International Journal of Rock Mechanics and Mining Sciences*, *42*(3), 331–349. https://doi.org/10.1016/j.ijrmms.2004.11.003

Hales, T. C. et Roering, J. J. (2007). Climatic controls on frost cracking and implications for the evolution of bedrock landscapes. *Journal of Geophysical Research: Earth Surface*, *112*(2), 1–14. https://doi.org/10.1029/2006JF000616

Hall, K. (1986). Rock moisture content in the field and the laboratory and its relationship to mechanical weathering studies. *Earth Surface Processes and Landforms*, *11*(2), 131–142. https://doi.org/10.1002/esp.3290110204

Hall, K. (1997). Rock temperatures and implications for cold region weathering. I: New data from Viking Valley, Alexander Island, Antarctica. *Permafrost and Periglacial Processes*, *8*(1), 69–90. https://doi.org/10.1002/(SICI)1099-1530(199701)8:1<69::AID-PPP236>3.0.CO;2-Q

Hall, K. (2004). Evidence for freeze-thaw events and their implications for rock weathering in northern Canada. *Earth Surface Processes and Landforms*, *29*(1), 43–57. https://doi.org/10.1002/esp.1012

Hall, K. et André, M. F. (2001). New insights into rock weathering from high-frequency rock temperature data: an Antarctic study of weathering by thermal stress. *Geomorphology*, *41*(1), 23–35. https://doi.org/10.1016/S0169-555X(01)00101-5

Hall, K. et Hall, A. (1996). Weathering by wetting and drying: some experimental results. *Earth Surface Processes and Landforms*, *21*(4), 365–376.

Hall, K., Lindgren, B. S. et Jackson, P. (2005). Rock albedo and monitoring of thermal conditions in respect of weathering: Some expected and some unexpected results. *Earth Surface Processes and Landforms*, *30*(7), 801–811. https://doi.org/10.1002/esp.1189

Hall, K., Thorn, C. E., Matsuoka, N. et Prick, A. (2002). Weathering in cold regions: some thoughts and perspectives. *Progress in Physical Geography*, *26*(4), 577–603. https://doi.org/10.1191/0309133302pp353ra

Hall, K., Thorn, C. et Sumner, P. (2012). On the persistence of "weathering." *Geomorphology*, *149*, 1–10. https://doi.org/10.1016/j.geomorph.2011.12.024

Hallet, B., Walder, J. S. et Stubbs, C. W. (1991). Weathering by segregation ice growth in microcracks at sustained subzero temperatures: Verification from an experimental study using acoustic emissions. *Permafrost and Periglacial Processes*, *2*(4), 283–300. https://doi.org/10.1002/ppp.3430020404

Haque, U., da Silva, P. F., Devoli, G., Pilz, J., Zhao, B., Khaloua, A., … et Glass, G. E. (2019). The human cost of global warming: Deadly landslides and their triggers (1995–2014). *Science of the Total Environment*, *682*, 673–684. https://doi.org/10.1016/j.scitotenv.2019.03.415

Harris, C., Arenson, L. U., Christiansen, H. H., Etzelmüller, B., Frauenfelder, R., Gruber, S., … et Vonder Mühll, D. (2009). Permafrost and climate in Europe: Monitoring and modelling thermal, geomorphological and geotechnical responses. *Earth-Science Reviews*, *92*(3–4), 117–171. https://doi.org/10.1016/j.earscirev.2008.12.002

Hartmann, D. L., Klein Tank, A. M. G., Rusticucci, M., Alexander, L. V., Brönnimann, S., Charabi, Y., … et Zhai P.M. (2013). IPCC Climate Change 2013: The Physical Science Basis. Chapter 2: Observations: Atmosphere and Surface. *In* Climate Change 2013 the Physical Science Basis: Working Group I Contribution to the Fifth Assessment Report of the Intergovernmental Panel on Climate Change (Vol. 9781107057, pp. 159–254).

Hartmeyer, I., Keuschnig, M., Delleske, R., Krautblatter, M., Lang, A., Schrott, L. et Otto, J.-C. (2020). A 6-year lidar survey reveals enhanced rockwall retreat and modified rockfall magnitudes/frequencies in deglaciating cirques. *Earth Surface Dynamics*, *8*, 753–768. https://doi.org/10.5194/esurf-8-753-2020

Hasler, A., Gruber, S., Font, M. et Dubois, A. (2011). Advective heat transport in frozen rock clefts: Conceptual model, laboratory experiments and numerical simulation. *Permafrost and Periglacial Processes*, *22*(4), 378–389. https://doi.org/10.1002/ppp.737

Hasler, A., Gruber, S. et Haeberli, W. (2011). Temperature variability and offset in steep alpine rock and ice faces. *Cryosphere*, *5*(4), 977–988. https://doi.org/10.5194/tc-5-977-2011

Hétu, B. (2007a). Analysis of the weather conditions leading to avalanche activity along transportation roads in Northern Gaspésie , Canada. *Géographie Physique et Quaternaire*, *61*(2–3), 17. https://doi.org/10.7202/038990ar

Hétu, B. (2007b). Les conditions météorologiques propices au déclenchement des avalanches de neige dans les corridors routiers du nord de la Gaspésie, Québec, Canada. *Géographie Physique et Quaternaire*, *61*(2–3), 165. https://doi.org/10.7202/038990ar

Hétu, B. et Gray, J. T. (1985). Le modelé d'érosion glaciaire de la Gaspésie septentrionale. *Geog. Physique et Quaternaire*, *39*(1), 47–66. https://doi.org/10.7202/032584ar

Hétu, B. et Gray, J. T. (2000). Effects of environmental change on scree slope development throughout the postglacial period in the Chic Choc Mountains in northern Gaspé Peninsula , Québec, (April), 335–355. https://doi.org/10.1016/S0169-555X(99)00103-8

Hétu, B. et Vandelac, P. (1989). La dynamique des éboulis schisteux au cours de l'hiver, Gaspésie septentrionale, Québec. *Géographie Physique et Quaternaire*, *43*(3), 389–406. https://doi.org/10.7202/032791ar

Higgins, C. G. et Coates, D. R. (1990). *Groundwater geomorphology: The role of subsurface water in Earth-surface processes and landforms*. (Geological Society of America Special Paper 252, Ed.). Boulder, Colorado. https://doi.org/10.1130/SPE252

Higgins, C. G. et Osterkamp, W. R. (1990). Seepage-induced cliff recession and regional denudation. *In* Geological Society of America (Ed.), *Groundwater Geomorphology: The Role of Subsurface Water in Earth-Surface Processes and Landforms* (pp. 291–318).

Highland, L. et Bobrowsky, P. (2008). The Landslide Handbook — A Guide to Understanding Landslides. *US Geological Survey Circular*, 129. https://doi.org/Circular 1325

Hilker, N., Badoux, A. et Hegg, C. (2009). The Swiss flood and landslide damage database 1972–2007. *Natural Hazards and Earth System Sciences*, *9*(3), 913–925. https://doi.org/10.5194/nhess-9-913-2009

Hinchliffe, S. et Ballantyne, C. K. (1999). Talus accumulation and Rockwall retreat, Trotternish, isle of Skye , Scotland Talus Accumulation and Rockwall Retreat. *Scottish Geographical Journal*, *115*(1), 53–70. https://doi.org/10.1080/00369229918737057

Hoek, E. et Bray, J. (1981). *Rock slope engineering* (3rd ed.). London: The Institution of Mining and Metallurgy.

Höllerman, P. (1983). Blockgletscher als Mesoformen der Per iglazialstufe. *Bonner Geographische Abhandlungen*, *67*.

Huggel, C. (2009). Recent extreme slope failures in glacial environments : effects of thermal perturbation. *Quaternary Science Reviews*, *28*(11–12), 1119–1130. https://doi.org/10.1016/j.quascirev.2008.06.007

Huggel, C., Clague, J. J. et Korup, O. (2012). Is climate change responsible for changing landslide activity in high mountains? *Earth Surface Processes and Landforms*, *37*(1), 77–91. https://doi.org/10.1002/esp.2223

Humlum, O. (2000). The geomorphic significance of rock glaciers: Estimates of rock glacier debris volumes and headwall recession rates in West Greenland. *Geomorphology*, *35*(1–2), 41–67. https://doi.org/10.1016/S0169-555X(00)00022-2

Hungr, O., Evans, S. G. et Hazzard, J. (1999). Magnitude and frequency of rock falls and rock slides along the main transportation corridors of southwestern British Columbia.

Canadian Geotechnical Journal, *36*(2), 224–238. https://doi.org/10.1139/t98-106

Hungr, O., Leroueil, S. et Picarelli, L. (2014). The Varnes classification of landslide types, an update. *Landslides*, *11*(2), 167–194. https://doi.org/10.1007/s10346-013-0436-y

ISRM. (1979). Suggested methods for determining water content, porosity, density absorption and related properties and swelling and slake-durability index properties. *Int J Rock Mech Min Sci Geo Abstr*, *16*, 141–156.

Jarman, D. (2006). Large rock slope failures in the Highlands of Scotland: Characterisation, causes and spatial distribution. *Engineering Geology*, *83*(1–3), 161–182. https://doi.org/10.1016/j.enggeo.2005.06.030

Keefer, D. K. (1984). Landslides caused by earthquakes. *Geological Society of America Bulletin*, *95*(4), 406–421. https://doi.org/10.1130/0016-7606(1984)95<406:LCBE>2.0.CO;2

Keiler, M., Knight, J. et Harrison, S. (2010). Climate change and geomorphological hazards in the eastern European Alps. *Philosophical Transactions of the Royal Society A: Mathematical, Physical and Engineering Sciences*, *368*(1919), 2461–2479. https://doi.org/10.1098/rsta.2010.0047

Korup, O. et Clague, J. J. (2009). Natural hazards , extreme events , and mountain topography. *Quaternary Science Reviews*, *28*(11–12), 977–990. https://doi.org/10.1016/j.quascirev.2009.02.021

Korup, O., Görüm, T. et Hayakawa, Y. (2012). Without power? Landslide inventories in the face of climate change. *Earth Surface Processes and Landforms*, *37*(1), 92–99. https://doi.org/10.1002/esp.2248

Krautblatter, M. et Moser, M. (2009). A nonlinear model coupling rockfall and rainfall intensity based on a four year measurement in a high Alpine rock wall (Reintal, German Alps). *Natural Hazards and Earth System Science*, *9*(4), 1425–1432. https://doi.org/10.5194/nhess-9-1425-2009

Krautblatter, M. et Dikau, R. (2007). Towards a uniform concept for the comparison and extrapolation of rockwall retreat and rockfall supply. *Geografiska Annaler, Series A: Physical Geography*, *89*(1), 21–40. https://doi.org/10.1111/j.1468-0459.2007.00305.x

Krautblatter, M., Funk, D. et Günzel, F. K. (2013). Why permafrost rocks become unstable: A rock-ice-mechanical model in time and space. *Earth Surface Processes and Landforms*, *38*(8), 876–887. https://doi.org/10.1002/esp.3374

Kromer, R. A., Rowe, E., Hutchinson, J., Lato, M. et Abellán, A. (2018). Rockfall risk management using a pre-failure deformation database. *Landslides*, *15*(5), 847–858.

https://doi.org/10.1007/s10346-017-0921-9

Kromer, R., Walton, G., Gray, B., Lato, M. et Group, R. (2019). Development and optimization of an automated fixed-location time lapse photogrammetric rock slope monitoring system. *Remote Sensing*, *11*(16). https://doi.org/10.3390/rs11161890

Lachenbruch, A. H., Cladouhos, T. T. et Saltus, R. W. (1988). Permafrost temperature and the changing climate. *In* Fifth International Conference on Permafrost (Vol. 3, pp. 9–17). Trondhelm, Norway.

Lague, D., Brodu, N. et Leroux, J. (2013). Accurate 3D comparison of complex topography with terrestrial laser scanner: Application to the Rangitikei canyon (N-Z). *ISPRS Journal of Photogrammetry and Remote Sensing*, *82*(February 2013), 10–26. https://doi.org/10.1016/j.isprsjprs.2013.04.009

Laliberté, J., Gauthier, F. et Birien, T. (2022). Dynamique des parois de flysch (partie3) : prévision des chutes de pierres. *In* Société canadienne de géotechnique (Ed.), *8e conférence canadienne sur la géotechnique et les risques naturels - Géorisques 8* (pp. 395–402). Québec.

Lato, M. J., Jean Hutchinson, D., Gauthier, D., Edwards, T. et Ondercin, M. (2015). Comparison of airborne laser scanning, terrestrial laser scanning, and terrestrial photogrammetry for mapping differential slope change in mountainous terrain. *Canadian Geotechnical Journal*, *52*(2), 129–140. https://doi.org/10.1139/cgj-2014-0051

Lim, M., Rosser, N. J., Allison, R. J. et Petley, D. N. (2010). Erosional processes in the hard rock coastal cliffs at Staithes, North Yorkshire. *Geomorphology*, *114*(1–2), 12–21. https://doi.org/10.1016/j.geomorph.2009.02.011

Lippmann and Rauen GbR. (2022). Thermal Conductivity Scanning. Retrieved from http://www.geophysik-dr-rauen.de/tcscan/index.html

Macciotta, R., Cruden, D. M., Martin, C. D., Morgenstern, N. R. et Petrov, M. (2013). Spatial and temporal aspects of slope hazards along a railroad corridor in the Canadian Cordillera. *In* Slope Stability 2013: Proceedings of the 2013 International Symposium on Slope Stability in Open Pit Mining and Civil Engineering, Austria (pp. 1171–1185). https://doi.org/10.36487/ACG_rep/1308_83_Macciotta

Macciotta, Renato, Hendry, M., Cruden, D. M., Blais-Stevens, A. et Edwards, T. (2017). Quantifying rock fall probabilities and their temporal distribution associated with weather seasonality. *Landslides*, *14*(6), 2025–2039. https://doi.org/10.1007/s10346-017-0834-7

Macciotta, Renato, Martin, C. D., Edwards, T., Cruden, D. M. et Keegan, T. (2015).

Quantifying weather conditions for rock fall hazard management. *Georisk*, *9*(3), 171–186. https://doi.org/10.1080/17499518.2015.1061673

Magnin, F., Josnin, J., Legay, A., Ravanel, L., Deline, P. et Duvillard, P. A. (2021). Recent advances in Rock wall Permafrost Modelling to Understand Bedrock Failures Periglacial rock slope failures are increasing and impact Alpine and Arctic communities. International Association of Geomorphologists Webminar.

Malamud, B. D., Turcotte, D. L., Guzzetti, F. et Reichenbach, P. (2004). Landslides, earthquakes, and erosion. *Earth and Planetary Science Letters*, *229*(1–2), 45–59. https://doi.org/10.1016/j.epsl.2004.10.018

Marinos, P. et Hoek, E. (2001). Estimating the geotechnical properties of heterogeneous rock masses such as flysch. *Bulletin of Engineering Geology and the Environment*, *60*(2), 85–92. https://doi.org/10.1007/s100640000090

Martynov, A., Laprise, R., Sushama, L., Winger, K., Šeparović, L. et Dugas, B. (2013). Reanalysis-driven climate simulation over CORDEX North America domain using the Canadian Regional Climate Model, version 5: Model performance evaluation. *Climate Dynamics*, *41*(11–12), 2973–3005. https://doi.org/10.1007/s00382-013-1778-9

Marzorati, S., Luzi, L. et De Amicis, M. (2002). Rock falls induced by earthquakes: A statistical approach. *Soil Dynamics and Earthquake Engineering*, *22*(7), 565–577. https://doi.org/10.1016/S0267-7261(02)00036-2

Matsuoka, N. (1990). The rate of bedrock weathering by frost action: Field measurements and a predictive model. *Earth Surface Processes and Landforms*, *15*(1), 73–90. https://doi.org/10.1002/esp.3290150108

Matsuoka, N. (1991). A model of the rate of frost shattering: Application to field data from Japan, Svalbard and Antarctica. *Permafrost and Periglacial Processes*, *2*(4), 271–281. https://doi.org/10.1002/ppp.3430020403

Matsuoka, N. (2001). Direct observation of frost wedging in alpine bedrock. *Earth Surface Processes and Landforms*, *26*(6), 601–614. https://doi.org/10.1002/esp.208

Matsuoka, N. (2008). Frost weathering and rockwall erosion in the southeastern Swiss Alps: Long-term (1994-2006) observations. *Geomorphology*, *99*(1–4), 353–368. https://doi.org/10.1016/j.geomorph.2007.11.013

Matsuoka, N. (2019). A multi-method monitoring of timing, magnitude and origin of rockfall activity in the Japanese Alps. *Geomorphology*, *336*, 65–76. https://doi.org/10.1016/j.geomorph.2019.03.023

Matsuoka, N., Hirakawa, K., Watanabe, T. et Moriwaki, K. (1997). Monitoring of periglacial

slope processes in the Swiss Alps : the first two years of frost shattering , heave and creep. *Permafrost and Periglacial Processes*, *8*(2), 155–177. https://doi.org/10.1002/(SICI)1099-1530(199732)8:2%3C155::AID-PPP248%3E3.0.CO;2-N

Matsuoka, N. et Murton, J. (2008). Frost Weathering: Recent Advances and Future Directions. *Permafrost and Periglacial Processes*, *19*(2), 195–210. https://doi.org/10.1002/ppp.620

Matsuoka, N. et Sakai, H. (1999). Rockfall activity from an alpine cliff during thawing periods. *Geomorphology*, *28*(3–4), 309–328. https://doi.org/10.1016/S0169-555X(98)00116-0

McGreevy, J. P. et Whalley, W. B. (1985). Rock moisture content and frost weathering under natural and experimental conditions: a comparative discussion. *Arctic & Alpine Research*, *17*(3), 337–346. https://doi.org/10.2307/1551022

Mearns, L., McGinnis, S., Korytina, D., Arritt, R., Biner, S. et Bukovsky, M. (2017). The NA-Cordex dataset, version 1.0. NCAR Climate Data Gateway, Boulder CO. https://doi.org/10.5065/D6SJ1JCH

Michoud, C., Derron, M., Horton, P., Jaboyedoff, M., Baillifard, F., Loye, A., … et Pedrazzini, A. (2012). Rockfall hazard and risk assessments along roads at a regional scale : example in Swiss Alps. *Natural Hazards and Earth System Sciences*, *12*(3), 615–629. https://doi.org/10.5194/nhess-12-615-2012

Ministère du Transport du Québec. (2021). *Base de données événementielle des chutes de pierres entre 1987 et 2021*.

Miščević, P. et Vlastelica, G. (2014). Impact of weathering on slope stability in soft rock mass. *Journal of Rock Mechanics and Geotechnical Engineering*, *6*(3), 240–250. https://doi.org/10.1016/j.jrmge.2014.03.006

Mourey, J., Lacroix, P., Duvillard, P. A., Marsy, G., Marcer, M., Malet, E. et Ravanel, L. (2022). Multi-method monitoring of rockfall activity along the classic route up Mont Blanc (4809 m a.s.l.) to encourage adaptation by mountaineers. *Natural Hazards and Earth System Sciences*, *22*(2), 445–460. https://doi.org/10.5194/nhess-22-445-2022

Mourey, J., Perrin-Malterre, C. et Ravanel, L. (2020). Strategies used by French Alpine guides to adapt to the effects of climate change. *Journal of Outdoor Recreation and Tourism*, *29*(December 2019). https://doi.org/10.1016/j.jort.2020.100278

Noetzli, J., Gruber, S., Kohl, T., Salzmann, N. et Haeberli, W. (2007). Three-dimensional distribution and evolution of permafrost temperatures in idealized high-mountain topography. *Journal of Geophysical Research: Earth Surface*, *112*(2), 1–14.

https://doi.org/10.1029/2006JF000545

Ollier, C. (1984). *Weathering*. (Longman Group, Ed.) (2nd ed.).

Olyphant, G. A. (1983). Analysis of the factors controlling cliff burial by talus within Blanca Massif, southern Colorado, USA. *Arctic & Alpine Research*, *15*(1), 65–75. https://doi.org/10.2307/1550982

Oppikofer, T, Jaboyedoff, M., Blikra, L., Derron, M. et Metzger, R. (2009a). Characterization and monitoring of the Åknes rockslide using terrestrial laser scanning. *Natural Hazards and Earth System Science*, *9*, 1003–1019. https://doi.org/10.5194/nhess-9-1003-2009

Oppikofer, T, Jaboyedoff, M., Blikra, L., Derron, M. et Metzger, R. (2009b). Lebensphasenspezifische Gesundheit von Kindern und Jugendlichen in Deutschland. Ergebnisse des Nationalen Kinder- und Jugendgesundheitssurveys. *Bundesgesundheitsblatt, Gesundheitsforschung, Gesundheitsschutz*, *52*(2), 238. https://doi.org/10.1007/s00103-009-0785-9

Oppikofer, Thierry, Jaboyedoff, M. et Keusen, H. R. (2008). Collapse at the eastern Eiger flank in the Swiss Alps. *Nature Geoscience*, *1*(8), 531–535. https://doi.org/10.1038/ngeo258

Paranunzio, R., Laio, F., Chiarle, M., Nigrelli, G. et Guzzetti, F. (2016). Climate anomalies associated with the occurrence of rockfalls at high-elevation in the Italian Alps. *Natural Hazards and Earth System Sciences*, *16*(9), 2085–2106. https://doi.org/10.5194/nhess-16-2085-2016

Peckover, F. L. (1975). *Treatment of rock falls on railway lines. American Railway Engineering Association* (Vol. Bulletin 6). Chicago, IL.

Peckover, F. L. et Kerr, J. W. G. (1977). Treatment and maintenance of rock slopes on transportation routes. *Can*, *14*, 487.

Piteau, D. R. et Peckover, F. L. (1978). Engineering of Rock Slopes. *In* Landslides, Analysis and Control, Transportation Research Board, in: Special Report 176, edited by: Schuster, R. L. and Krizek, R. J., Washington, DC (pp. 192–228). National Academy of Sciences, Washington DC.

Porter, S. C. et Orombelli, G. (1980). Catastrophic rockfall of September 12, 1717 on the Italian flank of the Mont Blanc massif. *Zeitschrift Für Geomorphologie Stuttgart*, *24*(2), 200–218. https://doi.org/10.1127/zfg/24/1984/200

Pratt, C., Macciotta, R. et Hendry, M. (2019). Quantitative relationship between weather seasonality and rock fall occurrences north of Hope, BC, Canada. *Bulletin of*

Engineering Geology and the Environment, *78*(5), 3239–3251. https://doi.org/10.1007/s10064-018-1358-7

Pröbstl-Haider, U., Hödl, C., Ginner, K. et Borgwardt, F. (2021). Climate change: Impacts on outdoor activities in the summer and shoulder seasons. *Journal of Outdoor Recreation and Tourism*, *34*(October 2020). https://doi.org/10.1016/j.jort.2020.100344

Rabatel, A., Deline, P., Jaillet, S. et Ravanel, L. (2008). Rock falls in high-alpine rock walls quantified by terrestrial lidar measurements: A case study in the Mont Blanc area. *Geophysical Research Letters*, *35*(10), 1–5. https://doi.org/10.1029/2008GL033424

Rapp, A. (1960). Recent Development of Mountain Slopes in Kärkevagge and Surroundings, Northern Scandinavia. *Geografiska Annaler*, *42*(2–3), 65–200. https://doi.org/10.1080/20014422.1960.11880942

Ravanel, L. et Deline, P. (2011). Climate influence on rockfalls in high-alpine steep rockwalls: The north side of the aiguilles de chamonix (mont blanc massif) since the end of the "Little Ice Age." *Holocene*, *21*(2), 357–365. https://doi.org/10.1177/0959683610374887

Rempel, A. W., Marshall, J. A. et Roering, J. J. (2016). Modeling relative frost weathering rates at geomorphic scales. *Earth and Planetary Science Letters*, *453*, 87–95. https://doi.org/10.1016/j.epsl.2016.08.019

Rode, M., Schnepfleitner, H. et Sass, O. (2016). Simulation of moisture content in alpine rockwalls during freeze–thaw events. *Earth Surface Processes and Landforms*, *41*(13), 1937–1950. https://doi.org/10.1002/esp.3961

Rosser, N. J., Petley, D. N., Lim, M., Dunning, S. A. et Allison, R. J. (2005). Terrestrial laser scanning for monitoring the process of hard rock coastal cliff erosion. *Quarterly Journal of Engineering Geology and Hydrogeology*, *38*(4), 363–375. https://doi.org/10.1144/1470-9236/05-008

Royán, M. J., Abellán, A., Jaboyedoff, M., Vilaplana, J. M. et Calvet, J. (2014). Spatio-temporal analysis of rockfall pre-failure deformation using Terrestrial LiDAR. *Landslides*, *11*(4), 697–709. https://doi.org/10.1007/s10346-013-0442-0

Samuelsson, P., Jones, C. G., Willén, U., Ullerstig, A., Gollvik, S., Hansson, U., … et Wyser, K. (2011). The Rossby Centre Regional Climate model RCA3: Model description and performance. *Tellus, Series A: Dynamic Meteorology and Oceanography*, *63*(1), 4–23. https://doi.org/10.1111/j.1600-0870.2010.00478.x

Santana, D., Corominas, J., Mavrouli, O. et Garcia-Sellés, D. (2012). Magnitude-frequency relation for rockfall scars using a Terrestrial Laser Scanner. *Engineering Geology*, *144–145*, 50–64. https://doi.org/10.1016/j.enggeo.2012.07.001

Sass, O. (1998). Die Steuerung von Steinschlagmenge durch Mikroklima, Gesteinsfeuchte und Gesteinseigenschaften im westlichen Karwendelgebirge. *Münchner Geographische Abhandlungen Reihe B, 29*, 347–359.

Sass, O. (2005a). Rock moisture measurements: Techniques, results, and implications for weathering. *Earth Surface Processes and Landforms*, *30*(3), 359–374. https://doi.org/10.1002/esp.1214

Sass, O. (2005b). Temporal Variability of Rockfall in the Bavarian Alps, Germany. *Arctic, Antarctic, and Alpine Research*, *37*(4), 564–573. https://doi.org/10.1657/1523-0430(2005)037[0564:TVORIT]2.0.CO;2

Scavia, C., Barbero, M., Castelli, M., Marchelli, M., Peila, D., Torsello, G. et Vallero, G. (2020). Evaluating rockfall risk: Some critical aspects. *Geosciences*, *10*(3), 1–29. https://doi.org/10.3390/geosciences10030098

Schnepfleitner, H., Rode, M. et Sass, O. (2018). Validation of simulated temperature profiles at rock walls in the eastern alps (Dachstein). *Permafrost and Periglacial Processes*, *29*(1), 34–48. https://doi.org/10.1002/ppp.1962

Schovanec, H. E. (2020). *Development of semi-automated lidar processing algorithms to correlate climate variables to rockfall patterns for a slope near Glendwood Springs, Colorado*. Colorado School of Mines: Golden, CO, USA.

Selby, M. (1982). *Hillslope materials and processes*. *New York: Oxford University Press* (1st ed.).

Selby, M. (1993). *Hillslope materials and processes*. *Oxford University Press.* (2nd ed.). Oxford.

Šeparović, L., Alexandru, A., Laprise, R., Martynov, A., Sushama, L., Winger, K., … et Valin, M. (2013). Present climate and climate change over North America as simulated by the fifth-generation Canadian regional climate model. *Climate Dynamics*, *41*, 3167–3201. https://doi.org/10.1007/s00382-013-1737-5

Sidle, R. et Ochiai, H. (2006). *Landslides : processes, prediction, and land use, Water Res Monograph* (Vol. 18). Washington: American Geophysical Union.

Singhal, B. B. S. et Gupta, R. P. (2010). *Applied hydrogeology of fractured rocks*. (Springer Science & business Media, Ed.) (Second Edi). Springer Netherlands. https://doi.org/10.1007/978-90-481-8799-7

Slivitzky, A., St-Julien, P. et Lachambre, G. (1991). *Synthèse géologique du Cambro-Ordovicien du nord de la Gaspésie*.

Stoll, V., Scandroglio, R. et Krautblatter, M. (2020). Modelling rock walls destabilization caused by hydrostatic pressure in frozen/unfrozen bedrock (Hochvogel & Zugspitze, Germany). Vienna, Austria: Presented at the EGU General Assembly. https://doi.org/10.5194/egusphere-egu2020-14338

Štroner, M., Křemen, T., Braun, J., Urban, R., Blistan, P. et Kovanič, L. (2019). Comparison of 2.5d volume calculation methods and software solutions using point clouds scanned before and after mining. *Acta Montanistica Slovaca*, *24*(4), 296–306.

Terzaghi, K. (1962). Stability of steep slopes on hard unweathered rock. *Géotechnique*, *12*(4), 251–270. https://doi.org/10.1680/geot.1962.12.4.251

Trenhaile, A. (2006). Tidal wetting and drying on shore platforms: An experimental study of surface expansion and contraction. *Geomorphology*, *76*(3–4), 316–331. https://doi.org/10.1016/j.geomorph.2005.11.006

Trenhaile, A. S. et Rudakas, P. A. (1981). Freeze-thaw and shore platform development in Gaspe, Quebec. *Geographie Physique et Quaternaire*, *35*(2), 171–181. https://doi.org/10.7202/1000435ar

Turner, A. K. et Schustler, R. L. (1996). *Landslides: investigation and mitigation* (Special re).

UNDRR. (2022). Terminology. Retrieved July 18, 2022, from https://www.undrr.org/terminology

van Veen, M., Hutchinson, D. J., Kromer, R., Lato, M. et Edwards, T. (2017). Effects of sampling interval on the frequency - magnitude relationship of rockfalls detected from terrestrial laser scanning using semi-automated methods. *Landslides*, *14*(5), 1579–1592. https://doi.org/10.1007/s10346-017-0801-3

van Vuuren, D. P., Edmonds, J., Kainuma, M., Riahi, K., Thomson, A., Hibbard, K., … et Rose, S. K. (2011). The representative concentration pathways: An overview. *Climatic Change*, *109*(1), 5–31. https://doi.org/10.1007/s10584-011-0148-z

Varnes, D. . (1978). Slope movement types and processes. *In* Special Report 176: Landslides: Analysis and Control; Schuster, R.L., Krizek, R.J., Eds.; TRB, National Research Council: Washington, DC, USA, 11–33.

Vergara, M. R. et Triantafyllidis, T. (2016). Influence of Water Content on the Mechanical Properties of an Argillaceous Swelling Rock. *Rock Mechanics and Rock Engineering*, *49*(7), 2555–2568. https://doi.org/10.1007/s00603-016-0938-8

Viles, H. A. (2013). Linking weathering and rock slope instability: Non-linear perspectives. *Earth Surface Processes and Landforms*, *38*(1), 62–70.

https://doi.org/10.1002/esp.3294

Volkwein, A., Schellenberg, K., Labiouse, V., Agliardi, F., Berger, F., Bourrier, F., … et Jaboyedoff, M. (2011). Rockfall characterisation and structural protection – a review. *Natural Hazards and Earth System Sciences*, *11*(9), 2617–2651. https://doi.org/10.5194/nhess-11-2617-2011

Walder, J. S. et Hallet, B. (1985). Theoretical Model of the Fracture of Rock During Freezing. *Bulletin of the Geological Society of America*, *96*(3), 336–346. https://doi.org/10.1130/0016-7606(1985)96<336:atmotf>2.0.co;2

Walder, J. S. et Hallet, B. (1986). The physical basis of frost weathering: toward a more fundamental and unified perspective. *Arctic & Alpine Research*, *18*(1), 27–32. https://doi.org/10.2307/1551211

Weber, S., Beutel, J., Faillettaz, J., Hasler, A., Krautblatter, M. et Vieli, A. (2016). Quantifying irreversible movement in steep fractured bedrock permafrost at Matterhorn (CH). *The Cryosphere Discussions*, (June), 1–23. https://doi.org/10.5194/tc-2016-136

Weber, S., Beutel, J., Faillettaz, J., Hasler, A., Krautblatter, M. et Vieli, A. (2017). Quantifying irreversible movement in steep fractured bedrock permafrost on Matterhorn (CH). *Cryosphere*, *11*(1), 567–583. https://doi.org/10.5194/tc-11-567-2017

Weidner, L. et Walton, G. (2021). Monitoring the effects of slope hazard mitigation and weather on rockfall along a colorado highway using terrestrial laser scanning. *Remote Sensing*, *13*(22). https://doi.org/10.3390/rs13224584

White, S. E. (1976). Is Frost Action Really Only Hydration Shattering? A Review. *Arctic and Alpine Research*, *8*(1), 1. https://doi.org/10.2307/1550606

Wieczorek, G. F. (1996). Landslide triggering mechanisms. In: Turner AK, Schuster RL (eds) Landslides investigation and mitigation, special report. *Transportation Research Board Special Report*, *247*(4), 76–89.

Wieczorek, G. F. et Jäger, S. (1996). Triggering mechanisms and depositional rates of postglacial slope-movement processes in the Yosemite Valley, California. *Geomorphology*, *15*(1), 17–31. https://doi.org/10.1016/0169-555X(95)00112-I

Williams, J. G., Rosser, N. J., Hardy, R. J., Brain, M. J. et Afana, A. A. (2018). Optimising 4-D surface change detection: An approach for capturing rockfall magnitude-frequency. *Earth Surface Dynamics*, *6*(1), 101–119. https://doi.org/10.5194/esurf-6-101-2018

Wyllie, D. C. et Mah, C. (2004). *Rock Slope Engineering* (4th ed.). Boca Raton, FL, USA: CRC Press.

Zadra, A., Caya, D., Côté, J., Dugas, B., Jones, C., Laprise, R., … et Caron, L. P. (2008). The next Canadian regional climate model. *Phys Can*, *64*, 74–83.